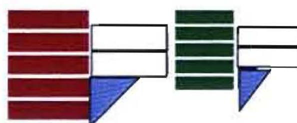

A Dissertation
in

Scanning Probe Microscopy studies and dynamic behaviour of ferroelectric domains in Pb $Zr_{0.53}Ti_{0.47}O_3$ thin films

Science and technologies of Mesophases
& Molecular Materials (STM^3)
XXII Cycle
FIS/07 FIS/01

Presented to the Faculties S.M.F.N. of the University of Calabria
2008/2009

Supervisor
Prof. Nicola Scaramuzza

Ph.D. student
Dott.ssa Emanuela Bruno

Coordinator
Prof. Carlo Versace

Prof. Anca Luiza Alexe Ionescu

Prof. Giovanni Barbero

Prof. Marcello Celasco

Prof. Antonio Sasso

ACKNOWLEDGEMENTS

First and foremost, I would like to thank Prof. Nicola Scaramuzza for being an outstanding supervisor. He introduced me to the field of Liquid Crystal and has guided my research from the first day at the AFM controls to the finer points of science. Many parts of this dissertation would be impossible if it were not for the collaboration with many people. I am deeply grateful to Dr.ssa Maria Penelope De Santo, Dr.ssa Federica Ciuchi and Dr. Marco Castriota for enlightening discussions. Collaborations with they have allowed me to satisfy my curiosity. The discussions with Dr.ssa De Santo were most useful to understand what's going on under the AFM tip. During my time at Lycril, I constantly felt the support and encouragement from the members of group. There are several people in Licryl whom I want to thank in particular. Dr. Salvatore Marino, Dr. Gaetano Nicastro and Dr. Mario Ariosto Matranga.
I would like to thank all members of the Licryl group for their collaborative spirit and for the friendly atmosphere which has always gone beyond the scope of professional relationships.
The research at Licryl would be impossible without the assistance from the staff members. I am especially grateful to Dr. Giovanni Desiderio, Dr. Alfredo Pane, Dr. Giuseppe De Santo and Dr.ssa Tiziana Barone.
Un grande ringraziamento a mio marito Raffaele per il suo amore, il sostegno e la pazienza con cui ha seguito la scrittura di questa tesi. In fine vorrei ringraziare tutta la mia famiglia e i miei amici per il continuo supporto affettivo che mi hanno dato in tutti questi anni e senza la quale oggi non sarei la persona che sono.

Grazie a tutti

Contents

Acknowledgements………………………………………………………....i

Abstract…………………………………………………………………...5

Introduction………………………………………………………………7

Chapter1: Start of the Art……………………………………………...9

1.1 Origins of SPM…………………………………………………9

1.1.2 Working principle of AFM…………..............................11

1.1.3 Forces in AFM………………………………….................14

1.1.4 Piezoresponse Force Microscope..17

1.1.5 Domain Writing……………………………………….....20

1.1.6 SNOM Instrument………………………………………21

1.1.7 NSOM measurement...……………………………………..24

1.1.8 STM..…………………………………………………………26

References...28

Chapter 2: Pyroelectric, Piezoelectric and Ferroelectric materials…29

2.1.1 Pyroelectricity……………………………………………...29

2.1.2 Piezoelectric Materials……………………………………..29

2.1.3 Ferroelectricity……………………………………………..33

2.1.4 Ferroelectric Materials……………………………………..35

2.1.5 Thin Films…………………………………………………36

2.1.6 Memory Applications of Ferroelectric Materials…………..37

2.1.7 (Lead Zircanate Titanate) PZT……………………………..37

2.1.8 Sol-gel preparation…………………………………………38

References...42

Chapter 3: Experimental Techniques……………………………45
3.1.1 AFM technique……………………………………………45
3.1.2 Electronics……………………………………………………52
3.1.3 Control Software…………………………………………...53
3.1.4 AFM and SEM Techniques……………………………...53
3.1.5 SEM image formation……………………………………...55
3.1.6 Electrostatic Force Microscopy (EFM)……………………59
3.1.7 NC EFM………………………………………………………61
3.1.8 DC EFM………………………………………………………65
3.1.9 X- Ray Technique…………………………………………65
References...67

Chapter 4: Qualitative analysis of the tip-sample interaction in AFM Probe Microscopy……………………………………………………69
4.1.1 Cantilever oscillations……………………………………...69
4.1.2 Cantilever oscillation in the no-contact mode……………...73
4.1.3 AFM Topography…………………………………………77
4.1.4 EFM images………………………………………………..78
References...85

Chapter 5: Experimental results……………………………………87
5.1.1 Instruments…………………………………………………88
5.1.2 Presentation of experimental dates for the samples annealed at 1 hour……………………………………………………89
5.1.3 DC-EFM and NC-EFM images on the sample annealed at 800°C…………………………………………………...116
5.1.4 Macroscopic hysteresis cycles…………………………119
5.1.6 Presentation of experimental dates for the samples annealed at 10 hours…………………………………………………123

5.1.6 Morphological evolutions……………………………...127
5.1.7 Electrical response studies……………………………..130
5.1.8 Conclusion………………………………………………..137
References..141

Chapter 6: Direct Measurement Surface Induced Orientational Order Parameter Profile above the Nematic Isotropic Phase Transition Temperature……………………………………………..................143
6.1.1 Introduction……………………………………………143
6.1.2 Results and discussion…………………………………143
References..155
List of the publications………………………………………………..158

Abstract

Scanning Probe Microscopy studies and dynamic behaviour of ferroelectric domains in $PbZr_{0.53}Ti_{0.47}O_3$ thin films

Emanuela Bruno

Dissertation Supervisor: Prof. Nicola Scaramuzza

Ferroelectric domains play an essential role in all ferroelectric materials applications, for example, microelectromechanical sensors systems (MEMS) and integrated optical systems. The prime interest in recent years is, however, in non-volatile random accesses memories (FRAM) based on ferroelectric thin film. This requires substantial improvement in the understanding of the basic proprieties at the nanometer length scale. Especially the domain nucleation and growth processes in ferroelectric is of key importance. As the optical methods are limited by diffraction, novel high resolution techniques are required. The scanning force methods introduced during this thesis offer the required high resolution together with high sensitivity.

In this thesis experimental and theoretical evidence for the origin of the force acting on the tip, the cantilever deflection and the image contrast mechanisms is given for various SFM (Scanning Force Microscopy) operation modes. For imaging ferroelectric domains the best suited SPM technique is the piezoresponse SFM that is performed with the tip in contact with the sample. The spontaneous growth of the domains

nucleating in lead zirconate titanate sample is investigated in detail using the EFM (Electrostatic Force Microscopy) technique. Even more interesting is the case where the domains are intentionally created switching the spontaneous polarization by means of an electric field between the EFM tip and an electrode below the sample. This allows to create any desired pattern of domains. The ability to use the same tip for domain switching and imaging is another advantage of the EFM. The domain formed in this way varies in size from few nanometers to few micrometers. Using EFM technique we demonstrate ferroelectrostatic switching in Lead Zircanate Titanate (PZT) thin film. This has important technological implication because the ferroelectric switching must be used in ferroelectric devices.

Introduction

The study of surfaces has held great importance in terms of technological applications for a long time. Many of the important properties of materials depend critically on the structure of their surfaces and how these surfaces interact with their environment. To really understand processes at surfaces, it is necessary to have information on the local atomic scale.

The development of Scanning Probe Microscopy (SPM) finally offers the surface scientist the possibility to see surfaces on the atomic scale. SPM techniques measure the interaction between a probing tip and the surface on the atomic scale, so that, in principle, individual atoms on the surface can be imaged with an unprecedented ability. Combined with the power of recent theoretical treatments of surfaces, SPM techniques offer a possible solution to a great many of the questions which limit the development of surface applications. In this thesis, I have summarized the results of SPM studies of the local electric properties of oxide materials, in particular ferroelectric oxide thin film such as Lead Zirconate Titanate Pb (Zi Ti)O_3 (PZT).

One of the most fascinating aspects of chemistry and physics of oxide materials is a wide variety of the properties they exhibit. While traditional semiconductor materials typically exhibit a single functionality and the coupling between mechanical, electrical and magnetic properties is relatively weak, this is not the case for the oxide materials.

Ferroelectric materials possess a spontaneous polarization which can be oriented by an external electric field greater than its coercive field. The direction of the spontaneous polarization can be used to stone information.

Once this electric field is turned off the last ”written” polarisation remains as a stable state. In the simplified case the spontaneous polarisation can be considered either positive or negative. This bistable state has been thought of as an obvious way to represent the Boolean Algebra ”1” and ”0”.

Thin films as lead zirconium titanate (PZT) are attracting a growing interest because of their applications in nonvolatile memories and piezoelectric transducers.[1,2] The properties of such ferroelectric materials have been investigated in the past ten years, focusing on problems such as elastic and dielectric properties, polarization fatigue, aging field and frequency dependence of the piezoelectricity.[3,4]

A particularly interesting application is the use of such films as rectifying layers in asymmetric nematic liquid crystal cells (ANLCC). In such cells, the electro-optical response depends on the polarity of the external electric field, so that it is defined as “rectified electro-optical response,” while in the usual cell it is polarity-independent. In fact, metal oxides with mixed ionic and electronic conduction properties have been tested in recent years as rectifying layers in ANLCC and their rectifying effect has been explained by the formation of double charged layers at the interfaces.[5–9]

In contrast, polarity-dependent responses already observed in ANLCC with an inserted PZT layer have been ascribed to a different mechanism: the polar orientation of the ferroelectric film could generate a permanent internal field opposite in polarity to the applied external field.[10] To optimize this particular application of ferroelectric films, specific information must be gathered on the influence of the production methods, the role of the substrate, and the effect of the thermal treatments on the electric and morphological properties of such a layer.

Platinum is the most used substrate for ferroelectric devices because of its good resistance to oxidation. Conducting oxides such as RuO2, [11] IrO2, [12] or SrRuO3. [13] are also used as electrodes to compensate the oxygen vacancies and to eliminate the polarization fatigue of ferroelectric capacitors.[14] In this case, to preserve the transparency required by the specific application, the evolution of the deposited PZT films has been investigated on indium-doped tin oxide ITO substrate. The final samples can be schematized as: glass/ITO/PZT, where the ITO layer is the electronic conductor.

An extensive investigation is carried out on the effects of different annealing temperatures, with regard to the film texture and to the electric polarization properties, by using low vacuum scanning electron microscopy (SEM), atomic force microscopy (AFM) and electrostatic force microscopy (EFM).

The general concept of SPM applied to electric and ferroelectric phenomena is considered in Chapter1 that summarizes current electrostatic SPM techniques.

In chapter 2 we review the basic concepts of ferroelectricity and piezoelectricity.

Chapter 3 presents our experimental techniques including AFM(Atomic Force Microscopy), EFM (Electrostatic Force Microscopy), SEM (Scanning Force Microscopy) techniques and X-Ray measurements.

A detailed analysis of tip-surface interactions in PFM is presented in Chapter 4 where the guidelines for quantitative imaging are developed too.

Properties of ferroelectric surfaces are considered in Chapter 5. Here the domain structure reconstruction from the combined topographic and electric measurements is presented. Origins of the electrostatic domain contrast are analyzed and it is shown that the polarization charge is almost

completely screened. Different temperatures of the preparation of the sample and different exposure at the annealed coating are shown. EFM images, X-Ray patterns are studied.

References

[1] C. T. Lin, B. W. Scanlan, J. D. Mcneill, J. S. Webb, and L. Li, J. Mater.Res. **7**, 2546 -1992.

[2] S. S. Dana, K. F. Etzold, and S. Clabes, J. Appl. Phys. **69**, 4398 1991.

[3] Science and Technology of Electroceramic Thin Films (NATO/ARW Series E), edited by O. Auciello and R. Waser _Kluwer, Deventer, 1994, Vol. 284.

[4] D. Damjanovic, "Ferroelectric, dielectric and piezoelectric properties of ferroelectric thin films and ceramics," Ph.D. thesis, Swiss Federal Institute of Technology-EPFL, Lausanne, Switzerland 1998.

[5] S. Marino, M. Castriota, V. Bruno, E. Cazzanelli, G. Strangi, C. Versace, and N. Scaramuzza, J. Appl. Phys. 97, 013523 2005.

[6] M. Castriota, S. Marino, C. Versace, G. Strangi, N. Scaramuzza, and E. Cazzanelli, Mol. Cryst. Liq. Cryst. 429, 237 2005.

[7] G. Strangi, E. Cazzanelli, N. Scaramuzza, C. Versace, and R. Bartolino, Phys. Rev. E **62**, 2263 2000.

[8] E. Cazzanelli, S. Marino, V. Bruno, M. Castriota, N. Scaramuzza, G. Strangi, C. Versace, R. Ceccato, and G. Carturan, Solid State Ionics 165, 201 2003.

[9] V. Bruno, M. Castriota, S. Marino, C. Versace, G. Strangi, E. Cazzanelli, and N. Scaramuzza, Mol. Cryst. Liq. Cryst. 441, 27 2005.

[10] S. Marino, M. Castriota, G. Strangi, E. Cazzanelli, and N. Scaramuzza, J.Appl. Phys. 102, 013112 2007.

[11] G. Asano, H. Morioka, and H. Funakubo, Appl. Phys. Lett. 83, 5506 2003.

[12] B. S. Kang, D. S. Kim, J. Y. Jo, T. W. Noh, J. G. Yoon, T. K. Song, Y. K. Lee, J. K. Lee, S. Shin, and Y. S. Park, Appl. Phys. Lett. 84, 3127 2004.

[13] S. Aggarwal, I. G. Jenkins, B. Nagarag, C. J. Kerr, C. Canedy, R. Ramesh,G. Velasquez, L. Boyer, and J. T. Evans, Jr., Appl. Phys. Lett. **75**, 1787, 1999.

[14] Z. Jia, T. L. Ren, T. Z. Liu, H. Hu, Z. G. Zhang, D. Xie, and L. T. Liu, Chin. Phys. Lett. 23, 1042 2006.

Chapter 1

State of the Art

The scope of this thesis is to get a better understanding of the mechanisms of polarization reversal in model systems of ferroelectrics in the form of thin films. The transfer of the fundamental findings should help to improve memory applications. Finally, the experimental character of this thesis is underlined by the development of novel characterization tools and methods.

1.1 Origins of SPM

You can not say with certainty who invented the first microscope. One of the first instruments for microscopic investigation is due to Dutch Anton von Leeuwenhoek (1632-1723).

With this instrument that, however, maximized up to 400x, its inventor was able to discover the bacteria, sperm and classify cells according to their shape.

Only many years later the microscopy techniques and of the relative instruments could be classified into three categories: optical microscopy, electron microscopy and other microscopy techniques. The scanning probe microscopy (SPM) is more recent.

The first scanning instrument was the SEM (Scanning Electron Microscope). This instrument uses the electrons, scattered by sample from a focused beam, for the visualization.

The idea of the scan, originally, came to try to improve the resolution that was very limited in the classic optical microscopic instruments.

The first scan instruments, except for the SEM, were still optical, but the fundamental step was the creation of a category of scanning microscopes named near field. The characteristic of these microscopes is the physical interaction, of various kinds, of the sample with a probe that operates precisely in "extreme proximity of the sample. This distance

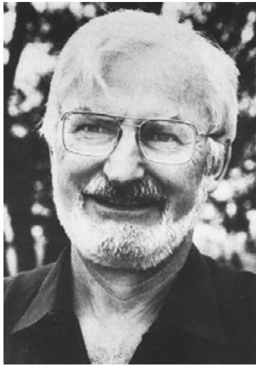

allows, with various mechanisms, to achieve a very high resolution hence the name of microscopy super-resolution.

In the early '80s Scanning Probe Microscope (SPM) began to be used. In these years G. Binnig and H. Rohrer, two researchers at the University of Zurich, thought and realized an instrument that after five years would have brought them the Physics Nobel Prize: the STM(Scanning Tunneling Microscopy). In the same year by G. Binnig in collaboration with C. Quate and C. Gerber, a new scanning probe microscope derived from the AFM was invented. Today, after more than two decades, there are about ten instruments generated by these two founders, who remain the two basic types of SPM.

The scanning microscopy although a relatively new technique has been developed so quickly to allow to resolve many problems in the study of biology, materials science, microelectronics circuit structures and in the physics surface, finding application in various sectors, such as metals, semiconductors, ceramics, membranes, etc. The probe microscopy, allows both; acquire images with nanometer resolution and to provide precise information on the three-dimensional structure of the sample analyzed.

Before the invention of this technique, in fact, the images obtained with any other type of microscope, provided only an apparent three-dimensionality derived from an appropriate manipulation of the colours and of the tones of grey of the image.

The working principle of the SPM technique is very simple: the three-dimensional scanning of the surface of the sample is obtained via a probe that placed near the sample or in contact; (distance $\leq$ 200 nm) interacts with the surface of the sample, providing information point by point on the surface structure of the sample.

The different nature of the detectable interaction, depending by the type of the probe used, produces several variants of a scanning microscope probe. The three main variants are AFM (Atomic Force Microscopy), STM (Scanning Tunneling Microscopy) and SNOM (Scanning Near Optical Microscopy). While STM technique provides information with atomic resolution of samples using the tunnelling current (quantum effect that occurs at small distance between the probe and the sample), the AFM and SNOM techniques allow analysis of samples including non-conductors (such as organic in their natural environment), respectively through the measurements of repulsive forces surface and the changes in the optical near field.

1.1.2 Working Principe of AFM

Historically, Atomic Force Microscopy (AFM) was designed to measure the strong short-range repulsive forces between a tip and surface implemented as contact mode imaging. The probe (tip) is brought into contact with the surface (hence the name) and repulsive Van der Waals (VdW) forces result in the deflection of the cantilever, which is monitored by a photodiode.

The idea of scanning force microscopy, SFM, was discovered in 1986 by Binnig et al. [1986], as a topographical technique. A constant force is maintained between a cantilever and the sample, or in some cases a constant sample-cantilever tip distance is used, to measure the change in distance or force, respectively, hence having a topographic map of a sample. To measure these forces and distances a laser beam is focused onto the cantilever and is reflected onto a position sensitive photodetector. The signal is compared to the set point value chosen and the difference is used to calculate both the topographical data and to control the z position of the scanner, see figure 1.1. [1]

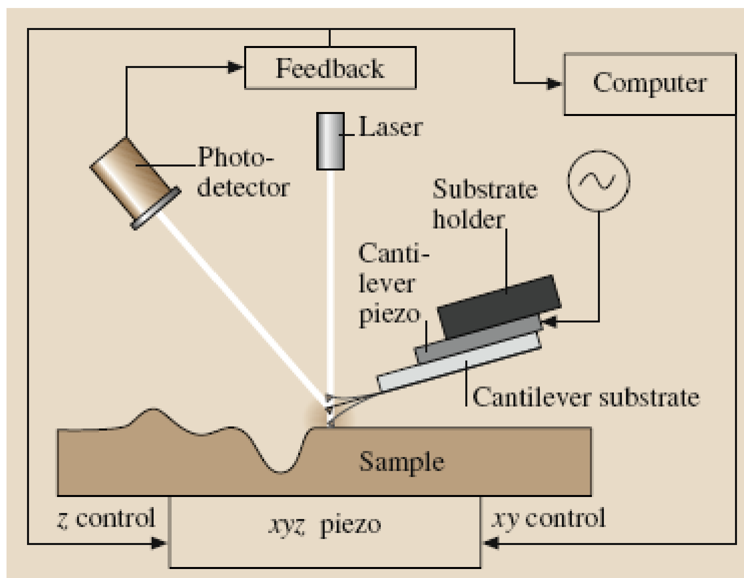

Fig. 1.1. Atomic Force Microscope Schema (AFM).

This is a versatile and non-destructive technique to make mappings of insulators, conductors, semi-conductors and is also used for biological applications. Cantilever shape and dimensions can strongly impact the quality of the image due to properties such as the mechanical resonance

frequency and force constant. Specifically, the resolution of the image obtained can be controlled, along with other factors, by the tip radius.

There are three modes in SFM: contact, non-contact, and tapping (intermittent) mode. In contact mode a repulsive van der Waals force is measured by the reflected laser signal as the cantilever tip is in close proximity (1−10) nm to the sample. Ideally, the cantilever should have a spring constant slightly lower than the effective spring constant holding the atoms of the sample together. In using a force too great between the cantilever and the sample any particles lying on the surface will be dragged around.

However, if one uses too small of a force the cantilever will not follow the topography. In general, this technique is good for large, non-uniform areas. In non-contact mode the cantilever is never in contact with the sample and the cantilever-sample forces are attractive, therefore the mechanical stiffness of the cantilever should be greater than those used for contact mode so that it does not get pulled into the sample. Here the cantilever is at distance of (1−100) nm above the sample, implying that the cantilever will have a longer life and that there is less potential for surface damage. In this method the cantilever is driven by a piezoactuator at a frequency just a bit higher than its mechanical resonance frequency, afterwards using amplitude modulation the topographical signal is extracted. Intermittent or tapping mode is similar to non-contact mode in many ways, however, the cantilever is vibrating (1−10) nm above the sample, where at the lowest point of its cycle the tip intermittently touches the sample.

A slightly lower frequency than that of the mechanical resonance frequency of the cantilever is used and again the topographical signal is extracted using amplitude modulation. Tapping mode at ambient temperature is possible, however non-contact operation is easier in

vacuum where air damping of cantilever oscillations is negligible, due to a much sharper mechanical resonance peak of the cantilever and hence higher sensitivity while measuring the shift in resonance frequency (fig. 1.2). [2-11].

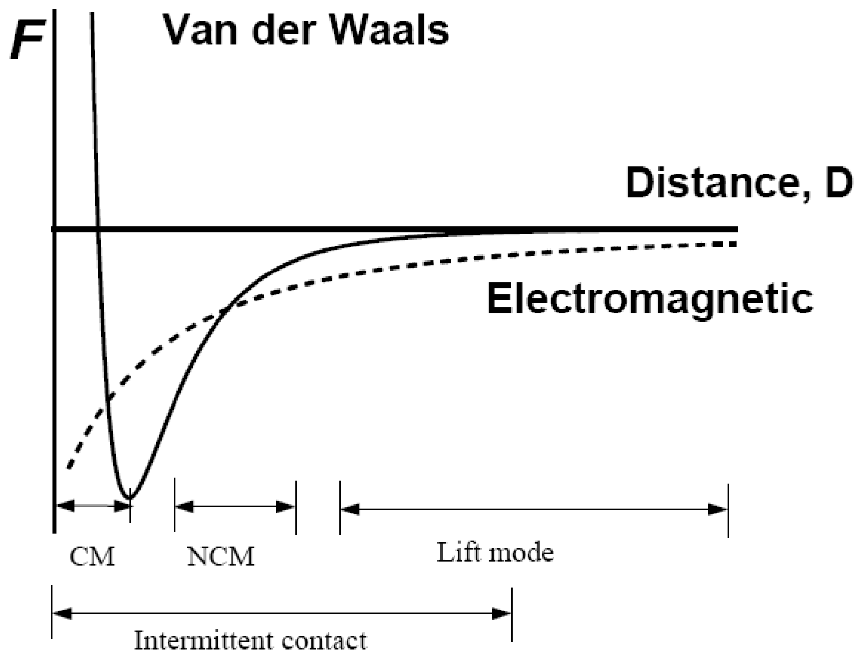

Fig. 1.2. Distance dependence of Van der Waals and electrostatic forces compared to the typical tip-surface separations in the contact mode (CM), non-contact mode (NCM), intermittent contact mode

1.1.3 Forces in AFM

It is obvious that in such a setup where two bodies are in close proximity, various kinds of forces, such as van der Waals, hydration forces and electrostatic forces will be present

In a force versus distance experiment, the tip moves from a large distance toward the substrate until the tip touches the substrate and,

therefore, it retracts to its original position. These forces can be characterized as follows:

Force	**Distance between Tip and Substrate**
No force	Large distance (mm)
Prior to touching	Attraction forces/tip bends downwards toward substrate
Almost touching	Repulsion forces/tip bends upwards
Touching	Contact/tip bent downwards

The magnitude of force is proportional to the cantilever spring constant multiplied by its deflection. In other words, AFM allows, the measurement of these forces in a simple way, as compared to other force apparatus. Prior to this AFM feature, forces at such close distances could not be measured under ordinary conditions.

However, in the current literature, a need for investigating these areas of application of AFM was found to be necessary.

Van der Waals Forces

The attractive forces present between the scanning force microscope tip and the sample at large separation is generally attributed to Van der Waals dispersion forces.

All bodies exert Van der Waals forces when their distance is of molecular size. The magnitude of Van der Waals forces is generally proportional to distance, r_d, as $1/r^6$, and is also called dispersion force. In this case, the tip, with radius R_{tip} is at a distance r_d from the substrate and the F_{vdw} (*vdw* = Van der Waals) force is given as:

$$F_{vdw} = A_{ham}R_{tip}/(6\ \mathrm{r_d}^2)$$

where A_{ham} is the Hamaker constant and is dependent on the polarizability of the materials. This relationship is not time retarded, hence, only valid for distances up to 10 nm and for tip radius R = 100 nm.

Electrostatic Force

An electrostatic force will exist between the tip and the substrate as a function of distance:

$$F_{el} = (q_1 q_2)/(4\pi\varepsilon D_d^{\ 2})$$

where q_1 and q_2 are the two charges, ε is the dielectric function of the medium, and D_d is the distance between the charges. Assuming a flat substrate, the electrostatic energy W_{el}, between the two charges and with capacitance C_c, at voltage U_v, can be given as follows:

$$W_{el} = 1/2\, C_c\, U_v^2$$

$$F_{el} = -\nabla W_{el}$$

In the limiting case, $D_d << R_{tip}$, one gets:

$$F_{el} = -(\pi\varepsilon R_{tip} U^2_{\ el})/D_d$$

Hydrophobic Forces

The special long-range force between hydrophobic macroscopic surfaces in water is called the hydrophobic force. This interaction is not completely defined, and there is probably more than one reason for which hydrophobic macroscopic surfaces attract each other, as many suggestions exist as regard to its origin. What seems perfectly clear, however, is that it is the water molecule and its unique properties that are the key components in this interaction phenomenon. The hydrophobic attraction

has been measured for distances up to 90 nm using a surface force apparatus. This attraction differs from short-range attraction between small hydrophobic molecules due to its anomalous long range of action. The interaction between hydrophobic molecules in water (i.e. hydrophobic interaction) plays an important role in the forces that stabilize the self-assembly of organized structures such as micelles, lipid bilayers, surface films, protein–lipid complexes and biological membranes.

The direct force measurements have revealed, somewhat unexpectedly, that the hydrophobic force is long range, for example, attraction beginning from distances greater than 50 nm is commonly measured. Despite a large number of studies reported in current literature, much remains to be investigated.

One important aspect that has not been extensively investigated is the manner in which the surfaces are prepared.

1.1.4 Piezoresponse Force Microscope

The first measurements of piezoresponse force microscopy, PFM, were done by Güthner and Dransfeld [1992]. They observed ferroelectricity by first applying a DC voltage between a conductive SFM tip, acting as top electrode and a bottom electrode and, hence, poling the ferroelectric vinylidene-fluoride trifluoroethylene copolymer film (VDF-TrFE).

The converse piezoelectric effect was then measured by applying an AC signal between the cantilever and bottom electrode, using a lock-in amplifier, amplitude modulation, to observe the phase and amplitude of the polarization. This converse piezoelectric effect forces a ferroelectric film to contract or expand under applied voltage depending on the orientation of polarization. The resolution in these first experiments was limited to 1μm, where higher resolution was obtained with topography.

They claim that this is due to the fact that Van der Waals forces decay much faster with distance than what the electric field forces generated by the AC voltage applied to the cantilever do.

With improvements to this technique it was later possible to observe ferroelectric domain patterns on the nanoscale by taking images of amplitude and phase of the local piezoelectric response, Colla et al. [1998] and Gruverman et al. [1996]. Alexe and Gruverman [2004] gave a thorough description of PFM and other SFM techniques. Hong et al. [1999] and Hong et al. [2001] gave a thorough description of the system we used and modified in this thesis. It is important for the frequency of the applied AC signal to be smaller than the mechanical resonance frequency of the cantilever and the AC voltage must be smaller than the coercive voltage in order to measure the converse piezoelectric effect. The phase shift of this piezoelectric vibration with respect to the phase of the applied AC signal will be around 0 or around 180 depending on the polarization orientation. Since in thin ferroelectric films the amplitude of the piezoelectric vibration is extremely small, on the order of Å, for correct phase detection a lock-in amplifier is indispensable.

The method of local piezoresponse imaging allows the direct visualization of the polarization distribution across the scanned area. Repetitive scans of this area can deliver information about stability of the created pattern and polarization losses due to back switching and other ferroelectric phenomenon.

There are two different ways to study the piezoresponse of ferroelectric films. The original experiments by Güthner and Dransfeld [1992] were using the configuration as noted in figure 1.3. The AC modulation voltage used was applied directly to the cantilever tip which scanned directly the ferroelectric film. When using the configuration of poling the ferroelectric layer directly, with the conducting AFM tip, care

must be taken in analyzing these results. This is because the emanating electric field from the conducting cantilever might not penetrate the whole ferroelectric film, Durkan et al. [1999]. Also the electric field distribution from the conducting cantilever is not trivial and can affect areas not directly in contact with the tip, Abplanalp [2001].

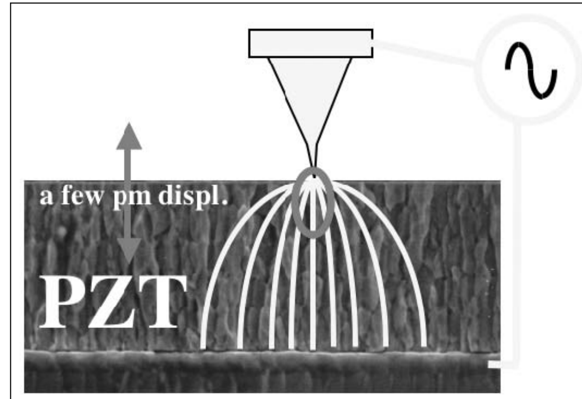

Fig.1.3 The electric field distribution when using a conducting cantilever tip is more difficult to model.

Later on Colla et al. [1998] wanted to gain further insight into ferroelectric capacitors that is Pt/PZT/Pt capacitors, and changed the original configuration to that viewed in figure 1.4. In this configuration the AC modulation voltage is still applied directly to the cantilever tip, however the tip is now scanning the top electrode of the ferroelectric layer. Using this setup it was possible to confirm that polarization suppression occurs region by region, or grain by grain. Also after cycling the capacitor with opposite fields it was possible to observe the fatigue or frozen regions, of dimensions 100nm-1μm. When capacitors are designed to such small dimensions this could become important. When applying the AC modulation voltage to the conductive cantilever tip the voltage seen locally by the ferroelectric layer is much higher than when studying a

capacitor structure through its top electrode. Also the electric field distribution in the ferroelectric layer is non-uniform when scanning directly the ferroelectric layer, unlike when studying the capacitor structure which has a uniform linear electric field distribution. Therefore it is not possible to directly compare the poling voltages when poling with the PFM directly on the ferroelectric layer and through a top electrode. [13]

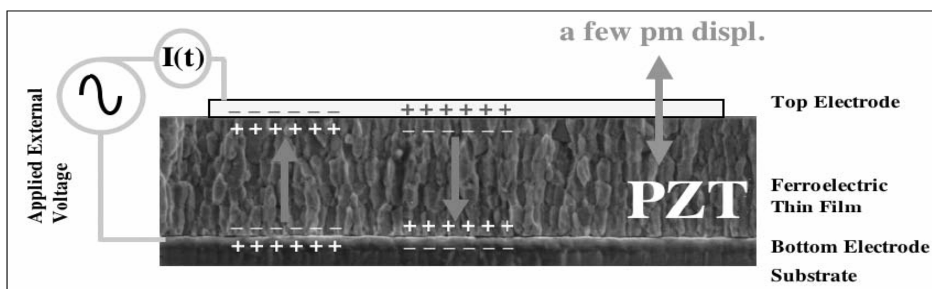

Fig. 1.4. The electric field distribution when studying the ferroelectricity through a deposited top electrode is simpler computationally. As it should exhibit a uniform electric field distribution from top electrode to bottom electrode.

11.5. Domain Writing

The great benefits of using ferroelectrics for domain writing are that they allow the creation of a reversible, non-destructive process. It is possible in using the Scanning Force Microscope, SFM, to modulate the spontaneous ferroelectric polarization by using a conductive cantilever with which a biasing DC voltage, either positive or negative, is applied locally to the ferroelectric layer.

The ferroelectric regions in which the tip of the cantilever has contact with will be poled with the according polarity. The poling of the spontaneous polarization in the ferroelectric layer can lead to the modulation of the current/resistance in a semiconductor channel. Reading of the modulation of the current in the channel can then be done using

electrical measurements. Using the SFM or PFM it is possible to write domains on the nanometer scale, paving the way for future possibilities in ferroelectric nanolithography.

As with the SFM there are many factors contributing to the quality and resolution of the piezoresponse image taken or the domain size written. The piezoresponse image and domain writing depend on the tip radius, frequency of the AC voltage, magnitude of the AC voltage, scanning rate, humidity, pressure and the tip/sample force. Written domain size depends on additional factors such as the sample thickness, transition temperature, crystallography, applied DC electric field, switching time, and cantilever/tip properties such as the metal coating. [14]

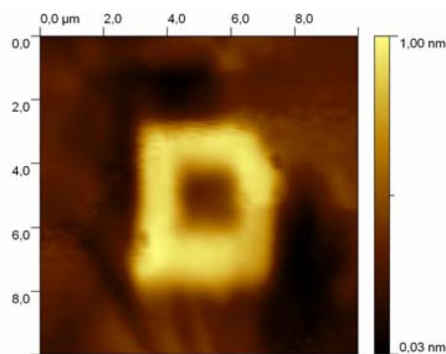

1.1.6. SNOM Instrument

In 1972, E. A. Ash and G. Nicholls, from the University College in London, demonstrated the near-field resolution of a subwavelength aperture scanning microscope operating in the microwave region of the electromagnetic spectrum. Utilizing microwaves, with a wavelength of 3 centimeters, passing through a probe-forming aperture of 1.5 millimeters, the probe was scanned over a metal grating having periodic line features. Both the 0.5-millimeter lines and 0.5-millimeter gaps in the grating were

easily resolvable, demonstrating sub-wavelength resolution having approximately one-sixtieth (0.017) the period of the imaging wavelength.

Near-field scanning optical microscopy (NSOM) is a type of microscopy where a sub-wavelength light source is used as a scanning probe. The probe is scanned over a surface at a height above the surface of a few nanometers (Fig.1.5)

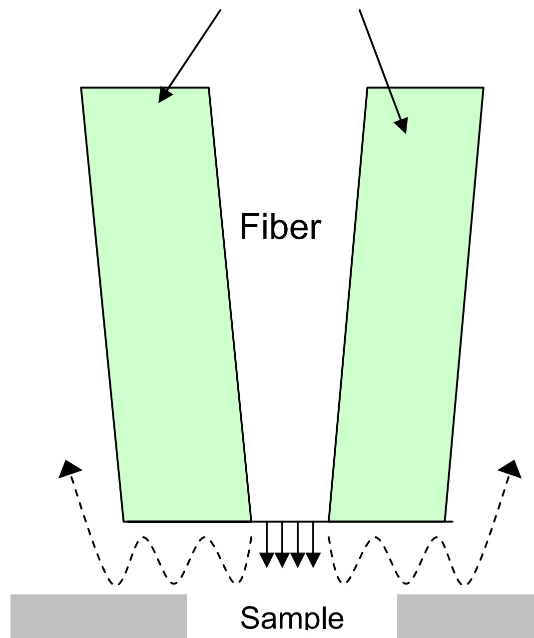

Fig.1.5. Schematic of near-field optical microscopy

While traditional optical spectroscopy has diffraction limited resolution of no better than 1/2 the wavelength (~200 nm for visible light), near-field spectroscopy surpasses this resolution limit and achieves subwavelength resolution (20 nm - 200 nm). In near-field spectroscopy, light propagates through a subwavelength size aperture (20 nm - 200 nm) in an opaque screen. Within the near-field the light is confined to an area on the order of the size of the aperture. The resolution of NSOM depends on the size of aperture used and the distance of the sample, but not on the wavelength of light. An image is generated by irradiating a small portion

of an object placed within the near-field of the aperture (tip) and scanning the sample.

We use, as a probe, a small aperture on the end of a tapered and aluminium-coated optical fiber (fig 1.6).

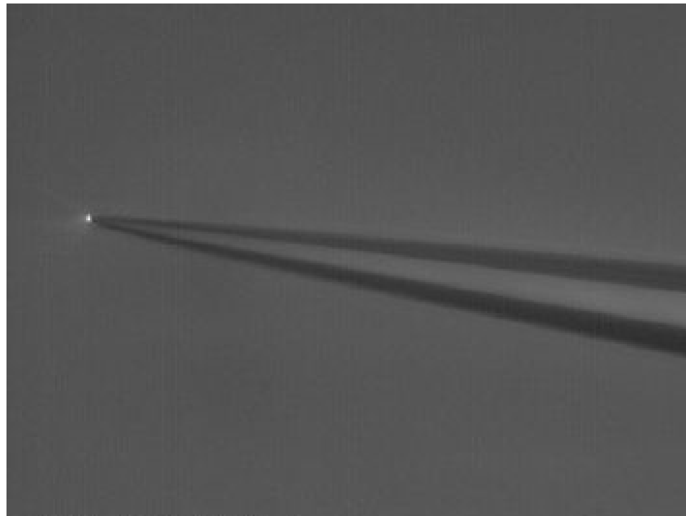

Fig 1.6. Optical microscope image of an NSOM tip.

We have been using NSOM (fig 1.7) to investigate the surface-induced orientation order at the nematic-isotropic (NI) phase transition for the liquid crystal 5CB and the results are shown in Chapter 6.

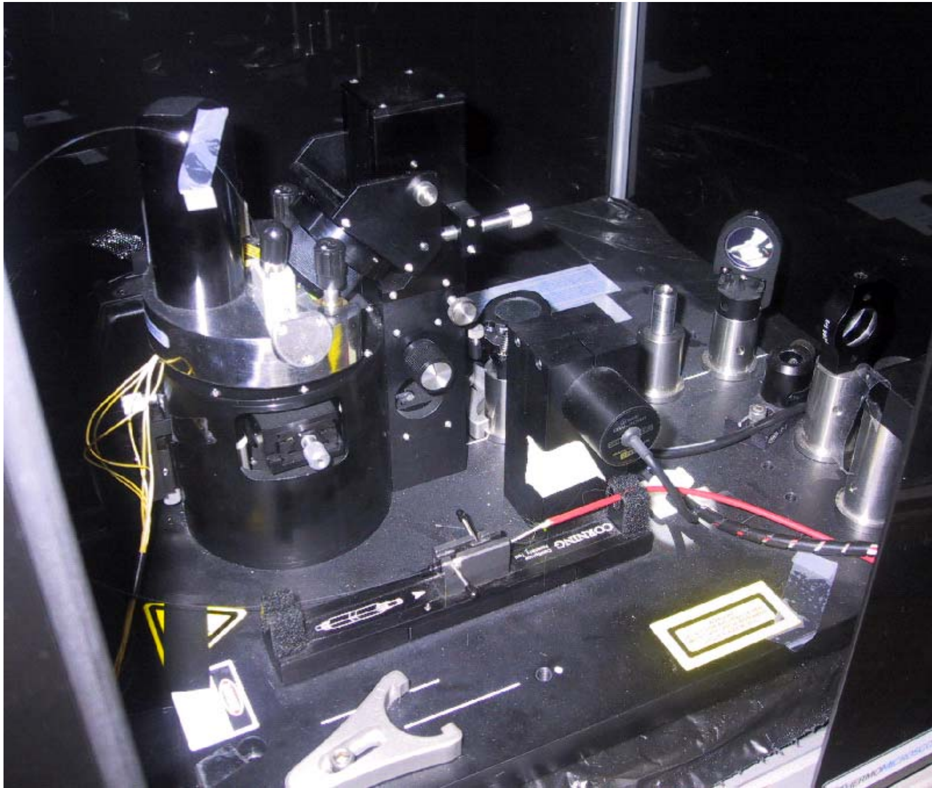

Fig 1.7. NSOM picture

1.1.7. NSOM measurement

Typically, laser light is fed to the aperture via an optical fiber. The aperture can be a tapered fiber coated with a metal (such as Al), a microfabricated hollow AFM probe, or a tapered pipette. Normally, the size of the point light source determines the obtainable resolution.

There are two types of feedback typically used to maintain the proper working distance of the probe and the sample. One method is quite similar to how feedback works with an AFM - by using a cantilevered probe, the normal force is monitored, typically by using a beam-deflection setup as in most AFMs. The second method uses a tuning fork. By attaching the fiber to a tuning fork, which oscillates at its resonant frequency, it can monitor changes in the amplitude as the tip moves over

the surface. The tip is moved laterally and this technique is normally referred to as "shear-force" feedback. Depending upon the sample being imaged, there are multiple modes of operation for NSOM.

Transmission: Light source travels through the probe aperture, and transmits through sample. Requires a transparent sample.

Reflection: Light source travels through the probe aperture, and reflects from the surface. Lower light intensity, and tip-dependent, but allows opaque samples.

Collection: Sample is illuminated from large outside light source, and the probe collects the reflected light.

Illumination/Collection: The probe both illuminates the sample and collects the reflected light.

Detection of the signal can be handled a number of different ways: Spectrometer, APD (Avalanche Photo Diode), Photomultiplier Tube, or CCD. In fig 1.8 is shown the SNOM operation schema for imaging.

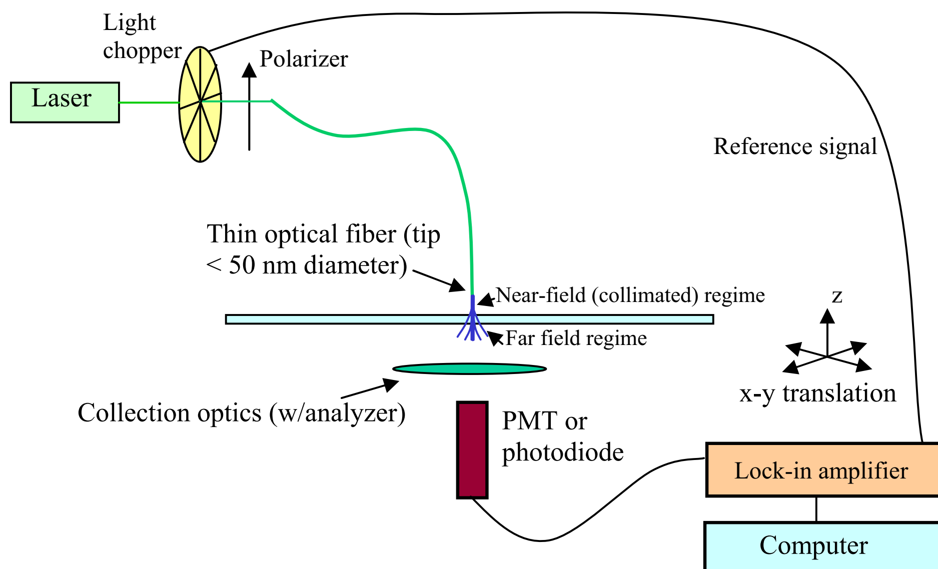

Fig. 1.8. Experimental configuration for near-field scanning optical microscope (NSOM)

1.1.8. STM

Local electronic properties became accessible after the invention of Scanning Tunnelling Microscopy. The rapid development of STM was due to the demonstrated atomic resolution and the ability to probe electronic structure (Scanning Tunneling Spectroscopy). However, dc current, feedback used in the vast majority of STMs, limits this technique to conductive surfaces. On semiconductive surfaces, tip-induced band bending severely limits the resolution.

Scanning Tunneling Microscopy (STM) is used to determine local atomic structure and Fermi level. The applicability of conventional STM is limited to conductive surfaces only. Tunneling occurs between two conductors (the probe, consisting of a thin metal tip and the sample) placed at different electrical potential, separated by a thin layer of insulation (e.g. air) which constitutes a potential barrier for electrons. The theory predicts that the evolution of the current depends exponentially on the thickness of the insulation, so it is possible to observe a tunneling current only at tip-sample distance of the order of a few Å.

However, with the STM technique, it is possible to obtain images with atomic resolution. If, between sample and the metal tip a small potential voltage (<1V) is applied, we have the passage of direct current of the order of nA that can be measured easily and used as feedback signal.

The flow of electrons depends on the sign of the voltage applied to the sample: if it is negative, the electrons pass from the filled electronic states to empty states in the tip and viceversa. Full or empty electronic states can be studied according to the sign of the applied voltage

The map of the area is generated by scanning the tip across the surface of the sample taking constant the tunneling current. In this way the vertical shift of the tip follows the constant density states during the scan.

The scanning technique is quite similar to the AFM, the only differences are the type of probe used in the interactions between tip and sample. In particular during the STM scan a voltage on the Z piezoelectric that controls the movement of approach and removal of the tip respect to the sample through a feedback loop is applied, namely the tunneling current is kept constant.

The image is built by storing the voltage applied to the piezoelectric crystal in the z direction, at every point of measurement. The calibration of the piezoelectric response can then convert this voltage in topographic variation.

Reference

[1] Sprinter Handbook of Nanotechnology 2003

[2] Franz J. Giessibl, Hartmut Bielefeld: Physical Review B 61,15 (2001)

[3] M. R. Jarvis, Rubén Pérez, M. C. Payne: Physical Review Letters 86, 7 (2001).

[4] M. Gauthier, N. Sasaki, M. Tsukada : Physical Review B 64, 085409 (2001).

[5] Kei Kobayashi, Hirofumi Yamada, Hiroshi Itoh, Toshihisa Horiuchi, Kazumi.

[6] Matsushige: Review of Scientific Instruments 72, 12 (2001).

[7] Michel Gauthier, Ruben Pérez, Toyoko Arai, Masahiko Tomitori, Masuru Tsukada: Physical Review Letters 89, 14 (2002).

[8] J. W. Hong, Sang-il Park, Z.G. Khim : Review of Scientific Instruments 70,30 (1999).

[9] Mischel Gauthier, Masaru Tsukada: Physical Review B 60, 16 (1999)

[10] Franz J. Giessibl: Physical Review B 56, 24 (1997).

[11] Nicolàs F. Martìnez, Ricardo Garcìa: Nanotechnology 17 (2006).

[13] Thesis: Ferroelectric Gate on AlGaN/GaN Heterostructures by Lisa Malin. Lausanne, EPFL 2007.

[14] Thesis: Nanoscale Electric Phenomena At Oxide Surfaces And Interfaces By Scanning Probe Microscopi by Sergei V. Kalini, University of Pennsylvania 2002.

Chapter 2

Pyroelectric, Piezoelectric and Ferroelectric materials

To better understand the piezoelectric phenomenon it is necessary to describe briefly the pyroelectricity and ferroelectricity, two effects related to the first and that involve the structure of the material.

2.1.1 Pyroelectricity

The pyroelectricity effect consists of the production of charges on the surface of a material if subjected to a uniform heating. This effect is related to crystal belonging to the class where there is only one polar axis with an electric dipole moment.

Pyroelectric materials are not symmetrical-center and exhibit a spontaneous polarization that can not be reversed through external electric fields. To explain the phenomenon of pyroelectricity we must consider that the crystal, retired, has a dipole different from zero. The uniform heating of the material causes a change in the intensity of the dipole, i.e. a compression or elongation of the material itself, and thus allows the formation of the pyroelectric phenomenon.

2.1.2 Piezoelectrics Materials

The piezoelectricity is a property found in many materials, which, subjected to mechanical forces, develop electric charges on their surface (direct piezoelectric effect) and, conversely, subjected to an electric field, show off a mechanical deformation (inverse piezoelectric effect). The first experimental demonstration between the macroscopic phenomenal piezoelectric and the crystallographic structure was published in 1880 by

Pierre e Jacques Curie, which measured the surface charge that appears on the crystals specially prepared undergoing mechanical effort.

The discovery of the opportunity to produce the piezoelectricity by applying a strong electric field to metal oxides synthesized in order to align their dipole domains, has enabled new applications piezoelectric and opened a new and intense area of research.

The first piezoceramic was titanium barium (Ba TiO_3), but today it has been replaced by titanium lead zirconate commercially known as PZT. The conventional process for the production of PZT is the mixing of metallic oxides. However this procedure involves some disadvantages such as the heterogeneity of composition and the volatilization of the lead oxides. The technique used for the production of PZT is the Sol-Gel process. A brief description of this process will be given later. The ability of piezoelectric materials to convert electrical energy into mechanical and vice versa depends on crystalline structure.

The necessary condition to obtain the piezoelectric effect is the absence of a center of symmetry in the crystal, which is responsible for the separation of charge between positive and negative ions and the formation of so-called Weiss domains, which are dipoles group with parallel orientation. Applying an electric field to a piezoelectric material, Weiss domains align in proportion to the field (Fig. 2.1).[1]

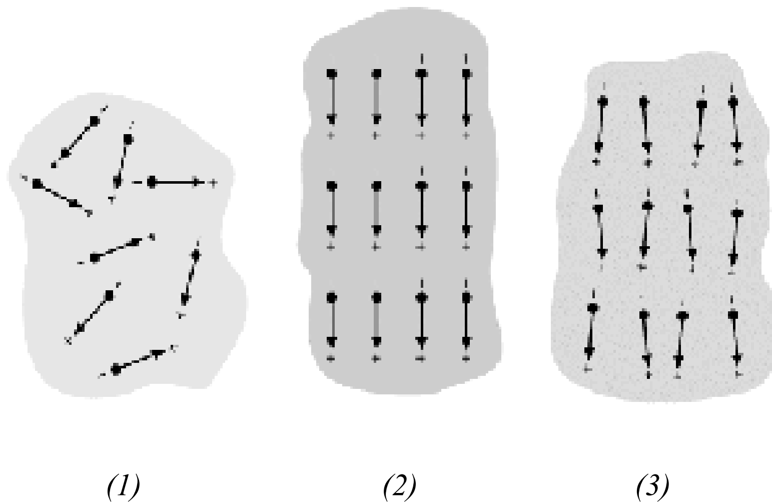

(1) (2) (3)

Fig.2.1. Electric dipoles in the Weiss domains, (1) No-polarization ferroelectric; (2) during the polarization; (3) after the polarization.

As a result, the size of the materials changes, increasing or decreasing if the direction of Weiss domains is the same or opposite to the field.

Generally in a ferroelectric crystal the domains are separated by walls that are the points where the orientation changes abruptly. The true polarization of the material will depend on the difference of the volumes directed upwards or downwards.

In fig. 2.2 the elementary cell of a PZT crystal is represented. The lead atoms are positioned at the corners of the cell unit and the atoms of oxygen centers face.

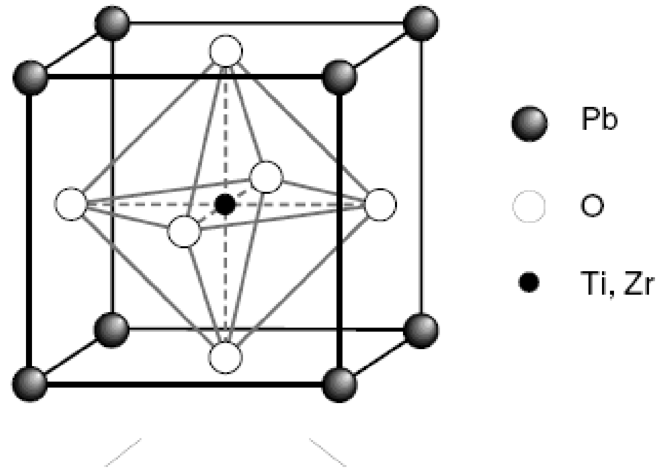

Fig. 2.2. Crystallographic structure of PZT

The proprieties of piezoelectric phenomena require preliminary definition of some mechanical quantities involved: mechanical stress, strain and the piezoelectric coefficient. The mechanical stress is the uniform pressure exerted on the material long one or more direction. This pressure is expressed in newton/metro^2 [N/m^2] and it is indicated with $\mathbf{T_i}$, where i = 1,2, ...6, according to the direction and to the surface in which stress is applied.

In fig. 2.3, since the piezoelectric crystal is a solid body $\mathbf{T_{23}=T_{32}}$, $\mathbf{T_{12}=T_{21}}$, $\mathbf{T_{31}=T_{13}}$, and moreover $\mathbf{T_{11}=T_{11}}$, $\mathbf{T_2=T_{22}}$, $\mathbf{T_3=T_{33}}$, $\mathbf{T_4=T_{23}}$, $\mathbf{T_5=T_{13}}$, $\mathbf{T_6=T_{12}}$.

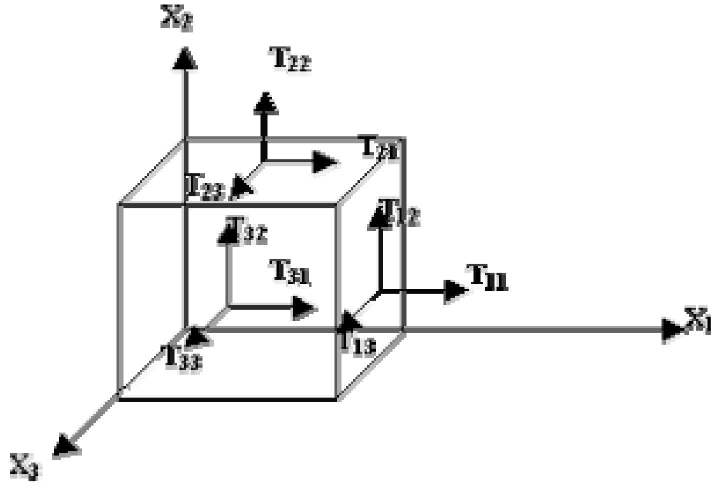

Fig. 2.3. Stress Components.

The Strain is the deformation that occurs in any solid body subjected to mechanical stress, it is a-dimensional quantity indicated with the symbol $\mathbf{S_i}$ with i=1,2,…..6, like the case of stress.

The piezoelectric charge constant, indicated with $\mathbf{d_{ij}}$**,** where the double subscript **i** and **j** (used to correlate electrical and mechanical quantities) show respectively, the direction of the electric field associated with the voltage applied or to the charge produced and the direction of the mechanical solicitation or of the deformation. The last is defined as the induced polarization in a material per unit mechanical stress applied.[2]

2.1.3 Ferroelectricity

The analogous electric of a ferromagnetic material is a ferroelectric material. The ferroelectric materials are also pyroelectric i.e. not center symmetric and are characterized by the ability to maintain a residual polarization even after an external electric field. A necessary condition so that a material has an ferroelectric behaviour is the absence of a symmetry center, that is the center of positive charge does not coincide with the

center of the negative charge even in the absence of an applied electric field.

The ferroelectric behaviour appears below a certain temperature. In fact it is characteristic of low temperatures, when increasing the thermal motion, the ordering of dipoles is destroyed. The temperature at which this happens is the ferroelectric Curie T_C temperature.

Above this temperature the amplitude of the thermal vibration is sufficient to prevent the formation of a set of oriented dipoles, and then the material has a paraelectric behaviour or simply not ferroelectric. By applying a different potential V on a dielectric substance the polarization **P** increases proportionality to the charge stored Q.

One of the simplest and most important characterization techniques to illustrate ferroelectricity in a material is the hysteresis loop measurement. This simple linear relationship between **P** and V or between **P** and **E** (electric field applied) does not apply to ferroelectric materials.
What is observed is a more complex behaviour, where the relationship between the polarization P and applied electric field is not linear, but is represented by a cycle of hysteresis as shown in Figure 2.4.

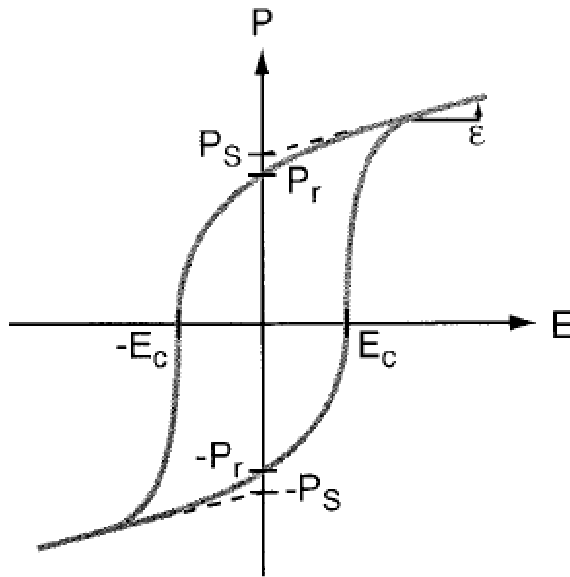

Fig 2.4. Macroscopic Hysteresis loop of a ferroelectric material. Where: P_S represent the spontaneous polarization ; P_r the remaining polarization; E_c coercive field .

The cycle should not necessarily be symmetrical respect to the axes **P** or **E**. In fact, the polarization, increasing the applied electric field is not reproduced when the field decreases. The ferroelectric shows a saturation of polarization, $\mathbf{P_S}$, with high electric field and polarization remaining $\mathbf{P_r}$, that is the value kept when **E=0**. The direction $\mathbf{P_r}$ is called ferroelectric axis, and its value $\mathbf{P_S}$ is called spontaneous polarization. [3]

2.1.4 Ferroelectric Materials

Ferroelectric materials exist in various compositions and forms. Single crystals of a material simplify studies of fundamental ferroelectric phenomena. The crystallographic orientation can be well controlled and intrinsic properties more easily accessed. However, single crystals are not

an option for many applications, because their costs are high. Ceramic materials can be processed, shaped and manipulated more easily and are therefore preferred in many, e.g. piezoelectric, applications. The most widely used ferroelectric, lead zirconate titanate, $Pb(Zr,Ti)O_3$ (PZT) cannot even be grown in single crystal form (large enough to be useful).

Apart from single crystals and ceramics, ferroelectrics are commonly deposited and used in the form of thin films. In micro-electro-mechanical systems (MEMS), but also for memory applications with high information density, this form is the most important; it is shortly discussed below.

2.1.5 Thin Films

With the age of miniaturization and computing, the interest in thin ferroelectric film grew fast. Thin films can be deposited in many different ways and consequently in many different phases and various degrees of perfection. The choice of a substrate is decisive for the quality of the films. Using appropriate single crystalline substrates, films can be grown with an orientation of the crystallographic axes that is fully controlled by the substrate. Such films are called epitaxial.

For more economic applications, methods were found to control the crystallographic orientation of the film and to achieve textured films with a preferential out-of-plane crystallographic orientation of the grains. Important parameters for the control of film growth are the lattice spacing, the thermal expansion coefficients of the substrate and the film, the temperature of the deposition, the material supply, the annealing process and other, more deposition technique specific parameters. An effective way to control the texture of a film is buffer layers that initiate the growth of crystals on the substrate. [4]

2.1.6 Memory Applications of Ferroelectric Materials

The ferroelectric bistability can be exploited for building memories, as the electrical polarization vector can be switched by an external field between two distinct stable states, up (”1”) and down (”0”). In order to switch at low voltages, the ferroelectric material must be necessarily a thin film.

A first device employing the memory effect in ferroelectric films was an array for a display with optical read out based on $Bi_4Ti_3O_{12}$ thin films. Switching was slow and the necessary high voltage was unsuitable for applications. Similar as in the case of magnetic hard disk drives, writing and reading of ferroelectric domains on a continuous thin film can be done by means of an appropriate probe head. In this case, reading and writing is performed only in a sequential order. The random addressing of individual bits using a word and a bit line is possible in random access memories. Here, the ferroelectric material has to be necessarily patterned into separated capacitors. [5,6]

2.1.7 (Lead Zircanate Titanate) PZT

As for the ferroelectric material, $Pb(Zr_x,Ti_{1-x})O_3$, short (PZT) was a straightforward choice since it has relatively low processing temperatures, approximately 570°C, high remanent polarization and low coercive field. PZT exhibits nucleation controlled growth and was also used in our experimental studies, described in chapter 5.

PZT was usually deposited at a composition of 47 % Zr and 53 % Ti and was deposited using sol gel methods, however limitations were imposed by the film thickness, high temperature annealing profiles and the large grain size. It was therefore of interest to investigate the growth of PZT on ITO (Indium, Tin oxide) and Silicon Wafer.

The phase diagram of the solid solution of lead zirconate and lead titanate is shown in figure 2.5

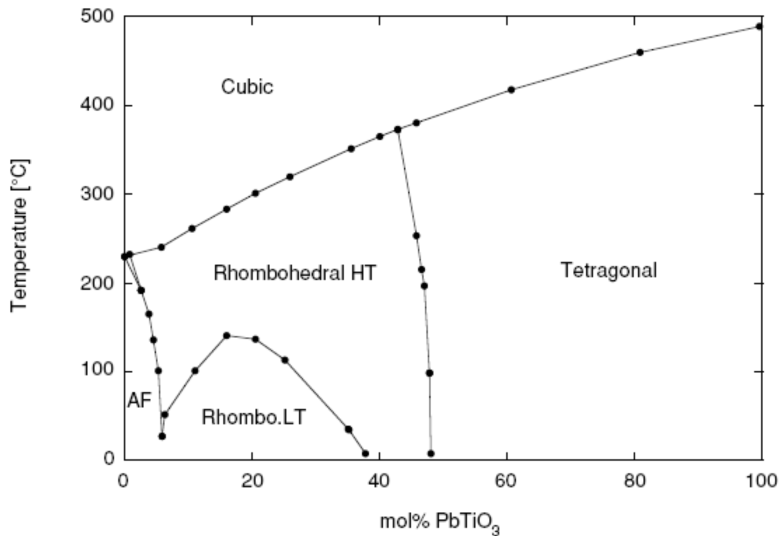

Fig. 2.5. Phase diagram for lead zirconate titanate exhibiting the cubic (paraelectric), antiferroelectric (AF), tetragonal and rhombohedral high/low temperature states

The phase diagram presents 3 main regions: the cubic paraelectric state, the antiferroelectric (AF) state around pure PZ and the ferroelectric state consisting of two types of rhombohedral phases (R3m at high temperature, and R3c at low temperature) and one tetragonal (P4mm). Detailed discussions of this solid solution are available. [7-12]

2.1.8 Sol-gel preparation

The sol-gel process is a technique widely used for the production of ceramics in the form of dust and films. The advantages of this technique are low temperatures the preparation of the materials and the possibility of

preparing in amorphous phase also materials difficult to obtain using other techniques, because quickly crystallizing. Moreover using the sol-gel process the material have a high degree of purity. The sol-gel technique is based on an appropriate molecular solution, which, as a result of chemical reactions, is transformed into a colloidal solution (sol), which, reacting further, it turns into a gel. The sol is obtained by dissolving appropriate quantities of the various precursors in an organic solvent, usually alcohol, then, through reactions, the hydrolysis and polycondensation, is switched to gel.

Lead Zirconate Titanate (PZT) thin films, with stoichiometric ratios indicated in the formula $PbZr_{0.47}Ti_{0.53}O_3$ were obtained by hybrid (carboxylate and alkoxides) sol gel route and spin coating deposition of the obtained mother solution on ITO (indium tin oxide)-glass substrate (sheet resistivity □$_s$ = 20 Ω/□, Unaxis GmbH) as detailed described in a previous paper [13].

The reagents (all supplied by Sigma-Aldrich) used are Lead(II) acetate trihydrate ($Pb(CH_3COO)_2{\cdot}3H_2O$, 99.999 %), Zirconium(IV) propoxide solution ($Zr(C_3H_7O)_4$, 70 wt. % in 1-propanol), Titanium(IV) isopropoxide ($Ti[(CH3)_2CHO]_4$, 99.999 %), Acetic acid glacial (CH_3COOH, 99.99+ %), n-Propanol anhydrous ($CH_3CH_2CH_2OH$, 99.7%), Ethylene glycol anhydrous ($HOCH_2CH_2OH$, 99.8%).

Briefly, the synthesis of the stock solution has been performed in “humidity free” Glove Box in Argon atmosphere (percentage of humidity and of molecular oxygen lower than 0.1 ppm). In order to obtain stable mother solution, the right amount (10.43 g considering the 10% excess in mole of lead, which compensate the lead loss (as PbO) which occurs during the process) of $Pb(CH_3COO)_2{\cdot}3H_2O$ have been dissolved in CH_3COOH by stirring and heating the solution up to 80°C for fifteen minutes. After two minutes at 80°C, the heater was set at 70°C and when

the solution was cooled down to the latter temperature, the stoichiometric amount of $Zr(C_3H_7O)_4$ solution, have been added. Later on, $Ti[(CH3)_2CHO]_4$, in its stoichiometric ratio, was added. When the solution is cooled down to room temperature, acetic acid has been added and the solution has been left to stir for 15 minutes. At this point 23.10 g of n-propanol and 1.16g of ethylene glycol have been added and again stirred and after 15 minutes the solution has been sealed and left to stir for one night.

Finally, the solution has been removed from the glovebox and 9 ml of bidistilled water have been added before the spin coating deposition.
The ITO glasses substrates were previously ultrasonically cleaned [6] and a SC10 CaLCTec s.r.l. spin coater has been used for the deposition of the mother solution. PZT thin films have been obtained at 1200 rpm for 25s. Such samples (Glass/ITO/PZT) have been placed on a hot plate for 5 minutes at 300°C. Later on, the films were subjected, for an hour, to different single thermal treatment in an oven in temperature range between 100°C and 800°C, each one separated by 100°C step.

The next step is to remove the solvent and water through a heat treatment with consequent formation of voids and subsequent collapse of the structure. In the gel state, usually, the structure is ordered only on very short scale of the magnitude of the first neighbors.

Through the heat treatment the energy of the atoms increase and itself to reorganize forming polycrystalline size of a few nanometers. Increasing the temperature has a further rearrangement of the polycrystalline and, therefore, to the formation of "rosette" crystal ever larger (fig. 2.6).

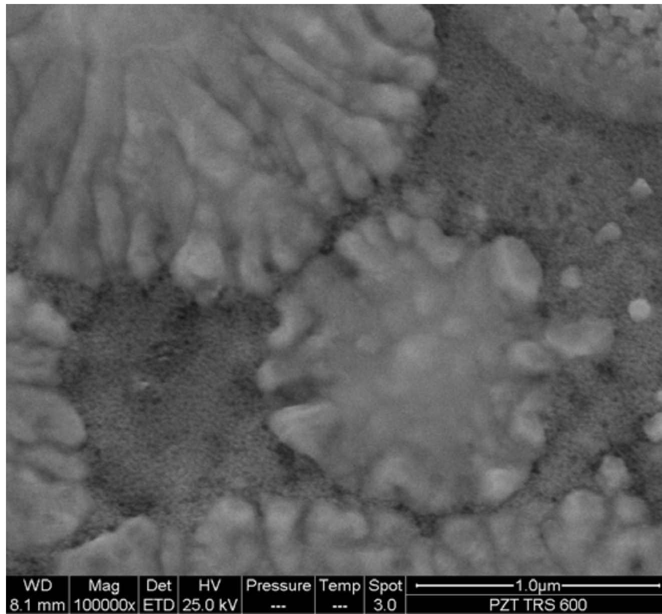

Fig 2.6 SEM Image of the PZT film deposited on Glass and ITO (Indium, Tin oxide) annealed at 600 °C.

References

[1] Thesis: Surface-Stimulated Phenomena in the Polarization Response of Ferroelectrics by Guiod Gerra Master of Philosophy, University of et de nationalité italienne 2008.

[2] Thesis: Investigation of ferroelectricity and piezoelectricity In ferroelectric thin film capacitors Using synchrotron x-ray microdiffraction by Dal-hyun do University Of Wisconsin-Madison 2006.

[3] M. Dawber, K. M. Rabe, J. F. Scott: Review of Modern Physics 77, (2005).

[4] Thesis: Polarisation Reversal in Ferroelectric PVDF and PZT Films by Roman Gysel. Diplomierter Werkstoff-Ingenieur ETH de nationalité suisse et originaire de Wilchingen (SH) 2008.

[5] H. Park, J. Jung, S. Kim, S. Hong, and H. Shin. Scanning resistive probe microscopy: Imaging ferroelectric domains. Appl. Phys. Lett., 84(10):1734, 2004.

[6] Y. Cho, K. Fujimoto, Y. Hiranaga, Y. Wagatsuma, A. Onoe, K. Terabe, and K. Kitamura. Terabit inch^{-2} ferroelectric data storage using scanning nonlinear dielectric microscopi nanodomain engineering system. Nanotechnology, 14:637, 2003.

[7] M.J. Haun, E. Furman, T.R. Halemane, and L.E. Cross, Thermodynamic theory of the lead zirconate-titanate solid solution system, Part IV: Tilting of the oxygen octahedra. Ferroelectrics, (1989) **99** p. 27-44.

[8] C.A. Randall, M.G. Matsko, W. Cao, and A.S. Bhalla, A transmission electron microscopy investigation of the R3m -> R3c phase transition in Pb(Zr,Ti)O3 ceramics. Solid State Com., (1993) **85** [3] p. 193-5.

[9] Thesis: softening and hardening transitionsin ferroelectric pb(zr,ti)o3 ceramics by Maxim Morozov. Maître ès Techniques et Technologies, Université Electrotechnique d'Etat de St. Pétersbourg, Russie 2005.
[10] Thesis: Patterned And Self-Assembled Ferroelectric Nano-Structures Obtained By Epitaxial Growth And E-Beam Lithography by Simon Bühlmann. Lausanne, EPFL 2004.
[11] Thesis: Extrinsic contributions to the piezoelectric Response of lead-based ferroelectrics by Gilles Robert. Lausanne, EPFL 2001.
[12] Thesis: Ferroeletricity at the nanoscale: study of sizes effects in lead titanate thin filmby Céline Lichtensteiger. Genere 2006.
[13] R. W. Schwartz, T. Schneller, and R. Waser, C. R. Chim. **7**, 433 2004.

Chapter 3

3.1.1 Experimental Techniques

This chapter will describe the technical characteristics of the microscope “Perception” used for measures.

In the following we describe a particular technique of measurement known as electrostatic force microscopy (EFM) very interesting to study the process of polarization of ferroelectric materials.

The development of scanning probe techniques, and more specifically electrostatic force microscopy (EFM), has provided a very important insight into the polarization reversal on a microscopic level. In the context of the traditional polarization reversal model with nucleation, forward and sideways growth, knowledge on the domain shape and details about its growth on a microscopic scale is of great interest, but could not be answered satisfactorily by the traditional PFM technique. The main shortcoming was that static observations of domain configurations and quasi-dynamical studies of domain growth were always performed on the surface of ferroelectric films.

Direct insight into the domain growth details is possible from observations of the domain structure and development during the switching process on the normal to the surface of ferroelectric films.

3.1.1 AFM technique

The Perception microscope consists of three blocks: microscope perception, electronics and software.

This instrument can be used as AFM, STM and SNOM changing one of the appropriate head. It’s composed of a lower structure for all

three techniques and of a top structure that can be changed depending on the type of configuration that is used (Fig. 3.1).

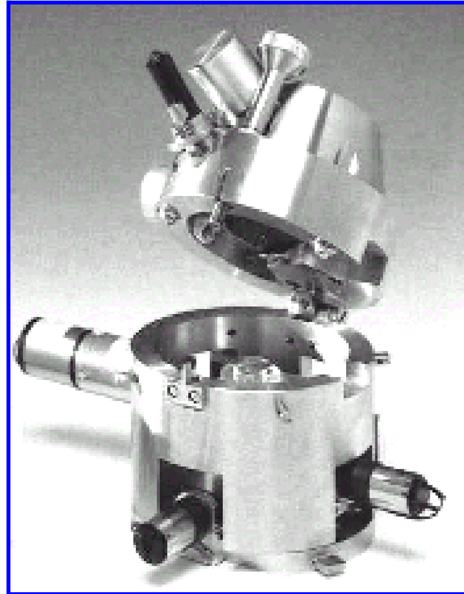

Fig. 3.1. Perception Microscope.

The lower portion of the microscope contains a stable that can accommodate samples with a diameter up to 6 cm and assembled on a piezoelectric scanner and three piezoelectric motors X, Y and Z which move on a macroscopic scale up to ± 3.5 mm in X, Y and ± 0.5 mm long z. The piezoscanner is composed of two empty cylindrical piezoceramic (see Figure 3.2) combined each other. At the end of the top piezo, which causes the movement along Z, is fixed a plug SM support on which the sample can be assemble. The lower piezo is divided into four perpendicular sectors, two for shift long X and two for the long Y.

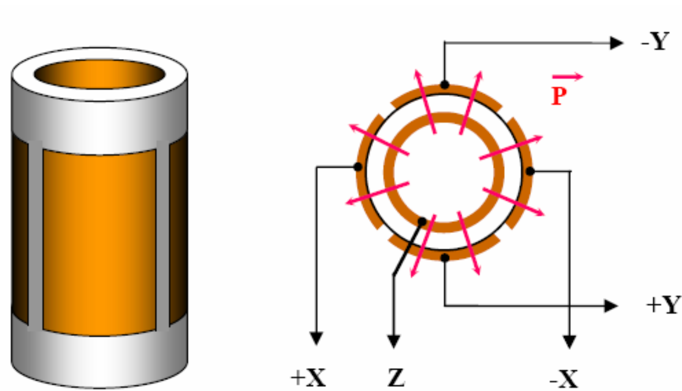

Fig. 3.2. Empty cylindrical piezoceramic.

The lateral shift (x,y) is obtained by bending the axis of the cylinder applying opposite voltage to the external electrodes and the vertical shift (z) by applying voltage to the central electrode.

During the acquisition of the image the movement of the Z piezo is activated and adjusted by the feedback circuit (Fig. 3.3), while the movements X, Y are controlled by the computer with DAC converter that generate two ramps of the synchronized voltage.

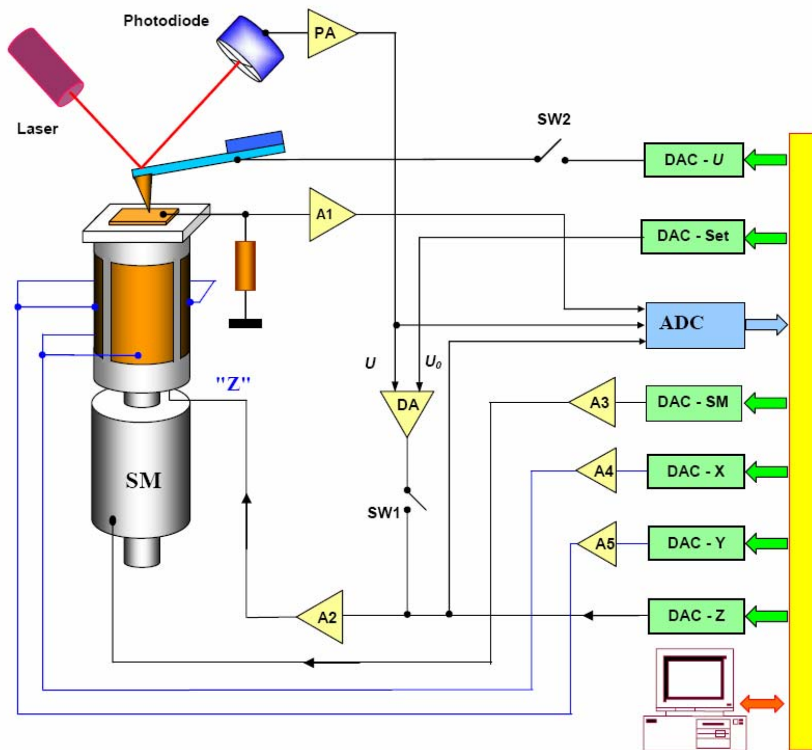

Fig. 3.3. Simplified Scheme of the Control System.

The scanner moves the sample along the X direction by steps of length L/N, where L is the linear dimension of the image and N is the total number of points that you want to acquire for each line. The scan at the end of the line will move of one step in the direction Y, and then runs another line after it is relocated to the point of departure.

In fig. 3.4 the fiber-sample movement in a Perception microscope is reported. [1, 2]

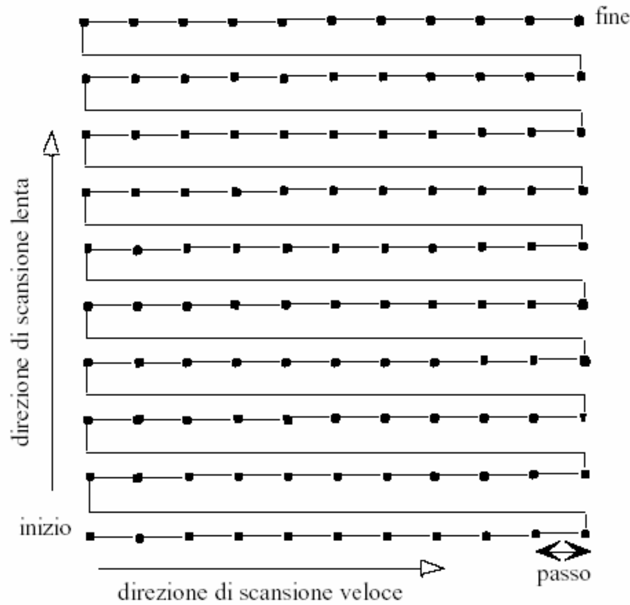

Fig. 3.4. Scheme of the Scanning Process.

The movement of the engines is completely controlled by the software for data acquisition, this allows the automatic approaching and the investigation of a large area of the sample acquiring and overlapping multiple images to obtain a complete image of the sample at high resolution. The AFM head contains the optic system for detecting the deflection of the micro lever.

The optical system is composed of a diode laser equipped with a lens system that provides a spot less than 5 microns. The diode is connected at the top of the head through a plate that can be adjusted across two micrometric screws spring.

The spot is focused on the back of micro lever which reflects it on a flat mirror that can be adjusted by two micrometric screws so that the laser, further reflected, is directed towards the center of a sensor (photodiode) composed of four quadrants (Fig. 3.5).

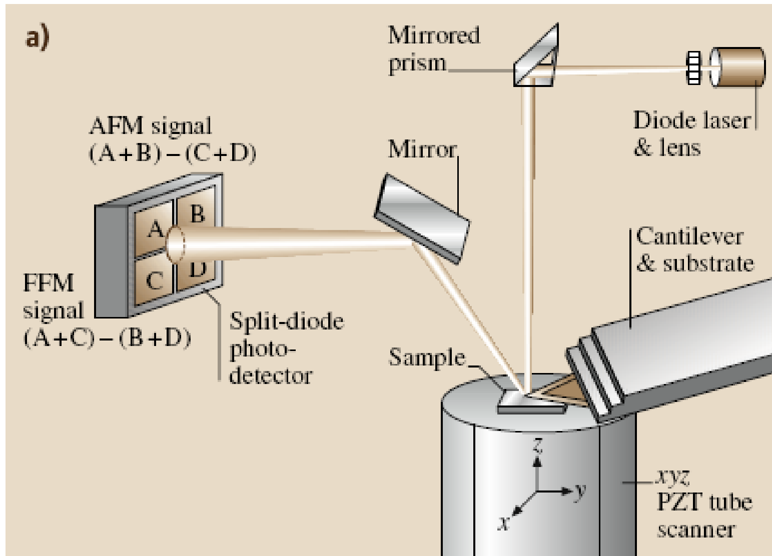

Fig. 3.5. Scheme Illustrative of the optic system for recording of the laser beam.

The four quadrants photodiode can record simultaneously and separately the vertical and horizontal displacement of the spot. The optic system can measure two quantities: the deflection of the cantilever due to the attraction or repulsive force Fz, (topography) and the torsion of the cantilever due to the lateral component F_L of the force of the interaction tip-surface (friction).

The deflection in either vertical or lateral direction is determined calculating the potential ratio of either (A + B): (C + D) or (A + D) : (B + C), where A, B, C, and D are the respective electric potentials proportional to the beam intensity on each quadrant. This current is converted into a voltage by a converter I/V. [3,4]

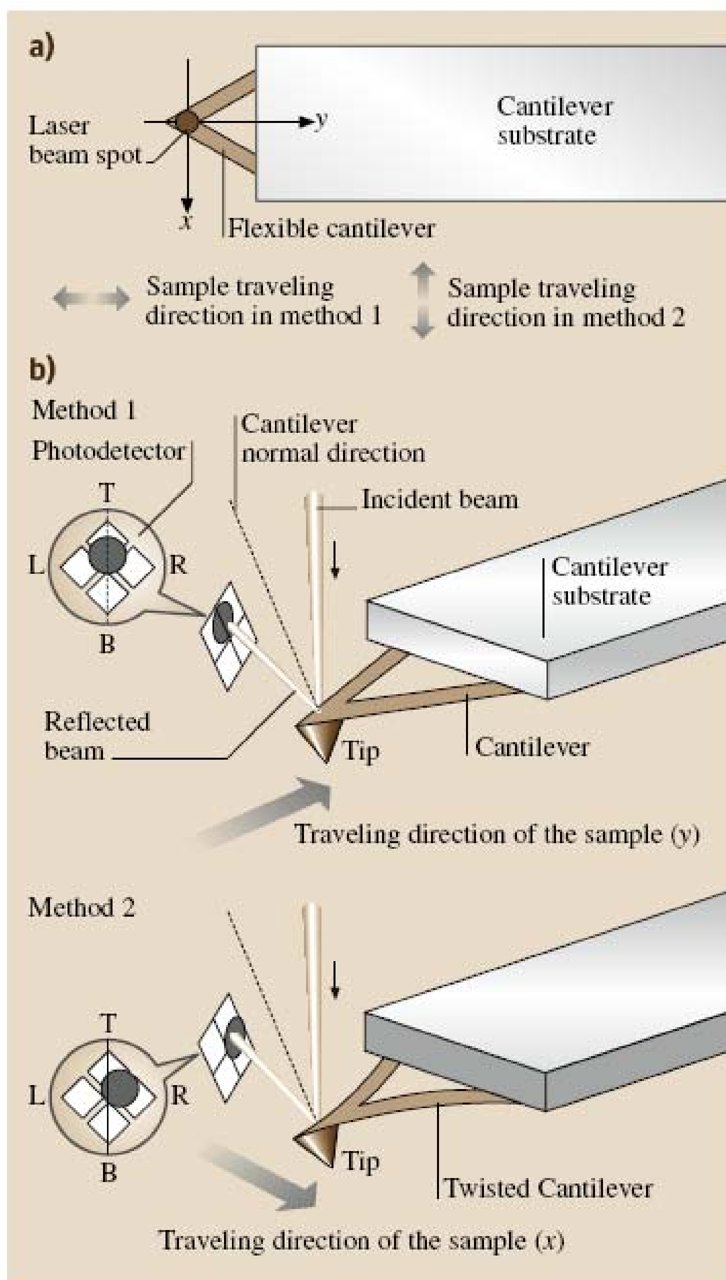

Fig. 3.6. Relationship between the various tapes of the deformation of the cantilever and the change of the position of the spot on the four quadrants of the photodiode.

In the SNOM head there is the resonant system. This system is made of a piezoelectric plastic powered by a sinusoidal voltage and a piezo bimorph susceptible to variations in amplitude of the fiber attached to it.

In the SPM head there is a preamplifier with an integrated stable in which the conductive tip is mounted. The interchangeable head of the instrument and the bottom are held together by a pin that allows the rotating of the upper part by allowing the change of the probe and the sample.

A screw ensures the rigid connection between the two parts and allows to vary the distance tip-sample microscopically. The anti-vibration stainless steel system is composed of a cylinder and a plate held in suspension by four springs on which the instrument is placed.

3.1.2 Electronics

The output signal, which, for the AFM, is the current detected by the photodiode, is converted into a voltage by a I/V converter and is sent to the circuit that compared the signal with the value "Reference" under which you want to work.

The output signal from the comparator is sent to the computer and stored as topography data and simultaneously, amplified and turned to feedback mechanism that operating on the piezo Z, keep a constant the tip-sample distance.

The output signal from the comparator is highest when the value of feedback is equal to that of reference, so that the error signal (the difference between the value of control and the reference) can be neglected.

3.1.3 Control Software

The control software, works essentially using the interface of the panels that help to place the instrument. In the experimental and mechanical setup panels, we assign the data for the control of the movement of the tip of the microscope, the value "reference", the initial positions scanners X, Y and all other parameters necessary for a correct acquisition of the image.

The setup values are sent to the electronic of the microscope using of the simple instructions with the interface constitute of the I-96 card.

The real-time image of the sample during the scan is displayed in a window on the monitor of the computer. The image is saved as a binary file and used by the application of graphics processing pv-Wave.

3.1.4 AFM and SEM Techniques

There are many analytical techniques to characterize ferroelectric materials that depend on the information that you want to obtain. To investigate the surface at high resolution, the two most commonly used techniques are the AFM and SEM, each of which allows to obtain resolutions of the order of nanometers.

The SEM presents enormous advantages compared to other microscopy techniques. The most important are the resolution, the depth of field and the ability to analyze the composition of the sample.
The following shows how a SEM image is produced, the principles that determine the resolution, the depth of field and the micro analytic ability.

All SEM consists of a column where the electronic beam is created and accelerated; a room for the sample that interacts with the beam; detectors that collect a variety of signals that result from the interaction beam-sample, a processing system that creates an image of the sample.

The electronic beam is created by an electronic gun. In the gun, placed on top of the column, an electrostatic field focuses the electrons emitted from a small region on the surface of an electrode on a small spot called crossover.

The gun accelerates the electrons towards the bottom of the column interacting with the sample at energies ranging from a few hundred electron volts to a few tens of keV.

The electron emerges from the gun as a divergent beam. A series of magnetic lenses and apertures in the column converge and focalize the beam on the crossover.

Near the bottom of the column a set of spool deflect the beam to a scan path on the surface of the material. The final lens focuses the beam in the smallest possible spot on the sample.

Fig. 3.7 shows the experimental setup of a SEM.

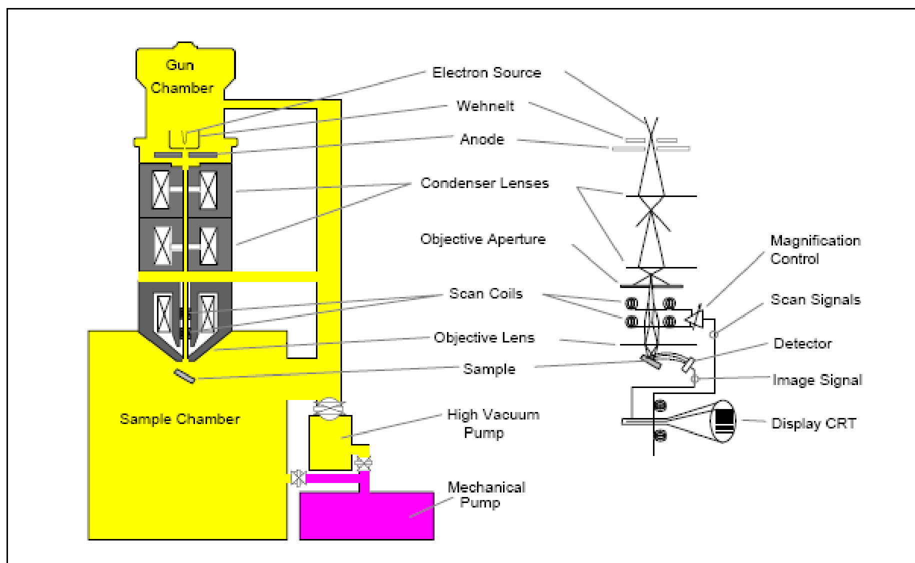

Fig 3.7. Scanning Electron Microscope schema.

The electron beam incoming inside the sample loses energy that is emitted in a variety of modes. Each emission mode is potentially a signal from which to create an image.

3.1.5 SEM image formation

On the contrary of the light in an optic microscope, the electrons, in a SEM do not give a real image of the sample.

The SEM forms a virtual image from the signals emitted by the material in question. A scan of the material with the electron beam is represented by a line path and, at every moment, the beam illuminates only a single point during the passage on the surface.

The signal that the beam generates moving from point to point varies in intensity, reflecting the differences in the sample.

In fig. 3.8 a graphic illustration of the signals generated of the interaction of the primary beam with the surface of the sample is shown.

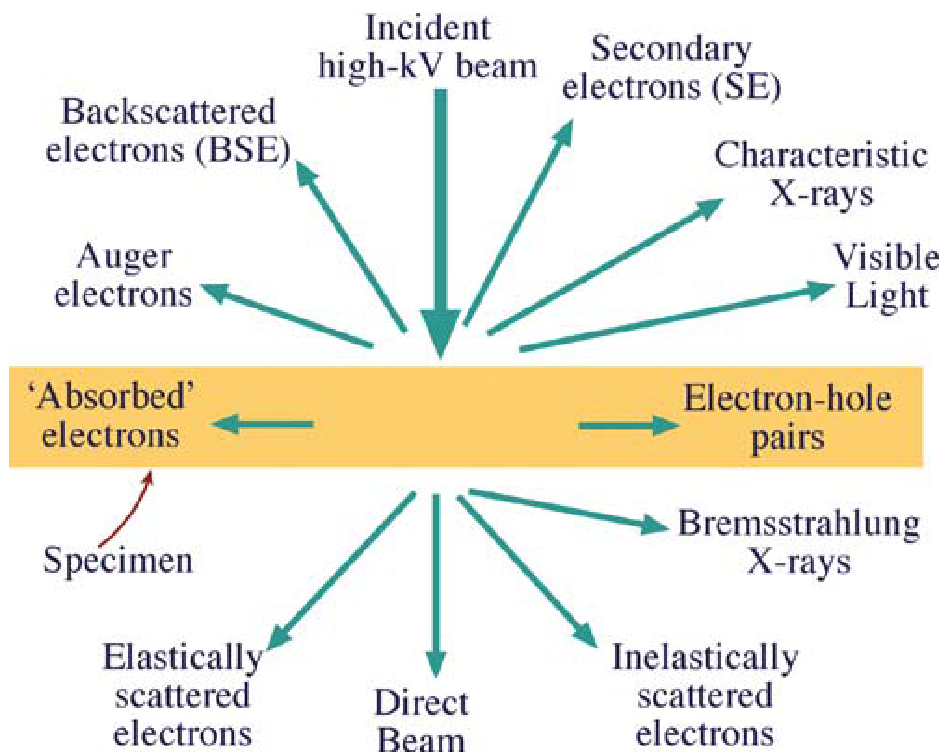

Fig. 3.8. Signals generated when a high-energy beam of electrons interacts with a thin specimen. Most of these signals can be detected in different types of SEM. The directions shown for each signal do not always represent the physical direction of the signal, but indicate, in a relative manner, where the signal is strongest or where it is detected.

There is a relation between the current beam and the measurement of the spot. An increase of one generally leads to an increase of the other. High-resolution images, on the other hand, require the smallest as possible size of the spot, whose lower limit is imposed by the current of the beam.

The information in a SEM is the variation of signal intensity. For beam currents and measurements of the spot below a critical value, the random signal variations are significant and the noise generated would compromise the resolution.

The SEM, in fact, can not resolve features smaller than the size of the spot. Generally, current low-intensity, short distances and high voltage acceleration produce smaller spot.

Other factors, such as the type of signal reflection, penetration of the beam and composition of the sample affect the resolution. The image signals are not only generated from the surface of the sample, the electron beam penetrates in the material and can interact one or more times in its path.

The region inside the sample from which the signal originates is called the volume of interaction.

Figure 3.9 is a schematic representation of the type of signal and of the volumes of specific interaction. In many cases the volume of interaction is significantly wider than the spot and thus becomes a real limit to the resolution of the instrument.

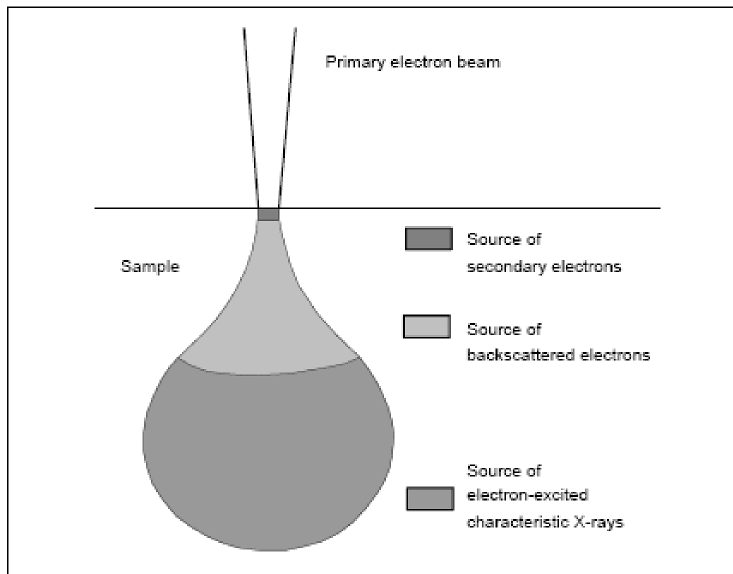

Fig. 3.9. Representation of the magnitude of the interaction volume due to the secondary electron, back diffuse electrons and X-ray.

The secondary electrons have a smaller volume of interaction. The composition of the sample affects the shape and the depth of the volume of interaction. Dense materials reduce the penetration of the beam and the distance that a signal can pass through before being absorbed. In the following we discuss the volume of interaction from which all the signals arise.

- Secondary Electron

From the principle of conservation of energy we know that any energy lost by a primary electron will appear as a gain in energy of the atomic electrons that are responsible for the inelastic scattering. If these are the outer-shell (valence or conduction) electrons, weakly bound (electrostatically) to an atomic nucleus, only a small part of this acquired energy will be used up as potential energy, to release them from the boundary of a particular atom. The remainder will be retained as kinetic energy, allowing the escaping electrons to travel through the solid as secondary electrons (abbreviated to SE or secondaries). As moving charged particles, the secondaries themselves will interact with other atomic electrons and be scattered inelastically, gradually losing their kinetic energy. In fact, most SEs start with a kinetic energy of less than 100 eV and, because the probability of inelastic scattering depends inversely on kinetic energy, the average distance that a secondary travels in the solid is very small, typically one or two nm.

As a result, most secondaries are brought to rest within the interaction volume. But those created close to the surface may escape into the vacuum, especially if they are initially travelling towards the surface. On average, the escaping secondaries are generated only within very small depth (<2 nm) below the surface, called the escape depth. Because the SE signal used in the SEM is derived from secondaries that escape into the

vacuum, the SE image is a property of the surface structure (topography) of the specimen rather than any underlying structure; the image is said to display topographical contrast.

-Back diffuse Electron

Back diffuse electrons (BSE) are mainly electron beam that were scattered back because of the elastic collision with atomic nuclei in the sample.

They have high energy, ranging from 50eV and energy of the primary beam. Their high-energy causes wide volume of interaction and consequently the resolution is worse.

The contrast in BSE image is produced primarily from the difference, point by point, in the average atomic number of the sample. Nuclei at high atomic numbers produce more electrons BSE and create the most brilliant areas.

X-Ray and microanalysis

X-rays products from the interaction of the energetic electron of the primary beam with the interior shell of the atomic of the sample allow the identification of the elements constituting the material. The X-ray energy of the atom uniquely characterizes the atomic that they emit.

In the fifth chapter there are some images made with the SEM on the samples of PZT prepared in our laboratories and the chemical analysis of the elements that form these samples.

3.1.6 Electrostatic Force Microscopy (EFM)

Electrostatic Scanning microscopy, with high resolution, allows us to obtain micrometric and nanometer information of the polarization processes that occur in ferroelectric thin films (PZT). This new

microscopy technique to allows, simultaneously, electrical topographic resolution and electrical characterization of the materials. The AFM was modified to work as an electrostatic force microscope (EFM), acquiring information not only on morphology, but also on the variations of the surface potential and forces gradient. EFM can also operate in the no-contact mode (NC-EFM) or contact (direct contact DC EFM) for the acquisition of both the electrical and topographical signal (fig. 3.10). [16]

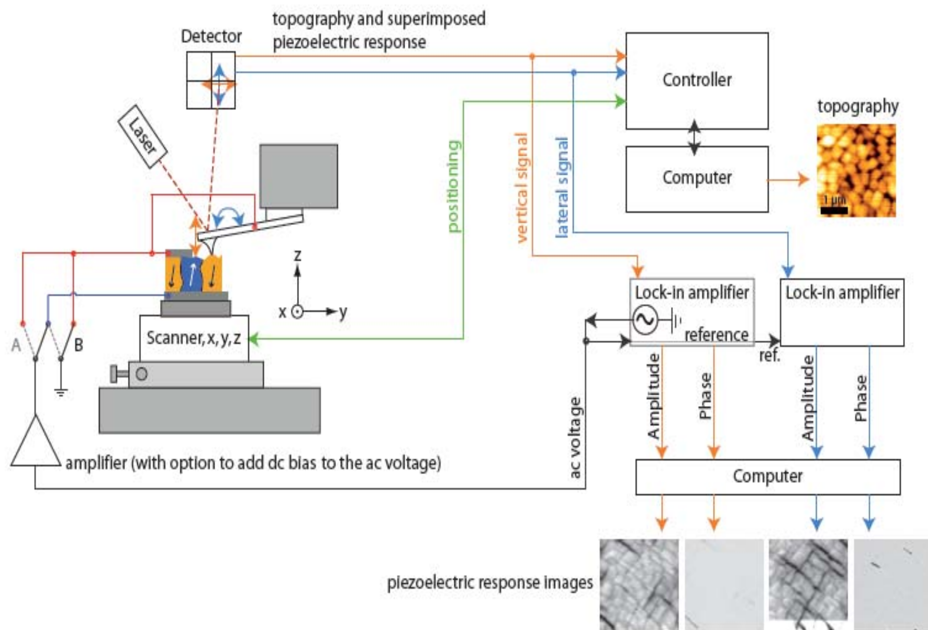

Fig 3.10. A schematic illustration of the EFM configuration with the AFM and its controlling unit, the lock-in amplifiers for vertical and lateral signal extraction, the computer unit to generate the topography image and the EFM images.

3.1.7 NC EFM

In this mode a circuit counter reaction of the AFM keep the tip sample distance constant in order to acquire the topographic signal. At the experimental set-up is added a DC and AC generator voltage and is made use of a lock-in instrument (Figure 3.17).

Tip and sample are required both conductors and their electrical contact is insured through a silver glue that ensures conductivity.

The force between the sample and the AFM tip is assumed to be proportional to the cantilever deflection, according to the simple Hooke‘s law:

$$F = kd$$

where F is the force, k the spring constant and d the deflection. The AFM tips are generally Si or Si_3N_4. The tips can be a pyramid, tetrahedric or conic shape, depending on the manufacturing process.

The lateral resolution of AFM image influenced by two factors: the size of the step of the scanning and of the minimum radius of the tip. The tip available has a radius of about 50 Å. The conical silicon tips, are more delicate and easily damaged than the silicon nitride tips, they have the advantage of being conductive by doping, and have a radius of curvature at approximately 10-20 nm. The pyramidal and tetrahedric tips (Si_3N_4) are more resistant and less suitable for mapping with narrow asperity or deep cracks.

The microscopes that work as EFM need that tip and sample are both conductors, the tips are conductive only if coated with a layer of metal (gold or silver). The deposition of material occurs not only at the tip, but also on the lever and on the silicon chip that supports the tip and on which the electrical contacts will be added. The SPM microscopes have the cantilever with elastic constant k optimum, i.e. lower than the elastic constant that holds together the atoms in a solid, that is 10-70 N/m.

The constant k depends on the shape, the size and material of which the cantilever is composed.

The thicker and courts cantilever tend to be stronger and to have resonance frequencies higher. The commercial cantilever has the elastic constant k which varies in the range 10-3-100 N / m, while the resonance frequency is between 1-350 kHz.

In Figure 3.11 is depicted a cantilever with silicon-nitride pyramid tip. [5-14].

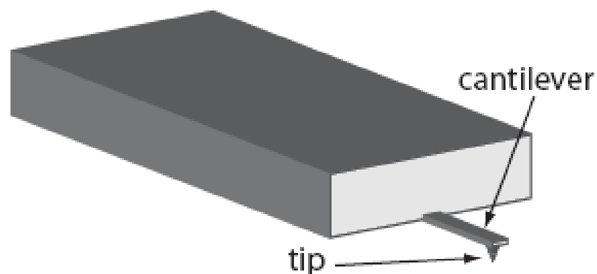

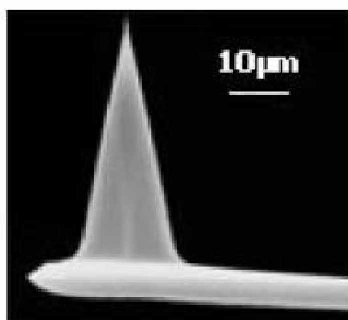

3.11. Rectangular Cantilever and silicon-nitride pyramid tip

Analysis of the force

When you run a scan between tip and sample an AC (Vac) and DC (Vdc) voltage are applied at the frequency (f) and a. The frequency of the voltage from the function generator (the order of tens kHz) is much lower than that of its instrument that operates in no-contact mode (the order of hundred kHz). This means that the two signals are distinguishable from one another without overlapping. The signal from the laser reaches the photodiode, containing information on the topography and electrical signal between the tip and the sample and then is sent to a Lock-in that selects the frequency f and sent the form to a microscope.

On the same area of the sample it is possible to obtain simultaneously two signals: the topography and f –EFM. The atomic force on the tip is compensated by a repulsive force to short-range and an attractive force to long-range (Van der Waals Force). This force shows a complex behaviour that depends on the tip-sample distance.

The basic principles of the DC-EFM for the measure of the contrasts domain is to detect the electrical field generated by a charge surface through a modulation technique in which the DC-EFM works in contact mode.

In the presence of a charge surface $\sigma_b=\mathbf{P}\cdot\mathbf{n}$ the force on the tip, in presence of a charge surface, is composed of an atomic force F_a and an electrostatic force F_e.

If there is a voltage electrostatic, force F_e is the sum of a capacitive force $\frac{1}{2}\left(\frac{\partial C}{\partial z}\right)V^2$ and a force of Coulomb. The Coulomb force is present since there is an electrical interaction between the electric charge induced on the tip $q_t=CV$ and the electric field E, due to the charge surface density on the sample where C and V are the capacity and the voltage applied between the tip and the sample.

The capacity C is the combination in series of the tip-sample capacity C_t and of the capacity C_s of the sample i.e. $C_t C_s / C_t + C_s$. The electrostatic force on the tip is

$$F_e = -\frac{\partial U}{\partial z} = -\frac{V^2}{2}\frac{\partial C}{\partial z} \qquad (3.19)$$

where U is electrostatic energy, z is the normal direction to the surface, C is the capacity between tip and sample and

$$V = -V_S + V_{dc} + V_{ac} \mathrm{sen}\,\omega t \qquad (3.20)$$

where $\omega = 2\pi f$ and V_S is surface potential of the sample respect to the tip and is $V_S = A_C - A_P$ where A_C and A_P are respectively the contact potential of the sample and of the tip.

V_S depend on the local proprieties of the sample and then it can be changed during the scan on the surface. Combining the equation 3.19 and 3.20 one obtains:

$$F = -\frac{1}{2}\frac{\partial C}{\partial z}\left[\left(V_{dc} - V_S\right)^2 + \frac{1}{2}V_{ac}^{\ 2}\right] +$$

$$-\frac{\partial C}{\partial z}\left(V_{dc} - V_S\right)V_{ac} sen\omega t + \frac{1}{4}\frac{\partial C}{\partial z}V_{ac}^{\ 2}\cos(2\omega t) = \qquad (3.21)$$

$$= F_0 + F_1 sen\omega t + F_2 \cos 2\omega t$$

F_1 and F_2 are proportional to the capacitive gradient $\partial C / \partial z$. Changing V_{dc} so that F_1 is zero, V_S can be directly measured. Dividing the equation 3.19 for F_1 and F_2 and eliminating the term of the capacitive gradient one obtains V_S depending on the position.

$$\left|\frac{F_1}{F_2}\right|\frac{V_{ac}}{4} = \left|V_{ac} - V_S\right| \quad (3.22)$$

3.1.8 DC EFM

Also in this modality, as in previous, the topography is obtained in contact mode, while the electric signal is obtained recording the vibration of the lever to the frequency f. In the descriptions of the piezoelectric material their ability to deform under the action of an applied electric field has already been emphasized. When these materials are polarized their thickness changes as a function of a voltage applied between the electrode upper and lower because of the inverse piezoelectric effect.

If the voltage applied is a signal a.c. the answer will change according to the different states of the polarization. The thickness of the film will increase by applying a voltage parallel to the polarization, viceversa, it will decrease if a small voltage is applied to the opposite direction of the original polarization.[15]

3.1.9 X- Ray Technique

One characterization of the deposited crystalline phases of thin films is X-ray diffraction.

X-rays are electromagnetic radiations with wavelengths of approximately 1Å (10^{-10}m). The wave nature of x-rays has been studied since the first x-ray diffraction experiment in 1912. Since then, x-ray diffraction has been an important method in understanding the internal structure of matter.

We determined the crystallographic orientation of the PZT samples using laboratory x-ray diffraction studies. The results of the diffraction measurements of the PZT films are shown in the chapter 5.

We use θ-2θ scans. In this measurement the detector and the sample surface are scanned relatively to the fixed source in a way that the normal surface always cuts the angle between the source-sample and sample-detector in halves (i.e. if the sample rotates by θ, the detector has to do a 2 θ step). According to Bragg's condition for constructive interference, there is an X-ray peak intensity at the condition $2d\sin\theta = n\lambda$ (d: spacing of an atomic plane, θ: angle between source and the sample surface, $\lambda = 1.5406$Å for Cu_a X-ray emission). In this way, the reciprocal lattice vector r* is always perpendicular to the substrate plane. This means that only the crystal planes parallel to the substrate can be observed.

This measurement does not give information about the in-plane orientation of the film. It only shows its orientation with respect to the normal substrate.

References

[1] U. Hartmann An Elementary Introduction to Atomic Force Microscopy and Related Methods. Institute of Experimental Physics, University of Saarbrücken D-66041 Saarbrücken, Germany 2005.

[2] N. Ashkenov*, M. Schubert, E. Twerdowski, H. v. Wenckstern, B.N. Mbenkum, H. Hochmuth, M. Lorenz, W. Grill, M. Grundmann, Thin Solid Films 486, 153– 157(2005).

[3] Sprinter Handbook of Nanotechnology 2003.

[4] New insights into ferroelectric domain imaging with piezoresponse force microscopi: Tobias Jungk, Akos Ho®mann, and Elisabeth Soergel University of Bonn, Institute of Physics, Wegelerstr. 8, 53115 Bonn, Germany 2008.

[5] Franz J. Giessibl, Hartmut Bielefeld: Physical Review B 61,15 (2001)

[6] M. R. Jarvis, Rubén Pérez, M. C. Payne: Physical Review Letters 86, 7 (2001).

[7] M. Gauthier, N. Sasaki, M. Tsukada : Physical Review B 64, 085409 (2001).

[8] Kei Kobayashi, Hirofumi Yamada, Hiroshi Itoh, Toshihisa Horiuchi, Kazumi.

[9] Matsushige: Review of Scientific Instruments 72, 12 (2001).

[10] Michel Gauthier, Ruben Pérez, Toyoko Arai, Masahiko Tomitori, Masuru Tsukada: Physical Review Letters 89, 14 (2002).

[11] J. W. Hong, Sang-il Park, Z.G. Khim: Review of Scientific Instruments 70, 30 (1999).

[12] Mischel Gauthier, Masaru Tsukada: Physical Review B 60, 16 (1999).

[13] Franz J. Giessibl: Physical Review B 56, 24 (1997)

[14] Thesis: Theoretical Modelling of Non-contact Atomic Force Microscopy on Insulators by Adam Foster. University College London 2005.
[15] Thesis: Atomic force microscopy studies of ferroelectric domains in epitaxial $PbZr_{0:2}Ti_{0:8}O_3$ thin films and the static and dynamic behavior of ferroelectric domain walls by Patrycja Paruch. Genève 2003.
[16] Thesis: Polarisation Reversal in Ferroelectric PVDF and PZT Films by Roman Gysel. Suisse 2009

Chapter 4

Qualitative analysis of the tip-sample interaction in AFM Probe Microscopy

The primary objective of this chapter is to understand the mechanisms linking the deflection of the cantilever to the topographical and electrical information when using the two EFM techniques, namely contact and no contact mode.

4.1.1 Cantilever oscillations

The effects of the cantilever deflection produced by the ferroelectric and piezoelectric proprieties of a material are analyzed in this paragraph.

The surface deformations, e.g. caused by the inverse piezoelectric effect, interact with the tip to play an important role in the contact images. Once the interactions are known, the deflection of the cantilever can be predicted for different states of the sample, e.g. for different directions of the spontaneous polarization.

The understanding of the deflection of the cantilever is important because the deflection is monitored accurately in all mode of the AFM. For example, any contrast observed for polarized inversely domains in a ferroelectric is produced by different interactions with these domains.
The exact derivations of the oscillation cantilever in the AFM requires the use the mathematical techniques quite complex.

However, the main characteristics of the processes that happen during the interaction of the oscillating cantilever with a surface can be

understood on the basis of elementary mathematical models. The cantilever has to be considered as a mass-free rod (with elastic constant *k*) with an end joined to a bimorph and a mass m located on the tip (fig. 4.1).

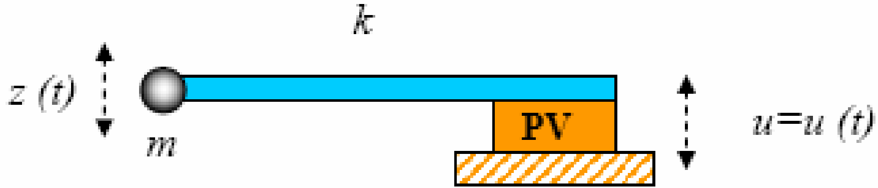

Fig. 4.1. Cantilever with a tip of mass m at the end.

Let us suppose that the bimorph fluctuates at a frequency ω with:

$$U = U_0 \cos(\omega t) \tag{4.3}$$

The equation of motion for the tip of the system is described by:

$$m\ddot{z} = -k(z-k) - \gamma\dot{z} + F_0 \tag{4.4}$$

where:

- M is effective mass of the tip;
- z is tip displacement;
- k is the cantilever spring constant;
- γ is damping coefficient. In the term γ the viscous force (force strength of the fluid in which the tip is immersed) are taken in account;
- F_0 represents the gravity force and the other constant forces.

A constant force produces only a shift of the equilibrium position of the tip and does not affect the frequency, amplitude and phase of the oscillation.

So with the replacement of variable $Z=Z_1+F_o/k$, the equation of motion of the shift Z_1 from the equilibrium position becomes:

$$m\ddot{z} + \gamma\dot{z} + kz_1 = kU_0 \cos(\omega t) \qquad (4.5)$$

Said $\omega=\sqrt{(k/m)}$ and

$$Q = \frac{m}{\gamma}\omega_0 \qquad (4.6)$$

(quality factor), the eq. (4.4) becomes

$$\ddot{z} + \frac{\omega_0}{Q}\dot{z} + \omega_0^2 z_1 = \omega_0^2 U_0 \cos(\omega t) \qquad (4.7)$$

(where ω_o is the frequency of the free oscillation).

The general solution is the overlap of a damping oscillation with the damping constant $\delta=\omega_o/2Q$ and a persistent oscillation forced with frequency ω.

The stationary oscillations of the equation 4.7 are in the form

$$\eta = a \times e^{-i\omega t} \qquad (4.8)$$

with

$$a = \frac{\omega_0^2 U_0}{\omega_0^2 - \omega^2 - i\frac{\omega\omega_0}{Q}} \qquad (4.9)$$

The amplitude module of the forced oscillation is

$$A(\omega) = \frac{U_0\omega_0^2}{\sqrt{\left(\omega_0^2-\omega^2\right)+\frac{\omega^2\omega_0^2}{Q^2}}} \qquad (4.10)$$

The complex phase amplitude (a) respect to the term forced oscillation

$$U = U_0 \cos(\omega t)$$

is

$$\varphi(\omega) = arctg\left[\frac{\omega\omega_0}{Q\left(\omega_0^2-\omega^2\right)}\right] \tag{4.11}$$

At frequency ω_o the oscillation amplitude of the tip is: $A(\omega) = QU_0$, i.e. is proportional to the quality factor. However, the presence of dissipation ($\gamma\neq 0$ i.e. $Q\neq\infty$) in the system produces a decrease in the resonant frequency of the cantilever, given by

$$\omega_{ris_1}^2 = \omega_0^2\left(1-\frac{1}{2Q^2}\right) \tag{4.12}$$

The resonance frequency shift of the dissipative system is

$$\Delta\omega = \omega_0 - \omega_{ris_1} = \omega_0\left(1-\sqrt{1-\frac{1}{2Q^2}}\right) \tag{4.13}$$

When increasing the dissipation, the characteristic curve amplitude-frequency of the system is shifted at lower frequency. Moreover, for typical values of the quality factor of the cantilever in the air, the resonance frequency shift due to the dissipation is small. The dominant effects of the dissipation are essentially the decrease of the oscillation amplitude and the enlargement of the amplitude profile and of the phase system (for different values of ω).

4.1.2 Cantilever oscillation in the no-contact mode

In the no-contact mode the amplitude of oscillation of the mechanically-forced cantilever is around 1-100 nm. During the approach of the tip to the surface, the cantilever is affected by the presence of the force of Van der Waals [F_{PS} (z)]. For small fluctuations of the cantilever around the position z_0 over the surface, the force can be approximated by

$$F_{PS} = F_{PS}\left(z_0\right) + F_z^{'} \times z\left(t\right) \tag{4.14}$$

where

F'_z is the gradient of the force of interaction tip-surface at the distance z_o.
Then, an oscillation term has to be included into the motion equation

$$m\ddot{z} - k\left(z - U\right) - \gamma\dot{z} + F_0 + F_{PS}\left(z_0\right) + F_z^{'} \times z \tag{4.15}$$

Being

$$z = z_1 + \left[F_0 + F_{PS}\left(z_0\right)\right] / k$$

The eq. 4.15 becomes

$$m\ddot{z} + \gamma\dot{z}_1 + \left(k + F_z^{'}\right) \times z = kU_0 \cos\left(\omega t\right) \tag{4.16}$$

It means that the presence of a gradient of force produces an effective change of rigidity of the system

$$k_{eff} = k - F_z^{'} \tag{4.17}$$

As in par. (4.1), the module of amplitude and the phase in the presence of a gradient force can be obtained

$$A\left(\omega\right) = \frac{U_0\omega_0^2}{\sqrt{\left(\omega_0^2 - \omega^2 - \frac{F_z^{'}}{m}\right) + \omega^2\omega_0^2 / Q}} \tag{4.18}$$

$$\varphi(\omega) = arctg\left[\frac{\omega\omega_0}{\left(\omega_0 - \omega_0^2 - \frac{F_z^{'}}{m}\right)}\right] \quad (4.19)$$

So, the gradient in the force of tip-surface interaction causes a further shift of the curve amplitude and phase. In this case, the frequency becomes

$$\omega_{ris_2}^2 = \omega_0^2\left[1 - \frac{1}{2Q^2} - \frac{F_0^{'}}{k}\right] = \omega_{ris_1}^2 - \frac{F_z^{'}}{m} \quad (4.20)$$

Therefore:

$$\Delta\omega = \omega_{ris_2} - \omega_{ris_1}\left(1 - \sqrt{1 - \frac{F_z^{'}}{m\omega_{ris_1}}}\right) \quad (4.21)$$

or

$$\Delta\omega \approx -\frac{\omega_0}{2k}F_z^{'}$$

Another effect of the presence of the gradient force is the shift of the phase curve in which the inflection point ω′ is shifted to

$$\omega^* = \omega_0\sqrt{1 - \frac{F_z^{'}}{k}} \quad (4.22)$$

and

$$\Delta\omega = \omega^* - \omega_0 = \omega_0\left(1 - \sqrt{1 - \frac{F_z^{'}}{k}}\right) \quad (4.23)$$

About the shift, far from the surface (where F'_z is negligible), a cantilever that oscillates at a frequency ω_o has a phase shift $+\pi/2$ (respect to the bimorph oscillation). Closer to the surface (where $k/QF'_z>1$)

$$\varphi(\omega) = arctg\left[\frac{k}{QF'_z}\right] \approx \frac{\pi}{2} - \frac{QF'_z}{k} \qquad (4.24)$$

Therefore, the phase shift in the presence of a gradient force is

$$\Delta\varphi = \frac{\pi}{2} - \varphi(\omega_0) \cong \frac{QF'_z}{k} \qquad (4.25)$$

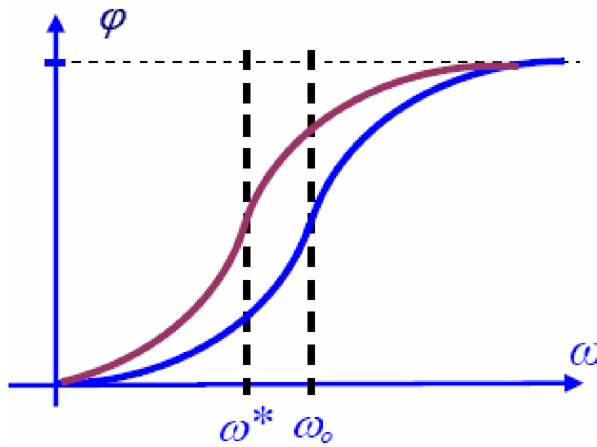

Fig. 4.2. Cantilever phase change in response to a forces gradient

As a result, the phase shift is proportional to the force gradient. This effect is used to obtain the phase-contrast images in AFM.

In order to maximize the amplitude change, the frequency of the bimorph has to be set in the maximum slope area of the magnitude-frequency curve 4.27

The change in oscillation amplitude at frequency ω_A due to the gradient force is correctly approximated by

$$\Delta A = -\left(\frac{2z_{max}Q}{3\sqrt{3}k}\right)F_z^{'} \tag{4.28}$$

Where z_{max} is the maximum amplitude of the oscillation at the frequency resonance

$$\omega_{ris_1} = \omega_0\left(1-\sqrt{1-\frac{1}{2Q^2}}\right) \tag{4.29}$$

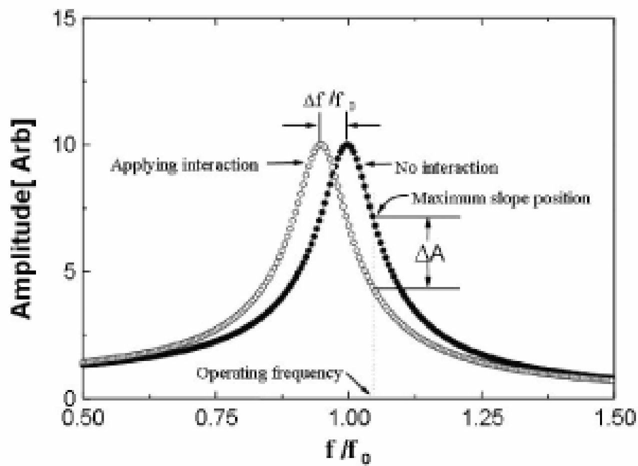

Fig. 4.3. Cantilever resonance curve

The following conclusions can be drawn

1) the external force F_{PS} (considering first and second order terms) produces a modification in the effective stiffness of the oscillator, which results in a change of the resonance frequency and the position of equilibrium around which the oscillation occurs.

2) Oscillations of the system are described the same equation of motion in absence of external force;
3) the change in the resonance frequency, phase and the amplitude of oscillation is proportional to the gradient of external force and are defined by equations 4.21, 4.25 e 4.28 [1,2]

4.1.3 AFM Topography

The AFM topography images in no-contact mode are obtained as follows:

1) the cantilever is made through a mechanically vibrated bimorph whose frequency of oscillation is set slightly above or below the resonant frequency of the cantilever (provided by the manufacturer) to maximize the variation amplitude.

2) the voltage signal provided by the photodiode is sent to a lock-in amplifier that measures the amplitude to the mechanical frequency of bimorph

3) the feedback system moves the scanner, bringing the sample to the tip until the photodiode signal does not reach the reference value.

4) during the scan of sample the oscillation amplitude is kept constant reference value and the voltage control circuit feedback is recorded as AFM image.

In the no-contact area of Figure (1.2) of Chapter 1, when the tip-sample distant decreases, F_z' is positive hence, from equation (4.27) there will be a shift towards lower frequencies of resonance peak and a decline in the amplitude oscillation as it can be seen in figure (4.30).

The AFM image, obtained keeping the cantilever oscillation constant represents a surface in which the gradient force is constant. In absence of electrical and magnetic interactions F_z' is determined by the

Van der Waals force and match, with good approximations, with the surface topography.

4.1.4 EFM images

With the EFM technique described in the previous chapter three, paragraph (3.4) it is possible to obtained information on the electric proprieties of the sample: e.g. the potential and the surface charge distribution.

The EFM signal is overlapped on the signal generated from the mechanical fluctuation of cantilever. The lock-in technique allows to separate the topographical and electrical signal and, simultaneously, measure the oscillation amplitude of the first and second harmonic at frequencies f and 2f where f is the frequency of the AC voltage between tip and sample. This frequency will provide information on surface charges.

The understanding of electrostatic interactions tip-sample represents one of main challenge in the Electrostatic Force Microscopy (EFM). This is because the electrostatic sensors have a complex shape: cantilever with conical or pyramidal tip ending with a spherical apex. Since the techniques of force microscopy are based on detecting the movement of the cantilever, the models focus on the description of the forces acting on tip.

In literature many exemplas can be found that describe the tip-sample system. These models are developed in three ways: a model in layer capacity, a model that uses the method of the images charge and a model that uses a method with finished elements. For the qualitative analysis of phenomenon, the simplest model is that at layer capacity in which the system tip-sample-electrode is considered as capacity.

In the first approximation, the volume under the contact area tip-sample may be regarded as a capacity composed of two layers (fig.4.4).

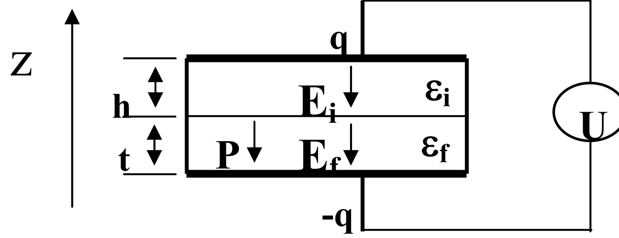

Fig. 4.4. Simplified model of the layer capacity for the EFM signal

The superior layer with thickness h and permittivity ε_i represent the interface between the tip and the sample.
The lower ferroelectric layer, which is the same sample has thickness t, p polarization (independent from the field applied) and permittivity ε_f. For measurements NCEFM the top dielectric is a layer of air, while DCEFM, can be a thin layer of water on the surface.

The electrostatic force acting on the tip can be calculated using the equation:

$$F^{el} = -\frac{\partial}{\partial h}W^{el} = -\frac{\partial}{\partial h}\left(\frac{1}{2}\int_V \bar{E}\cdot\left(\bar{D}\cdot\bar{P}\right)dV - qU\right) \qquad (4.32)$$

where the integral is calculated on entire volume of capacity.

In the electrostatic energy equation, the term **-E·P**/2 represents the energy density due to ferroelectric spontaneous or induced polarization and the term -q·U represents the energy supplied to the system by generating tension. The force can be calculated using the equations:

$$\begin{cases} D = \varepsilon_i E_i = \varepsilon_f E_f + P \\ U = h \cdot E_i + t \cdot E_f \end{cases} \quad (4.33)$$

In the EFM experiment the voltage applied to the tip is:

$U = V_{AC} \cos \omega t$ and V_{DC}=o (4.34)

Since the deflection of cantilever is proportional to the force (Hook law is a good approximation because the oscillation amplitude at frequency V_{AC} is about 1-100 pm) the signal measured by the lock-in is directly proportional at the harmonic components of the force acting on the cantilever. Thinking as in Chapter 3, using the equations 4.32, 4.33 and 4.34 the composition of the force in the three fundamental harmonics is obtained by:

$$\begin{cases} F_o = -\alpha \left[\left(\frac{P}{\varepsilon_f} t \right)^2 + \frac{1}{2} V_{AC}^2 \right] \\ F_\omega = -\alpha \left(\frac{P}{\varepsilon_f} t \right) V_{AC} sen\omega t \\ F_{2\omega} = \frac{1}{4} \alpha V_{AC}^2 sen \left(2\omega t + \frac{\pi}{2} \right) \end{cases} \quad (4.35)$$

the parameter α is given from equation:

$$\alpha = \frac{S}{\left(\frac{t}{\varepsilon_f} + \frac{h}{\varepsilon_i}\right)^2 \varepsilon_i} = -\frac{\partial C}{\partial h} \tag{4.36}$$

in which C represent the equivalent capacity for small signals of the system and s the area of capacitance. Analyzing through a lock-in amplifier, the spectral components of electrostatic force (Eq. 4.35) you can explain qualitatively the influence of ferroelectric domains on EFM signal.

In particular the sign of the first harmonic is determined by the direction of polarization i.e., if for example, the polarization is positive (upward) the amplitude of F_{ω} is negative and the signal will be out of phase of 180°C respect V_{AC}, producing voltage values lower of the value of background.

For negative polarizations (negative surface charges), the signal will be produced in phase with V_{AC} voltage, producing higher voltage values than background. A qualitative typical situation in which the charge distribution of a positively polarized material through application of a negative voltage on the conductive substrate (the tip is a mass) is described, is represented in Fig. (4.5).

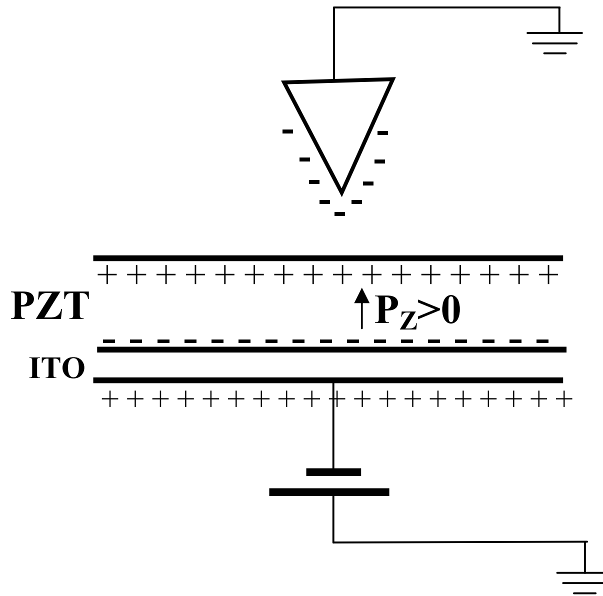

Fig. 4.5. Simplified Scheme of the charge distribution with $P_z>0$.

In the NCEFM and DCEFM modes, the contrast between different domains is due, therefore, to the opposite charge polarization on the surface. The Coulomb force between the tip and these charges lead also a change of the force gradient. Using the conductive tip connected to the ground the surface charges will induce charges with opposite sign on the tip. The Coulomb force is always attractive and identical for antiparallel polarization domains.

On a extended domain the force will decrease slightly to vary the distance tip-sample producing a small gradient of force. On the contrary, near a wall of separation of domains the force will change quick in proximity the antiparallel domains.

The feedback system will keep the value of the gradient of force constant expelling the sample from the tip. In this case the walls of the domains will be represented as a protuberance (reverb). An example of this artefact is shown in fig. (5.19) of Chapter 5 on the sample annealed at 700°C.

In the figure (4.6) and (4.7), on the contrary, is shown the effect of the surface charge distributions on the NCEFM signal. The electric signal (first harmonic) shows a line with a remarkable contrast compared to the background. The topographical image, on the other hand, does not show significant contrasts related to the presence of surface charges distribution in agreement with what just said. However, the persistence in the time of the signal and its recording for threshold values of the potential applied, is necessary for the identification of possible ferroelectric domains. The capacity of the layer model can be improved introducing the contribute of the screening charges on the surface (σ) and the different of the contact potential arising along circuit path. The first harmonic NCEFM signal will be linearly affected also by the latter property. [1, 3-9, 10-18, 19, 20, 21, 22, 23, 24]

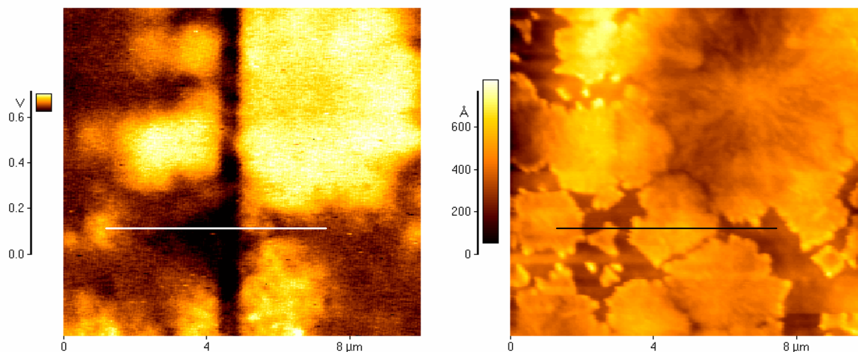

Fig. 4.6.Topographical image (right) and NCEFM image (left) of the sample annealed at 800°C

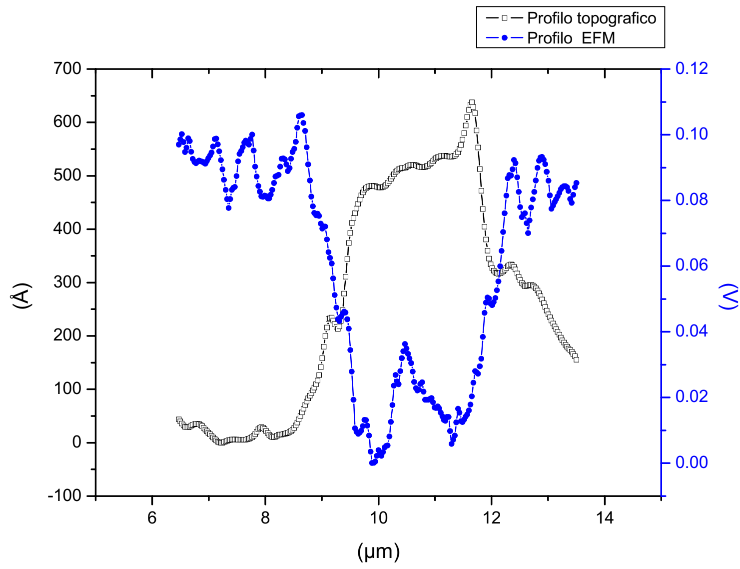

Fig. 4.7. Topographic and EFM profiles.

References

[1] R A Said: J Phys. D: Appl. Phys. 34 L7-L10 (2001).

[2] Daniel Chiang, Philip Zifeng Lei, Fengyan Zhang e Robert Barrowcliff: Nanotechnology 16 S35-S40 (2005).

[3] Sergei V. Kalinin, Dawn A. Bonnell: Physical Review B 65, 125408 (2002).

[4] M. Alexe, C. Harnagea, D. Hesse, U. Gösele : Applied Physics Letters 79, 2 (2001).

[5] N. A. Pertsev, J. Rodr^guez Contreras, V. G. Kukhar, B. Hermanns : Applied Physics Letters 83, 16 (2003).

[6] A. Gruverman, b. J. Rodriguez, R. J. Nemanich, A. I. Kingon: Journal of Applied Physics 92, 5 (2002).

[7] S. Dunn, C. P. shaw, Z. huang, R. W. Whatmore: Institute of Physics Publishing Nanotechnology 13 456-459 (2002).

[8] S. Dunn, R. W. Whatmore: Journal of the European Ceramic Society 22 825-833 (2002).

[9] John F. Hubbard, Helen F. Gleeson, Roger W. Whatmore, Christopher P. Shaw, Qi Zhang: J. Mater. Chem. 9, 375-380 (1999).

[10] J. W. Hong, D. S. Kahng, J. C. Shin, H. J. Kim, Z. G. khim: J. Vac. Sci. Technol: B, 16 (6) (1998).

[11] Genaro Zavala, Janos H. Fendler: Journal of Applied Physics 81 (11) (1997).

[12] X. Q. Chen, H. Yamada, T. horiuchi, K. Matsushire: J. Vac. Sci. Technol. B 17(5) (1999).

[13] A. V. Ankudinov, A. N. Titkov: Physics of the Solid State 47, 6 (2005)

[14] C H. Xu, C. H. Woo, S. Q. Shi: Journal of Applied Physics 95, 12 (2004).

[15] V.V. Shvartsman, N. A. Pertsev, J. M. Herrero, C. Zaldo, A. L. Kholkin: Journal of Applied Physics 97, 104105 (2005).
[16] Seungbum Hong, Jungwon Woo, Hyunjung Shin, Jong Up Jeon, Y. Eugege Pak. Enrico L. Colla, Nava Setter, Eunah Kim, Kwangsoo No: Journal of Applied Physics 89, 2 (2001).
[17] C. Durkan, M. E. Welland, D. P. Chu, P. Migliorato: Physical Review B 60, 23 (1999-I).
[18] S. Dunn: Journal of Applied Physics 94, 9 (2003).
[19] E. D. Missina, N. E. Sherstyuk, K. A. Vorotilov, A. S. Sigov, R. Barberi, M. P. De Santo: Appl. Phys. B 74, 783-788 (2002).
[20] R. Barberi, S. P. Palto, M. P. De Santo, S. G. Yudin. Journal of applied Physics 89, 7 (2001).
[21] V Nagarajan, A Stanishevsky e R Ramesh: Nanotechnology 17 338-343 (2006).
[22] S. W. Jiang, O. Y. Zhang, W. Huang. B. Jiang: Applied Surface Science. (2006).
[23] Jian Shen et al. Appl. Surf. Science (2006).
[24] B. Watts et al. Electroceram, 11-139 (2003).

Chapter 5

Experimental results

$PbZr_{0.53}Ti_{0.47}O_3$ (PZT) thin films were obtained by sol-gel synthesis, deposited by spin coating on ITO-coated float glass and Silicon wafer and subjected to different thermal treatments have been characterized by different techniques. Their thermal structural evolutions have been studied by X-ray diffraction (XRD), scanning electron microscopy (SEM), atomic force microscopy (AFM). The electrical and optical properties have been investigated by using electric force microscopy (EFM). The purpose of this study is to investigate the effects induced by different conductive oxide substrates (ITO and doped Si) on the evolution of micro and nanostructure of PZT films due to the annealing processes.

The growth of ferroelectric perovskite phase, occurring because of the highest annealing temperatures, depends on the substrate, being observed only on ITO substrate, while pyrochlore phase grows on Si substrates. Experiments of electric polarization on nanoscale, through EFM technique, reveal asymmetric responses for induced polarization persistence, which can be related to phenomena of intrinsic polarization regarding the films, which changes as a function of the annealing temperature and of the duration of the annealing processes.

The films were subjected, for one hour and ten hours, to different single thermal treatment in an oven, under ambient atmosphere, in a temperature range between 100°C and 800°C (1

hour) and 100°C at 700°C (10 hours), each one separated by 100°C step, with a ramp rate of 25°C/min. [2-4]

5.1.1 Instruments

XRD measurements have been made using CuK_{α} radiation of a Bruker Axs Reflectometer/Diffractometer (D8) in θ-2θ or asymmetric geometry. Latter geometry has been used to maximize the signal coming from the surfaces and the incident angles range from 0.5 to 1 degrees.

Morphologies have been studied by using a Quanta FEG 400 electronic microscope (Fei, The Netherlands), equipped with heating stage (up to 1000°C), in environmental conditions. PZT layers deposited on ITO/Glass and silicon wafer topographies were obtained by using an AFM instrument (Assing Perception). In order to investigate the electrical properties of PZT layers, the same AFM instrument has been slightly modified to work as Electrostatic Force Microscope (EFM): the remarkable change consists in the substitution of usual tips by $PtIr_5$ -coated silicon tips (Nanosensors, Germany).[1]

Electrostatic force microscopy EFM allows us to obtain information on the surface electrical properties of materials by measuring electric forces between the tip probe and the surface. In this EFM experiment, an electric field is induced inside the PZT thin layer by applying a voltage between a conductive AFM tip in close proximity to the surface and the electronic conductor layer ITO. In the case of thin ferroelectric samples, such an electric field turns out to be very strong localized, and able to produce domains of electric polarization on a sub micrometric scale inside the film. In addition, the evolution of such domains, can be studied by EFM investigations.

By applying a dc voltage between the tip and the ITO layer, it becomes possible to orient domains inside the ferroelectric material. [15]

In this work, such operation will be indicated as a “writing” process. No contact EFM (NC EFM) mode will be used to probe the surface potential. We will refer to this operation as a “reading” process. To read out the surface potential, an electric voltage, between 0.5 and 1.5 Vrms at a frequency f =2 kHz, has been applied between the tip and the ITO layer; such frequency is much lower than the cantilever resonance frequency f=100 kHz. At the same time, *X*-*Y* scans of the corresponding area using the no contact regime of AFM have been done.

A laser beam reflected from the cantilever is detected by a photodiode. The lower-frequency signals of the cantilever oscillation, selected by a lock-in amplifier, are used to create the surface potential images, while those at higher frequency are used, simultaneously, to obtain the topographical images. In addition, another mode that can be used for studying piezoelectric materials is direct contact EFM (DC EFM).

The reading operation, in DC EFM, is performed in contact mode where the external ac voltage induces the piezoelectric vibration of the PZT layer and the collected image is representative of the piezoelectric response of the ferroelectric layer against the charge distribution obtained by EFM investigations. AFM Autoprobe CP, Veeco Instruments, CA has been modified slightly to work as an EFM, equipped with silicon tips covered with a layer of $PtIr_5$ Nanosensors, Germany. An external dc power supply E3630A, Agilent and a lock-in amplifier EG&G Instrument, model 7260 have been used for “writing” and “reading” operations, respectively.

5.1.2 Presentation of experimental dates for the samples annealed at 1 hour

Sample annealed at 100°C

Morphologies were obtained using a Quanta FEG 400 (Fei, The Netherlands) scanning electron microscope. This apparatus can work in

both environmental conditions as well as in high and low vacuum. It enables investigating samples in a variety of environments manipulating temperature, pressure, and humidity. In particular, this microscope is equipped with a software-controlled heating stage, which can be used for heating the sample up to 1000°C.

The sol gel technique used to prepare the film does not allow to control the thickness deposited. An estimate of the thickness of the layer has been possible through the use of SEM.

The SEM technique has been used in order to evaluate the thickness and the structural evolutions induced by the thermal treatments. In Fig. 5.1 a cross-section of the sample annealed at 100°C is shown and the three layers glass/ITO/PZT can be clearly observed. The thickness of the PZT layer is about 290 nm, while the ITO thickness is 100 nm, in agreement with the nominal value declared by the manufacturer. Similar estimations have been obtained also for the others samples.

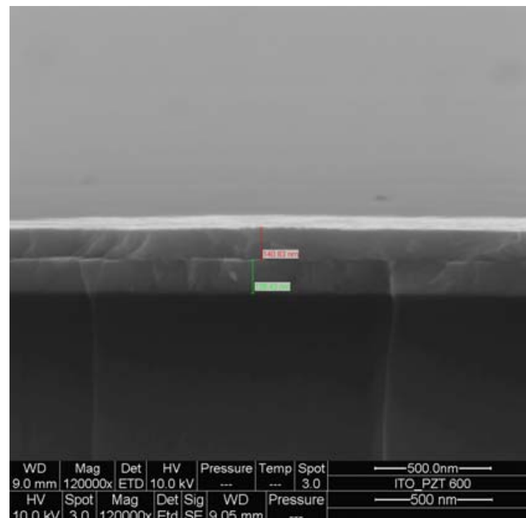

Fig.5.1. SEM lateral view of the thin PZT film deposition on ITO/glass.

Using the microanalysis function of SEM the chemical compositions of the three layers of the sample have been analyzed. Here are the results.

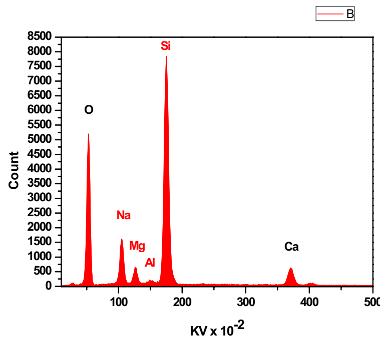

Glass Spectrum

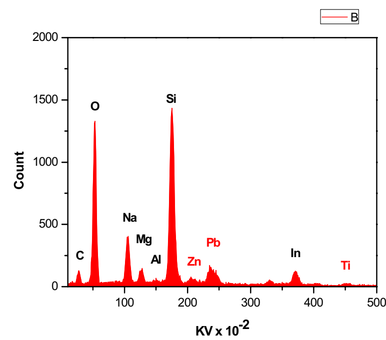

PZT Spectrum

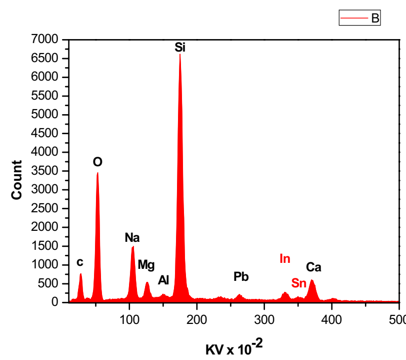

ITO Spectrum

The presence of magnesium and aluminium is due to impurities of the glass, present also in the spectrum of samples of glass only. The interpretation of EFM images, in contact and no contact mode, are controversial enough for the overlap of both electromechanical and electrostatic charge of the electric image contrast.

In Figs. 5.2 and 5.3 the topography, given by AFM, of a region where a line was "written" by a constant voltage, for a sample annealed at 100°C for 1h are shown. In fig. 5.2, on the left, the corresponding EFM image, related to a line previously "written" applying -10V, is shown, while in fig 5.3, on the left, the EFM image, related to a line previously "written" applying +10V, is shown.

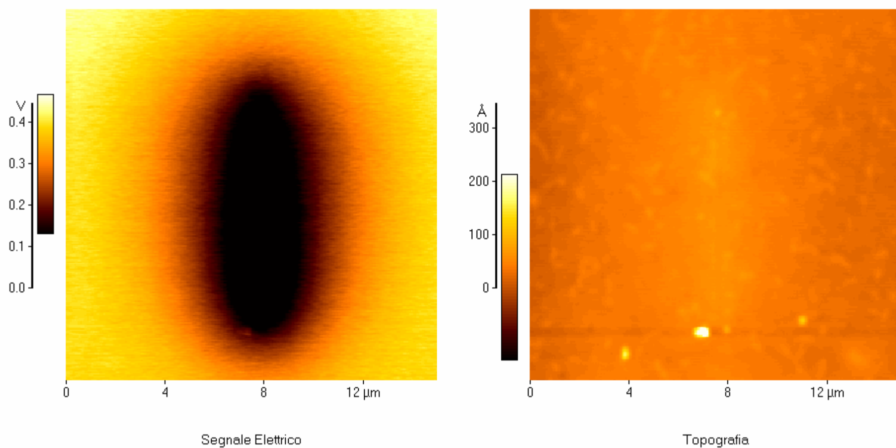

Fig.5.2. NC EFM image (left) and topographic image (right) of the PZT surface annealed at 100°C.

During the application of the voltage in contact mode, an additional pressure, due to the electrostatic forces between the tip and the surface sample, is applied on the sample. It can induce a small amount of damage on the surface, as is evident from the topographical images in fig. 5.2 and 5.3

On topographies are present, as evidenced by the microanalysis performed with the SEM, the white grains that appear in the PZT image, accumulated during the deposition.

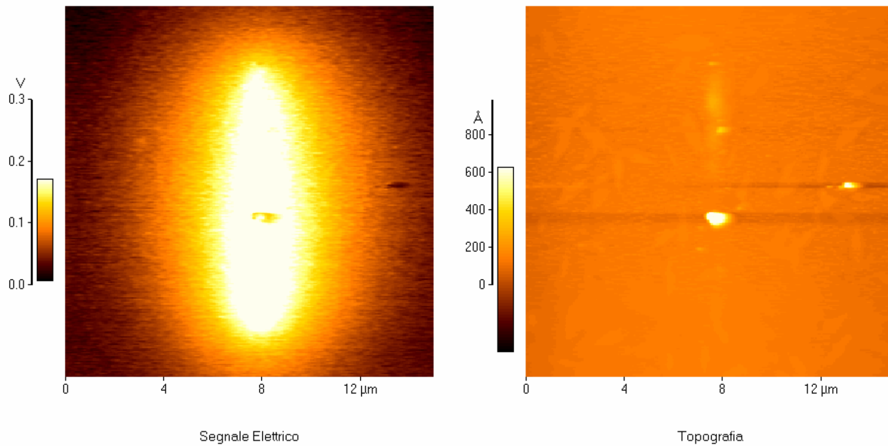

Fig.5.3. NC EFM Image (left) and topographic image (right) of the PZT surface. The line was written applying +15V on the sample.

Black and white spots on the electric maps are related to the charge distributions on the surface, due to the applied dc voltage, in a corona-like discharge effect.

Following the time evolution of the electrical traces, it can be observed that the dimensions spot of the accumulated charges decreases in time, due to the ohmic diffusion of charges on the surface.

After 15 min, the white spot vanishes completely, while the black one is still detectable, revealing an asymmetrical behaviour of the electric charge persistence on the surface, on the contrary on the topography no changes are observed.

The PZT materials are enough "hard" and unable to resist the pressure from the tip in contact with the surface without deformation, however, during the writing process it is possible to damage the surface of the sample.

Samples annealed at 200°C, 300°C and 400°C

Results quite similar to those of the 100°C annealed samples have been obtained for samples annealed at 200°C, 300°C, 400°C, and 500°C. Below, the topography images and EFM signals, on samples tempered at 200°C, 300°C and 400°C with either polarity applied are shown. The electrical signals have been acquired immediately after writing and at different times. Figure 5.4 shows the time evolution of the lines "written" on the sample tempered at 200°C with opposite polarity +10V and -10V.

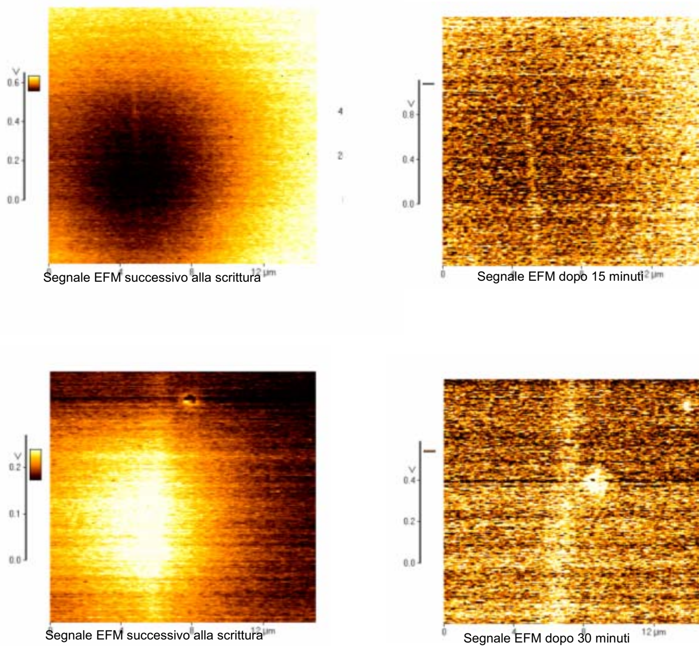

Fig.5.4. NC EFM Image (left upper) and time evolution of the line (right upper) after 15 minutes. NC EFM image (left button) and time evolution of the line (right button) after 30 minutes. The lines have been written applying -10V (black line) and +10V (white line) on the sample annealed at 200°C.

Continuing the discussion it should be noted that on the previous image (fig.5.4) the phase of the lock-in was not properly fixed, this

implies a reversal contrast for the lines written with the same dc voltage. Below (Fig. 5.5 and 5.6) the time evolution of the lines "written" on the samples annealed at 300°C and 400°C.

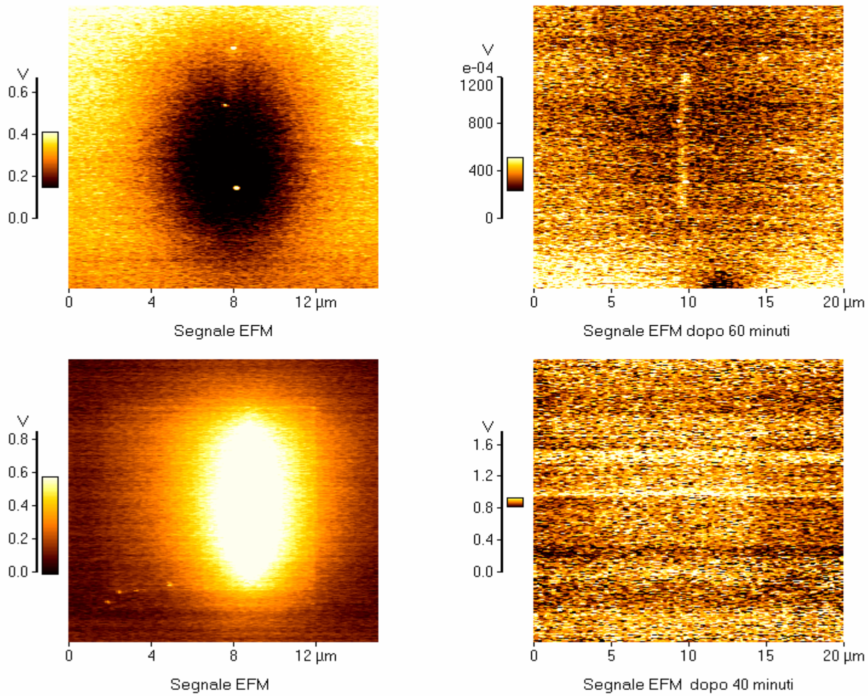

Fig.5.5. NC EFM Image (left upper) and time evolution of the line (right upper) after 60 minutes. NC EFM image (left button) and time evolution of the line after 40 minutes. The lines have been written applying -15V (black line) and +15V (white line) on the sample annealed at 300°C.

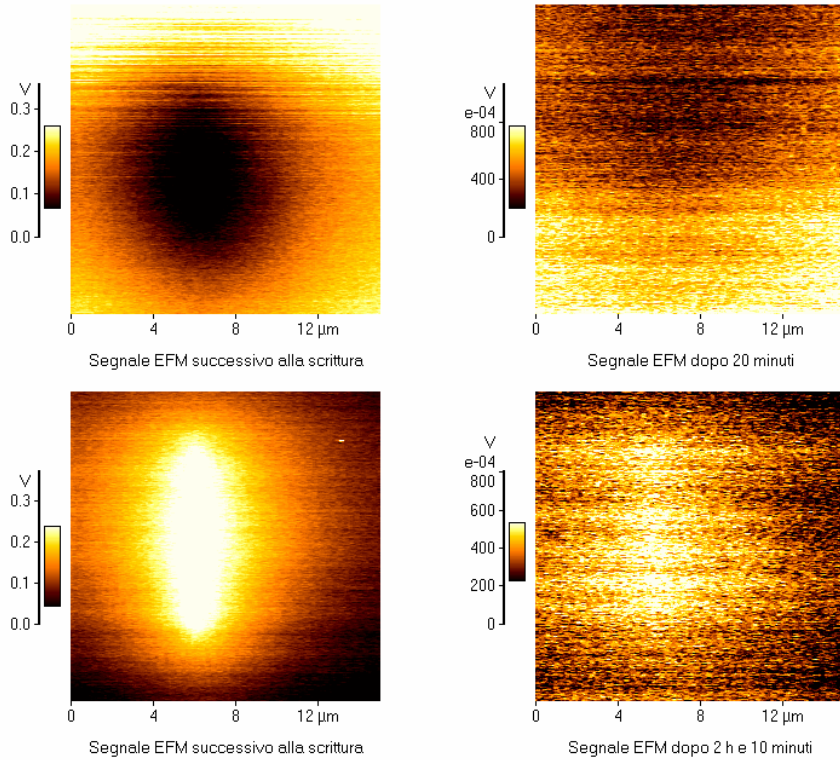

Fig.5.6. NC EFM Image (left upper) and time evolution of the line (upper right) after 20 minutes. NC EFM image (left button and time evolution of the line (right button) after 40 minutes. The lines have been written applying -15V (black line) and +150V (white line) on the sample annealed at 400°C.

From this moment and throughout the rest of the treatment the phase of the lock-in has been set in order to acquire correctly all images. We divided the series of eight samples in two groups. The first group, including the samples annealed from 100°C to 500°C as has been amply documented, do not show ferroelectric properties because the temperature is below the phase transition. The second group includes the samples

annealed at a temperature greater than that of phase transition (from 500°C to 800°C).

Sample annealed at 500°C

Before discussing the EFM images of the others samples the topographic images obtained with SEM on the sample annealed at 500°C will be shown.

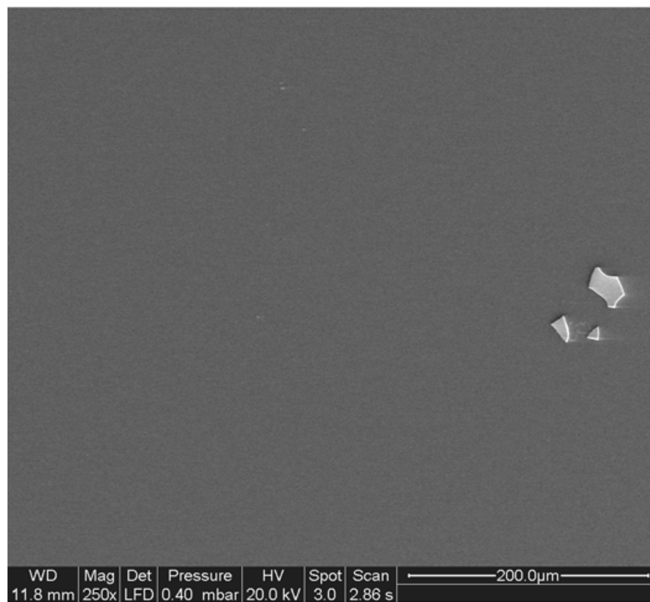

Fig.5.7. SEM topography image of the sample annealed at 500°C.

Fig. 5.7 shows a portion of the surface where accumulations of PZT have been identified and of which we give a magnification (Fig. 5.8).

.

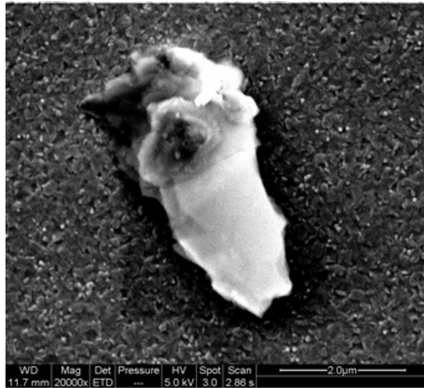

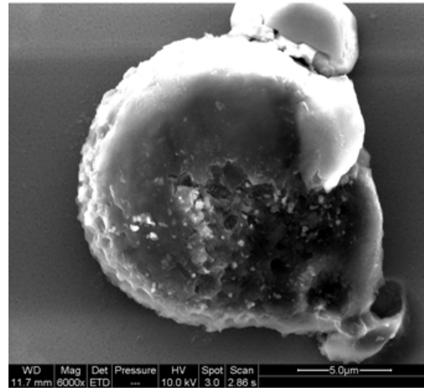

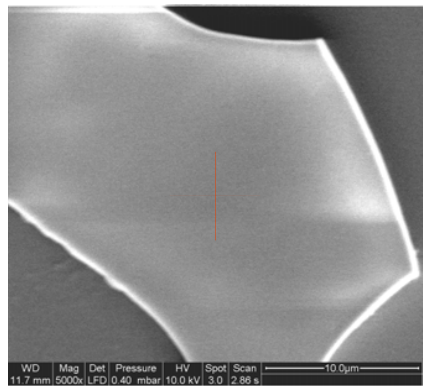

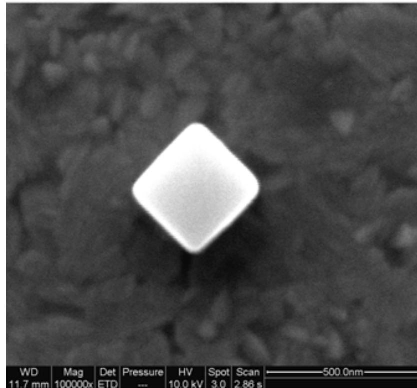

Fig.5.8. PZT details on the surface annealed at 500°C.

On these particulars, found on the surface, a SEM microanalysis to verify the chemical composition was performed. Here is a spectrum run at the point marked with a red cross. (Fig.5.9).

.

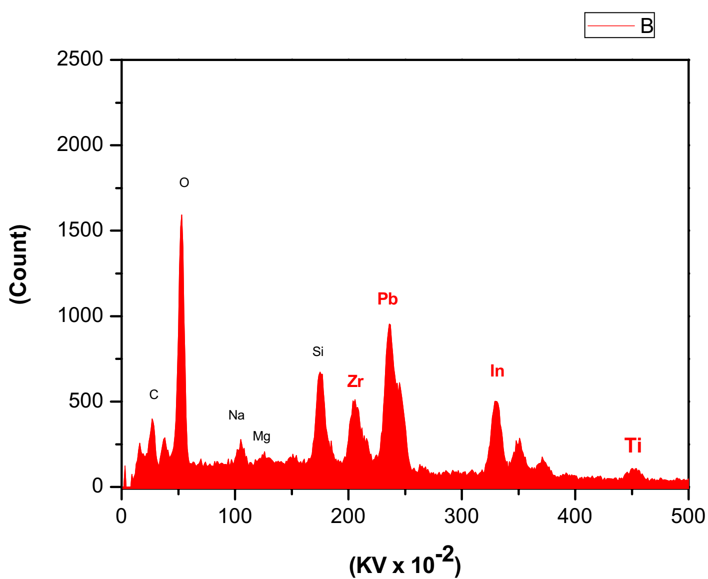

Fig. 5.9 SEM microanalysis performed on the sample annealed at 500°C.

By microanalysis performed also on others details from that shown no appreciable difference have been found. The same sample annealed at 500°C we applied a dc voltage and followed the behaviour of the charge accumulated over time.

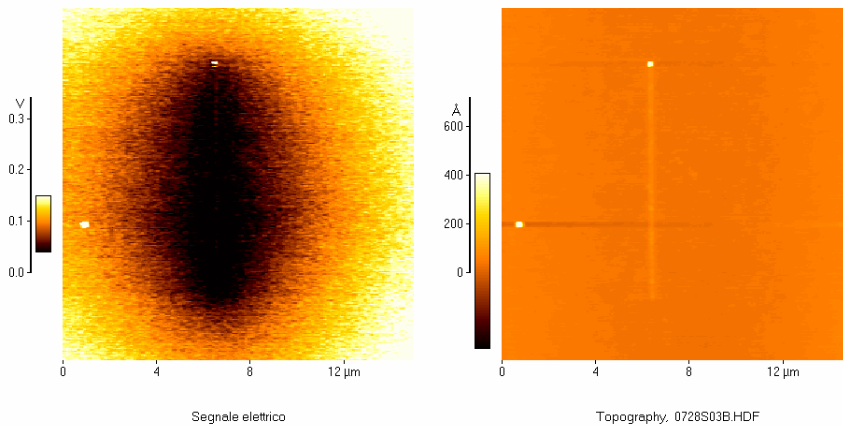

Fig.5.10. NC EFM Image (left) and topographic image (right) of the PZT surface annealed at 500°C. The line was been written applying -15V on the sample.

Once again, the left image refers to the electrical signal while the right image is the topography. We have analyzed the possibility of writing a line by applying a voltage of -15V on the sample. Initially we followed the time evolution of the line. The result is shown in Figure 5.11.

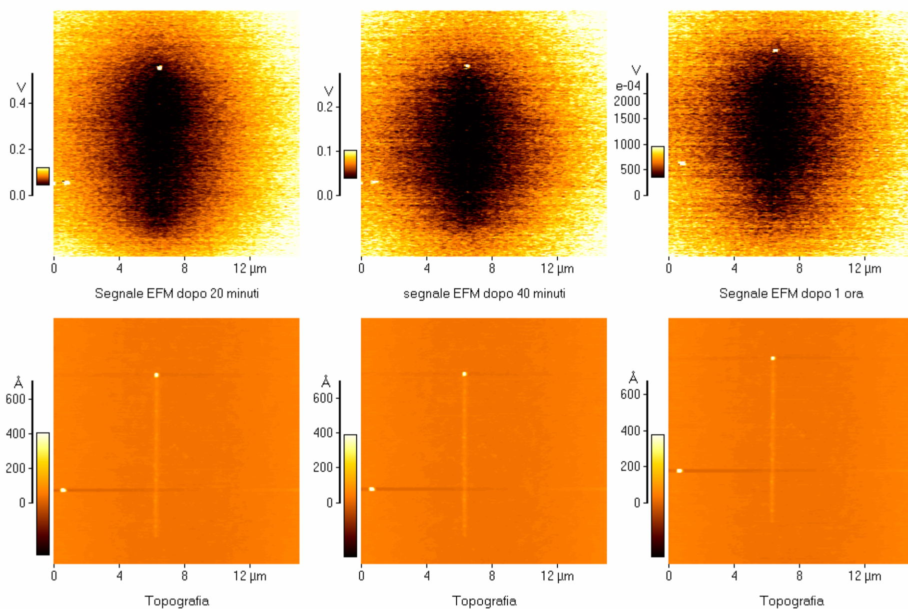

Fig.5.11. Time evolution of the line written applying -15V on the sample. The lines have been acquired after 20 min, 40 minute and 60 min. Topographic image (on the button).

Then we applied a voltage +15V on the sample, the result is shown in Figure 5.12, 5.13.

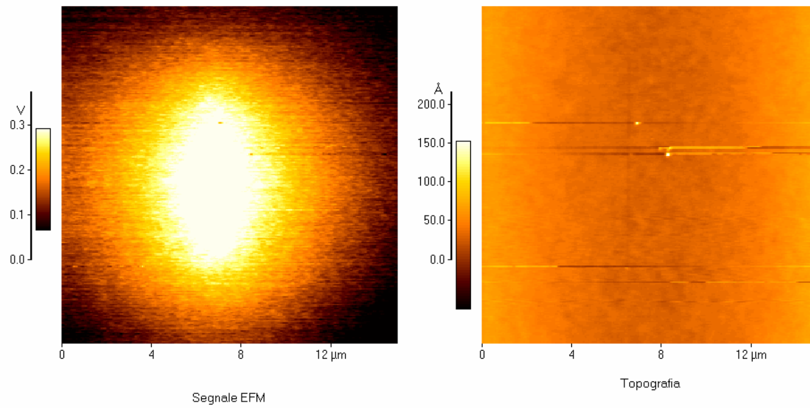

Fig.5.12. NC EFM Image (left) and topographic image (right) of the PZT surface annealed at 500°C. The line was been written applying -15V on the sample.

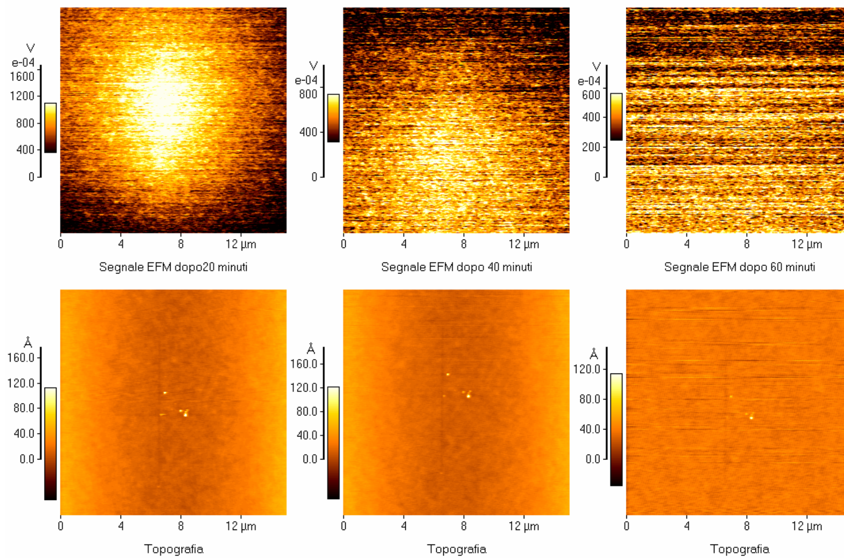

Fig.5.13 Time evolution of a line written with +15V on the sample. The images have been acquired after 20 min, 40 min and 60 min.
DC EFM signal upper and corresponding topographic image bottom.

The PZT film deposited by spin coating are locally polarized by applying an electric field.

To write more lines, the tip is moved to different points of the sample surface by applying alternating positive and negative voltages. In samples annealed from 100°C to 500°C this was not possible because the charge deposited was enough diffused and did not allow the writing of more than one line.

Samples annealed at 600°C e 700°C

A different behaviour has been observed, on the contrary, for the samples annealed at 600°C, 700°C, and 800°C.

Interesting results on the morphological evolutions and kinetics phase transformation of the PZT layers are provided by *in situ* investigations. In fact, the experimental procedure of the annealing processes, reproduced inside the SEM instrument, indicates that after annealing at 600°C, the PZT layer shows on the surface the presence of different flower shaped dendritic structures, called “rosetta,” as shown in fig. 2.6 chapter 2. The sizes of such structures range from hundreds to thousands of nanometers, increasing for higher-temperature treatments. Calorimetric measurements performed on such samples have shown an exothermic peak at temperatures slightly higher than 600°C, which has been assigned to the phase transition from amorphous to crystalline phases.[10,16].

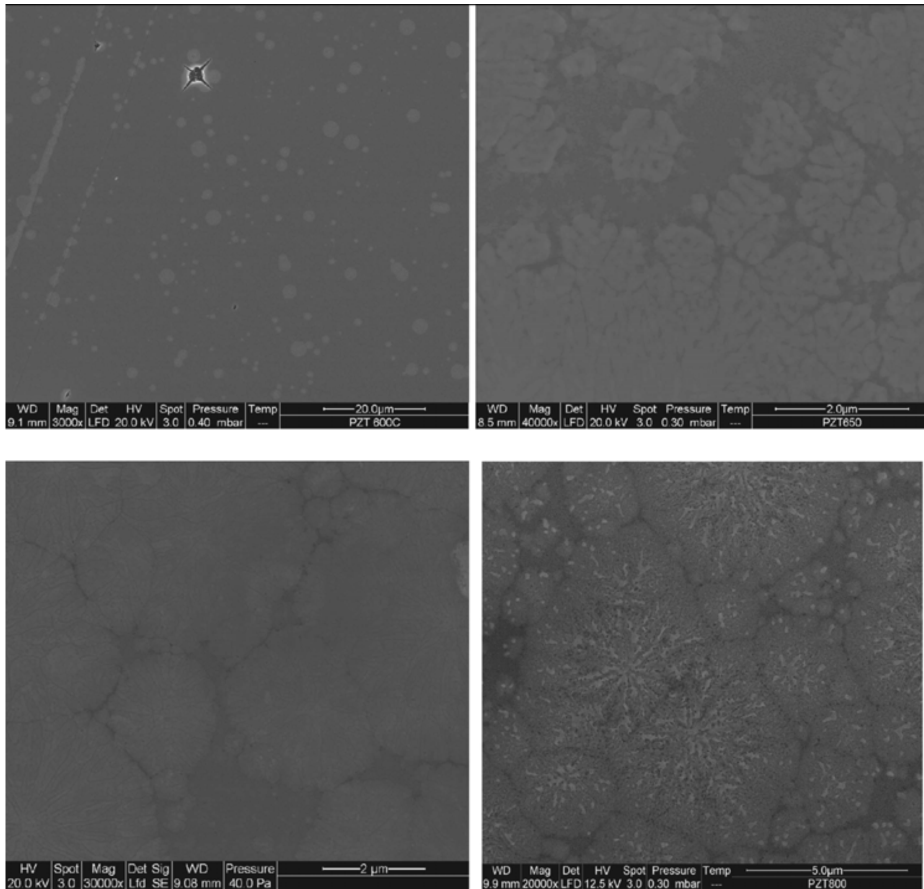

FIG.5.14. SEM images showing various steps of the in situ phase transition of a PZT film deposited on ITO substrate:

In Figs. 5.16, 5.19, 5.22 the AFM topographies of the samples annealed at 600°C, 700°C and 800°C are shown. As previously shown by SEM characterizations, an abrupt change of topography occurs when the samples are heated above 600°C, changing from a granular structure to the nucleation of the “rosetta” structures, with higher dimensions for higher annealing temperatures. These structures can be reasonably related to well-crystallized domains, whose expansion is favoured by the high temperatures.

In Fig.5.15 EFM images related to the electric traces writing applying -10V by collected on samples annealed at 600°C are shown.

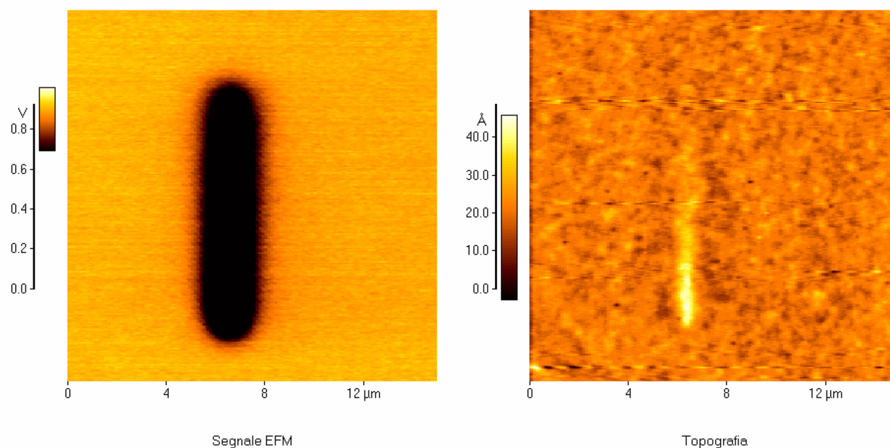

Fig.5.15 NC EFM Image (left) and topographic image (right) of the sample annealed at 600°C. The line was been written applying -10V voltage on the sample.

In fig. 5.16 the time evolution of the electrical trace writing on the sample annealed at 600°C was reported, it can be observed that the spot dimensions for the black line after about 2 hours is still well detectable.

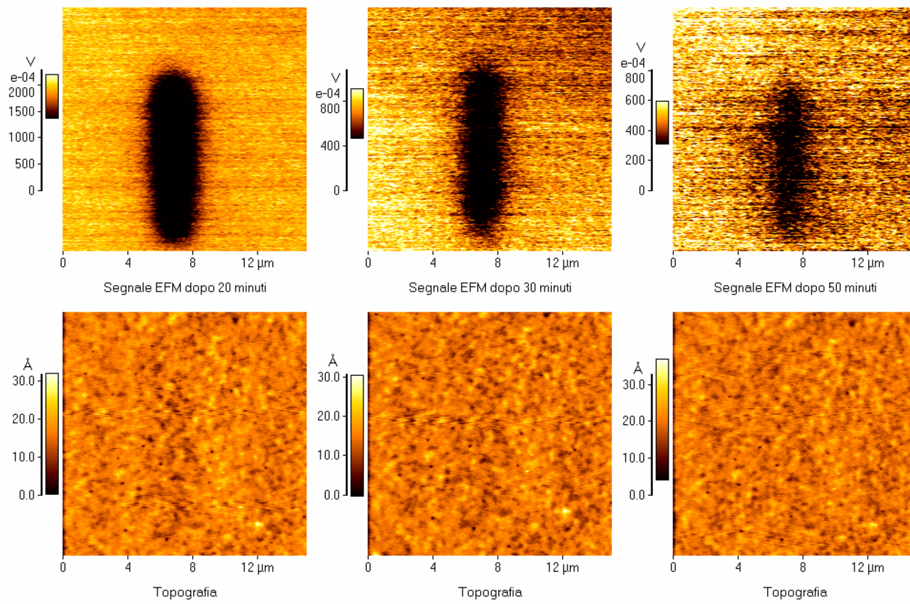

Fig.5.16 Time evolution of a line written with -10V on the sample. The images have been acquired after 20 min of the first scanning, 30 min from the second and 50 min from the third.

In the next image, on the contrary, on the same sample has been applied an opposite voltage (+10V) and we report the time evolution of such signal (fig. 5.17).

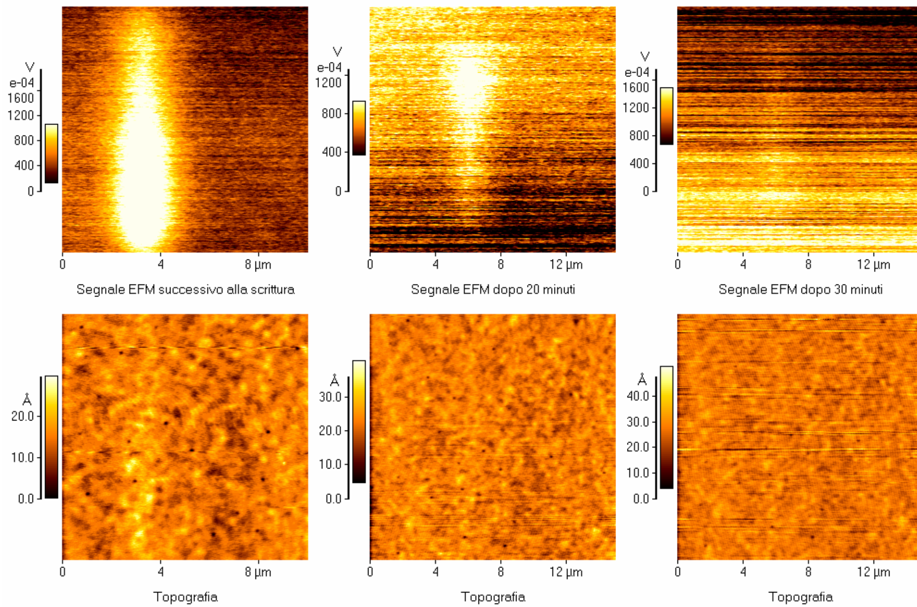

Fig.5.17 Time evolution of a line written with +10V on the sample. The line has been written after 20 min and 30 minutes. DC EFM signal upper and corresponding topographic image bottom.

The black spots of the samples annealed at 600°C are better defined than those observed on the samples annealed at lower temperatures. Moreover, they are still detectable after 2h. This could be related to the alignment of the dipoles inside the PZT layer that traps the charges deposited on the surface by the corona effect. On the other hand, the lifetime of the white line is still shorter than that of the black one and disappears after 30 min.

On the sample annealed at 700°C, a rearrangement of the granular structure in clusters of micrometric size can be observed (see Fig.5.18 topography).

The EFM image shows how the definition of the electric trace "written" applying −10V is still improved and much more intense. It has been supposed that in these samples, the transition from the paraelectric to the ferroelectric phases occurred. Such evolution is even more evident in the EFM image related to the samples annealed at 800°C, as shown in Fig. 5.21.

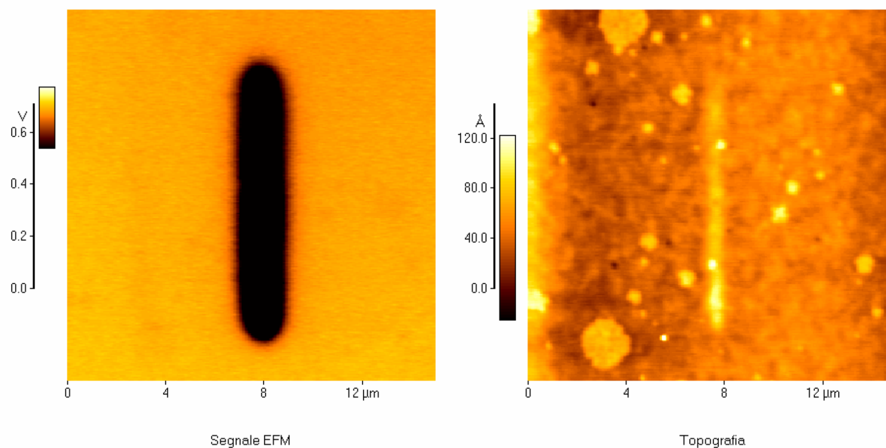

Fig.5.18 NC EFM Image (left) and topographic image (right) of the PZT surface annealed at 700°C. The line was been written applying -10V on the sample.

The topographic images (right) shows a white line "reverb" which represents the influence of charge surface, produced in the process of "writing", on the topographic signal.

This means that there is the presence of charges of the same sign on the tip as the sample (probably due to processes of discharge tip-sample) which determine an increase of the keff (eq. 4.17) and of the

resonance frequency. This implies an increase in the oscillation amplitude that the feedback system compensates by lowering the sample interpreting the excess charge as a surface protuberance. After few minutes of the first scanning the reverb disappears completely as shown by the images of the EFM signal repeated several times after certain time intervals (Figure 5.19)

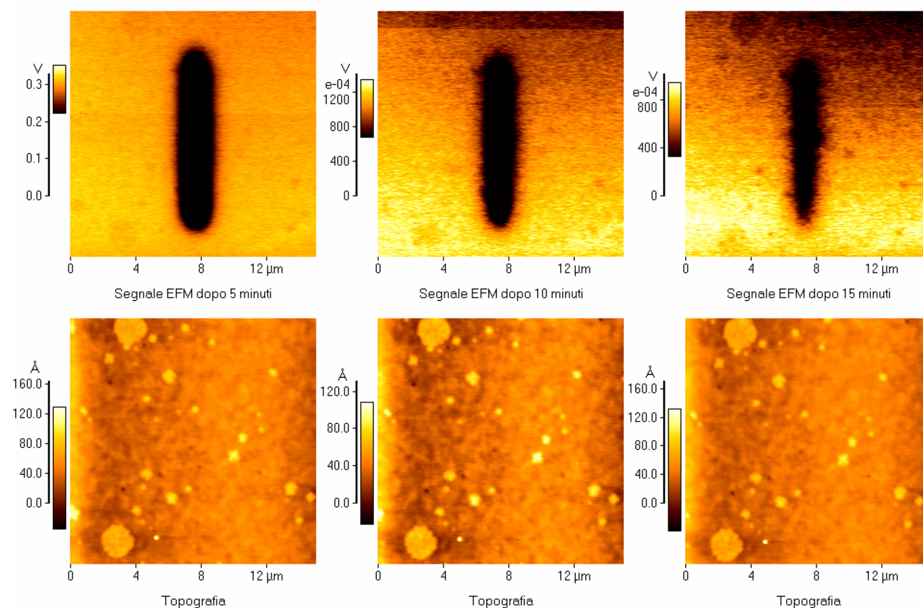

Fig.5.19. Time evolution of a line written with -10V on the sample annealed at 700°C. The images have been acquired after 5 minute from the first scanning 10, 15, 20, 30, and 50 minute.

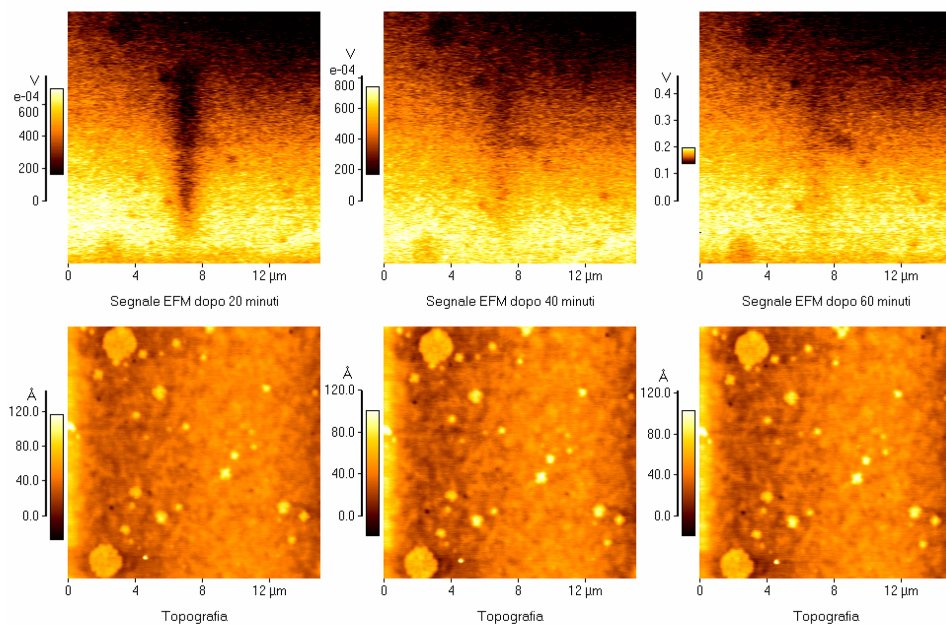

Fig.5.19 continued.

On the same sample a voltage with opposite polarity +10V was applied. The next images show the temporal evolution of the electric track (fig. 5.20).

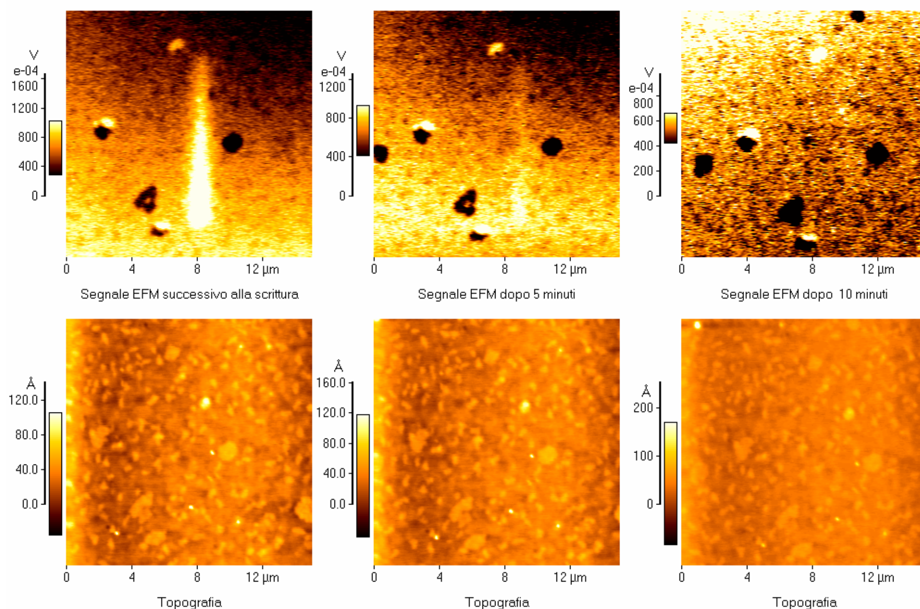

Fig.5.20. Time evolution of a line written with +10V applied on the sample. The images have been acquired one after the writing, the others 5 minute from the first scanning and after 10 minute from the second.

Sample annealed at 800°C

In the EFM images Fig. 5.21, two lines are visible, "written" by the two opposite voltages (-20V black, +20V white).

This increased sharpness could be explained taking into account a stronger dipole reorientation inside the ferroelectric layer. Such lines are still detectable after about 2h.

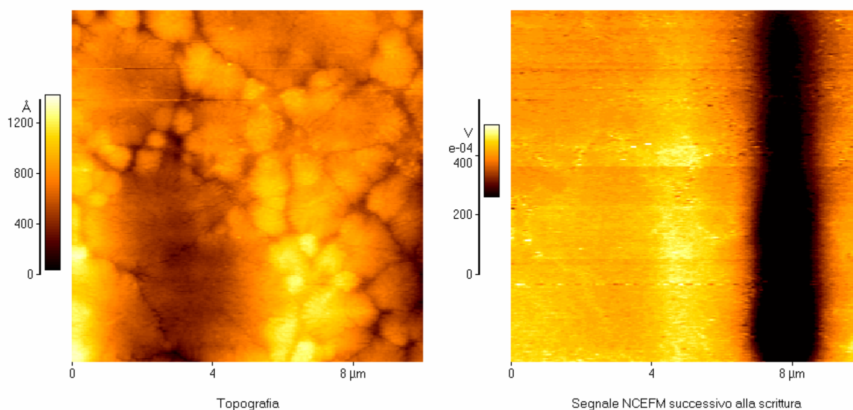

Fig.5.21. NC EFM Image (right) and topographic image (left) of the PZT surface annealed at 800°C. The lines have been written applying -20V (black line) and +20V (white line) on the sample.

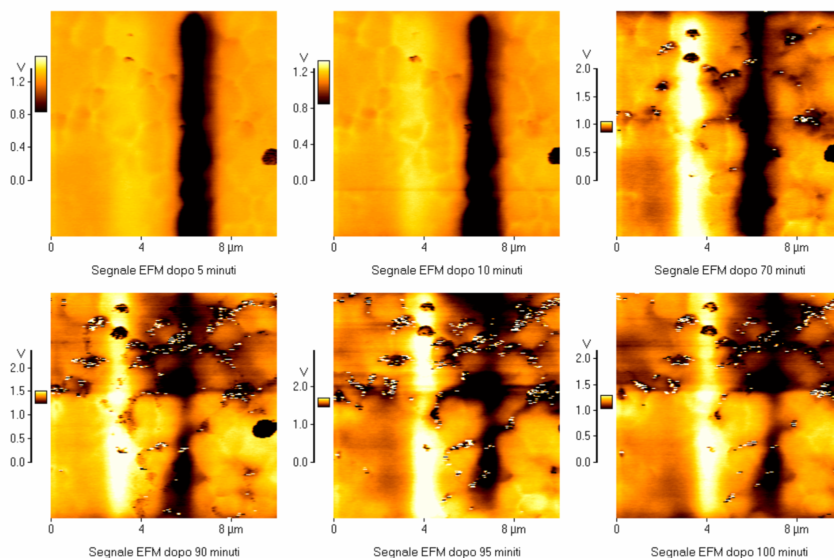

Fig.5.22. Time evolution of the lines written with +20 and -20 voltage applied on the sample. The images have been acquired for 5 minute from the first, 10, 70, 90, 95 and 100 minute from the previous.

The presence of small black spots on the EFM images, absent in the topographical image, are probably of the charge attracted by the tip during the process of "reading".

In all the images shown we observe a charge deposition on the surface. There are only two mechanisms that may be responsible for the electrical properties of the surface (electrostatic effect and electromechanical or piezoelectric effect). In the first case, during the writing process may happen that the tip deposits charge on the surface of the material, dielectric or ferroelectric.

In the case of a ferroelectric, the charge can be deposited for voltages lower than the threshold of the reversal polarization, this decade also rather quickly, sometimes within a few tens of seconds.

This behaviour is characteristic of the samples annealed from 100°C to 500°C, in which the dielectric nature of the sample through the free charges surface dominates.

The samples annealed at 600°C, 700°C and 800°C, where the phase transition probably occurred, the ferroelectric nature of the material through the charge polarization dominated.

The images on samples annealed at higher temperature show clearly that not only the morphology of the surface is changed with the formation of rosettes, ranging from a few nanometers to a few microns (Fig. 5.19 and 5.21), but the charge deposited during the writing process persists for several hours.

Furthermore, the possibility of writing more or less defined lines depends strongly on the size of rosettes. So we have investigated only the electrostatic effect.

It is also possible to measure qualitatively the piezoelectric response of the sample even if the process requires more accuracy for the possible deterioration of the tip due to contact with the surface (Fig. 5.23).

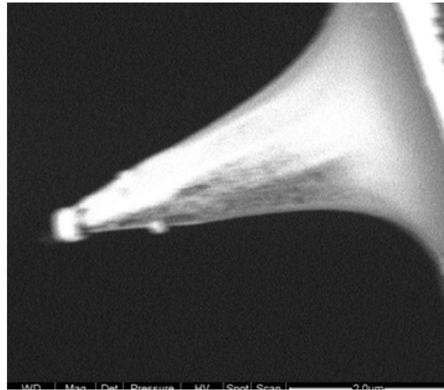

Fig.5.23. SEM image performed on a tip after being used in the "writing" process

Below is reported a SEM topographical image of the sample annealed at 800°C. On the surface of the film we can clearly distinguish two different areas, some of darker colour that represent the surface of PZT still in an amorphous phase and the lighter colour rosettes due not to thermal stress, but to the nucleation of the material.

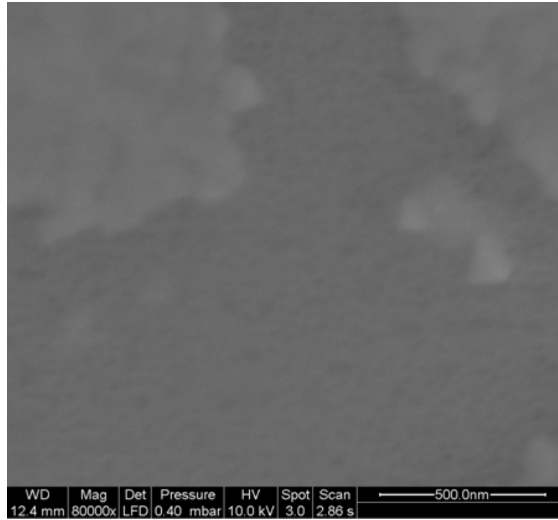

Fig.5.24. SEM image of the sample annealed at 800°C.

The SEM microanalysis performed on both of these areas shows clearly the chemical composition of the elements constituting the material. The spectrum below was performed on the amorphous area of PZT and shows that no significant differences were running on rosettes.

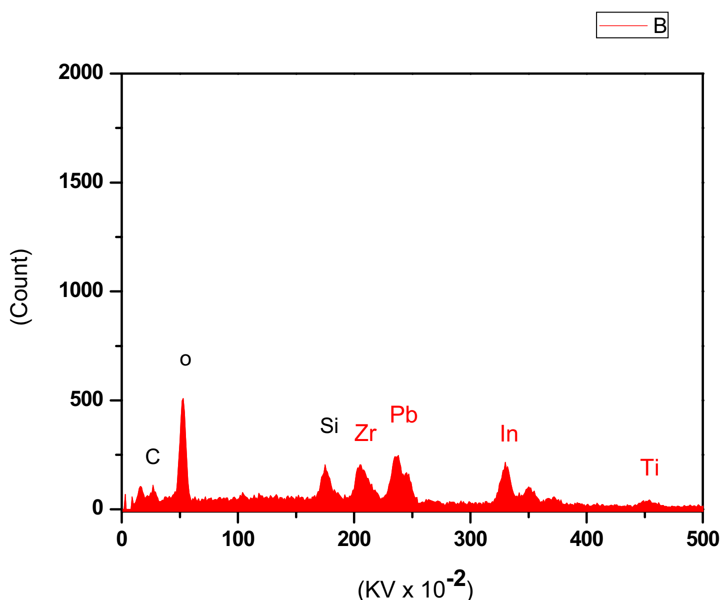

Fig. 5.25 Spectral analysis in a point on the surface inner the fracture of the sample annealed at 800°C.

5.1.3 DC-EFM and NC-EFM images on the sample annealed at 800°C

The analysis of contact and no contact EFM images requires particular attention (paragraph 5.2) for the overlap of the electrostatic and piezoelectric effects.

The interpretation is purely qualitative and is related to the context in which all the images have been acquired.

Contact and no contact images have been obtained with the same tip and with a lever of the same nominal elastic constant.

In fig. 5.26 a three-dimensional image of the surface of the sample annealed at 800°C is represented. On this same area we have performed scanning measures in EFM contact.

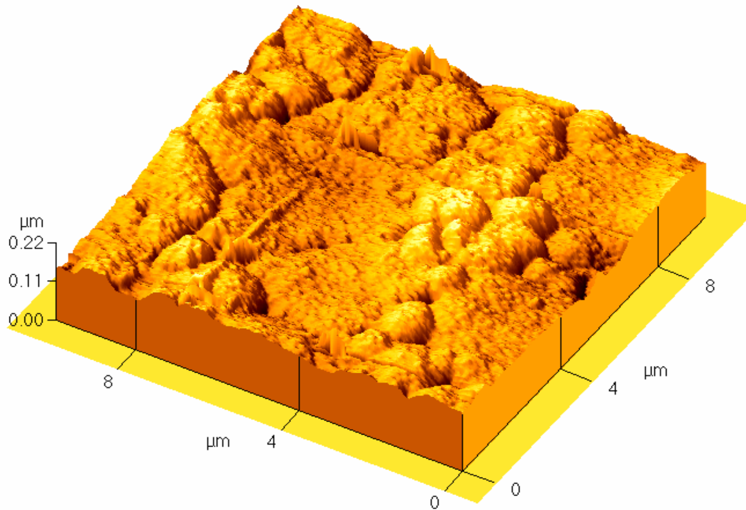

Fig. 5.26 AFM Three-dimensional image of the PZT surface annealed at 800°C.

On the samples annealed at the highest temperature, contact EFM has been performed to check the piezoelectric response of the PZT layer. When using contact mode, the "writing" operation requires higher dc voltages: in order to obtain detectable lines, 20V were applied. The EFM images show high intensities fig. 5.27 and they have been related to the piezoelectric effect of the PZT layer. Even in contact mode, the higher intensity of the electric signal is confirmed related to the black line with respect to that of the white line, as can be seen in Fig. 5.27.

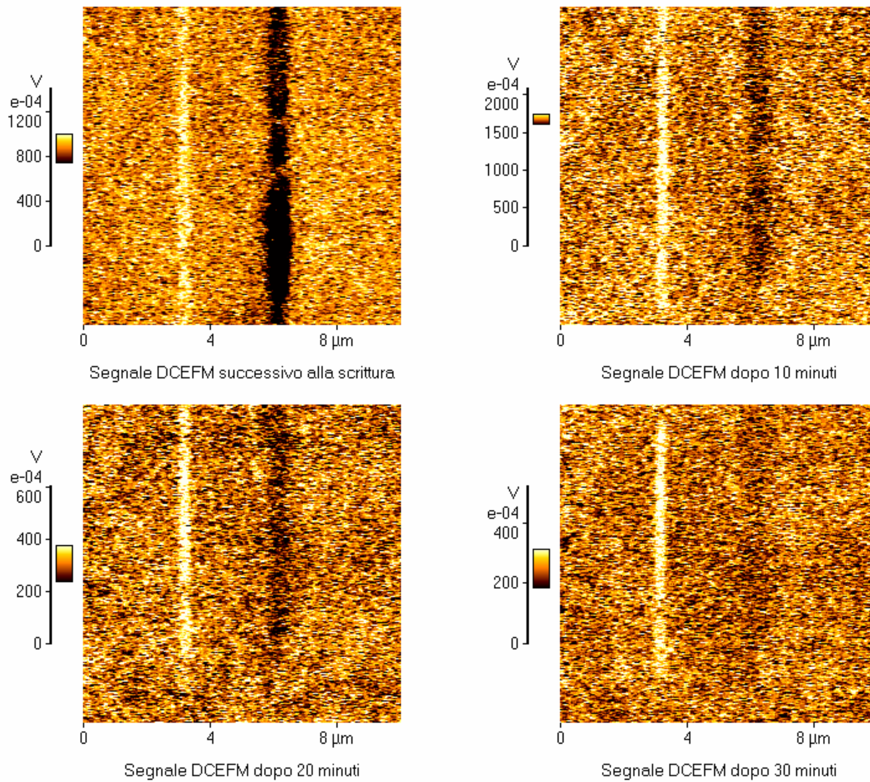

Fig.5.27. Direct contact EFM image of the PZT sample annealed at 800°C, lines written at ±20V (white: +20V, black: 20 V).

NCEFM images show the signal coming from the charge deposited by the tip, while the image acquired in DCEFM provides a map of the piezoelectric response of the material. The DCEFM image is "read" by applying a small AC field between tip and sample, by stimulating the piezoelectric vibration of the surface. Below is the linear profile of the two electric tracks "written" and "read" in DCEFM mode of the 5:28 where the increased in the time and the increased of the depth of the charge deposited with a negative voltage is indicative of the asymmetric response of our samples.

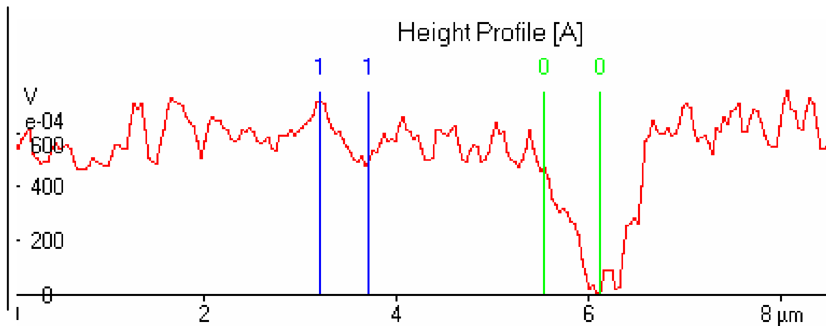

Fig.5.28 Linear profile of the two electric traces of the fig. 5.29

- Depth of the line written with negative polarity: 4.58×10^{-02}V
- Depth of the line written with positive polarity: 2.17×10^{-02}V

DCEFM measures were also performed on the sample annealed at 700 °C but no electric trace was found, this could suggest that the sample annealed at 800 ° C shows a piezoelectric behaviour.

In this regard we report in the next paragraph a macroscopic cycle of the hysteresis performed on the sample annealed at 800°C compared with a PZT known.

5.1.4 Macroscopic hysteresis cycles

The ferroelectric hysteresis curve is instrumental to observe the ferroelectric properties of a ferroelectric sandwiched between two electrodes.

Polarization switching can be observed in a ferroelectric hysteresis loop when measured by using a Sawyer-Tower circuit, Sawyer and Tower [1930]. The polarization is measured by the change in current when applying an AC voltage, at a small frequency, that is varied from 0V to

voltages greater than the coercive field of the ferroelectric being measured.

This circuit consists of a voltage generator, an oscilloscope, resistance and reference capacity. Fig 5.29 shows the simplified diagram of the circuit-Saywer Tower

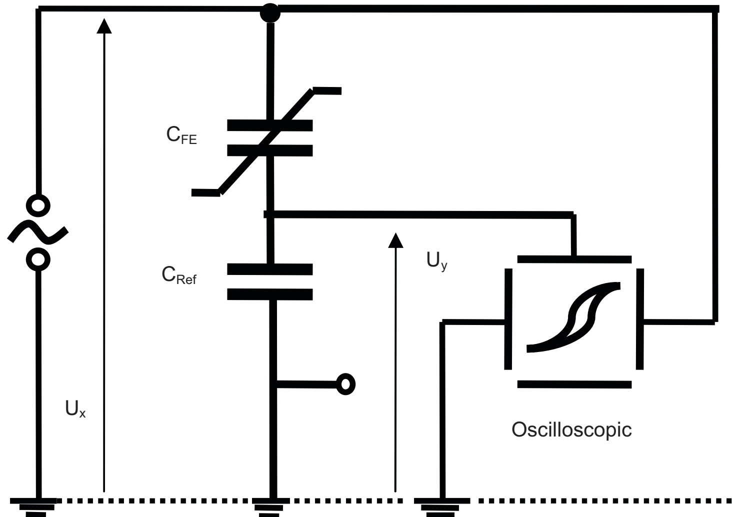

Fig.5.29. Saywer-Tower Circuit.

A ferroelectric material shows a polarization hysteresis in response to an applied electric field. The polarization P occurs through charges + Q and -Q on both sides of the area A of the ferroelectric capacitor C_{FE} with:

$$P = \frac{Q}{A}$$

This charge can be measured through a second capacity C_{Ref}, in series to C_{FE}, which acts as a charge-voltage converter. U_y tension to the end of C_{Ref} is:

$$U_y = \frac{Q}{C_{Ref}} \Rightarrow Q = U_y C_{Ref}$$

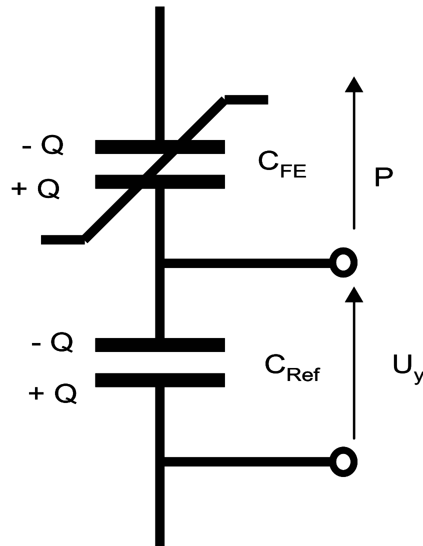

Fig.5.30. Polarization measurement with a reference capacity.

The polarization of the sample is:

$$P = \frac{C_{Ref} U_y}{A}$$

In the case of ferroelectric the surface charge is produced by the polarization P induced by applying an external potential U_x.

The hysteresis loop can be obtained by connecting U_x to a generator voltage in the X entry and U_y in the Y entry at the same oscilloscope.

Below is a hysteresis loop performed on the sample annealed at 800°C where the values of the components used in circuit-Saywer Tower are: C_{Ref}= 47 nF, f= 1kHz e U_x=20V_{pp} (fig. 5.31).

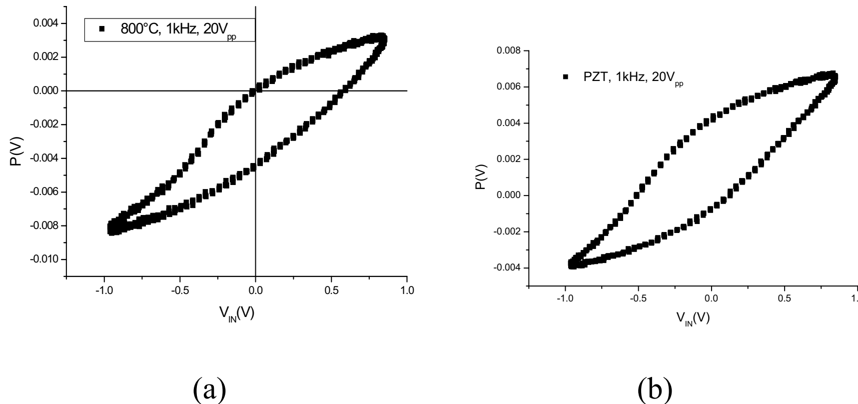

(a) (b)

Fig.5.31. Ferroelectric Hysteresis cycles performed on a PZT known (b) and a PZT prepared in our laboratories and annealed at 800°C (a).

The macroscopic hysteresis loop of our sample shows an asymmetric behaviour with respect to the two polarizations.

In particular, you may notice a shift of voltage (imprint) towards the negative probably due to a preference of the polarization-induced negative voltage signal also confirmed by NCEFM signal.

The phenomenon of the imprint is due to an asymmetry in the distribution of trapped charges, such as electrons and oxygen vacation [51,52].

Figure 5.32 shows the photograph of the circuit built in our laboratories.

Fig.5.32. Picture of the circuit and electronics used to measure the macroscopic hysteresis loop.

5.1.5 Presentation of experimental dates for the samples annealed at 10 hours.

XRD structural characterization

X-ray diffraction (XRD) investigations have been performed on PZT layers subjected at different annealing processes temperatures in the range between 100°C and 700°C. The meaningful results, at 500°C and 700°C obtained from the PZT layers deposited on ITO and doped Si substrates are shown in Figs. 5.33 and 5.34, respectively.

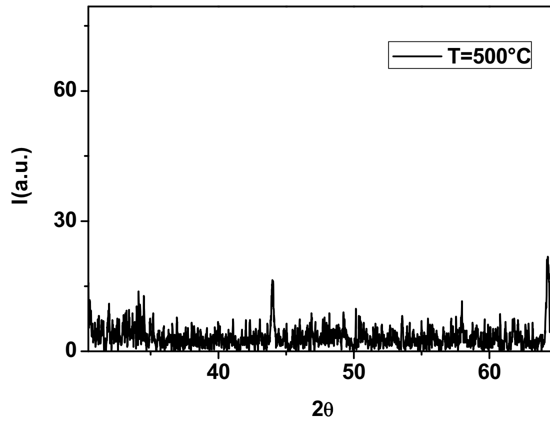

Fig.5.33. XRD patterns for PZT/ITO/glass samples annealed at 500°C.

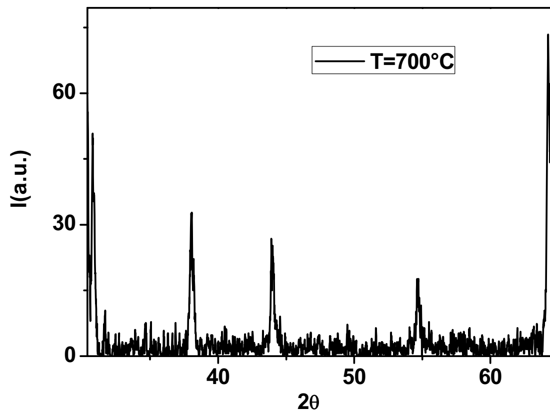

Fig.5.34. XRD patterns for PZT/ITO/glass samples annealed at 700°C.

The PZT/ITO samples diffraction peaks become detectable for thermal treatments above 500°C where the peaks at 44° and 64.30°, assigned to the (200) and (220) crystal planes of perovskite phase, respectively, can be seen (Fig. 5.33). The increased crystallization of the PZT films, induced by the highest thermal treatment, can be seen in Fig.

5.34. In fact, the two peaks, seen above, increase their intensity and others peaks appear at 30.79°, 38.03° and 54.70°, related respectively to the (110), (111), and (211) planes of perovskite phase (Fig.5.34). The FWHM of XRD peaks result to be quite small indicating the presence of crystalline domains extended at least on micrometer scale.

On the other hand, the investigations performed on the PZT films deposited on silicon wafers annealed at 500°C have shown a quite broad XRD peak around 30°, with a FWHM of more than 6° (Fig.5.35); in the Si-samples annealed at 700°C such peak shows a FWHM of 1.6°, as it can be seen in Figure 5.35;

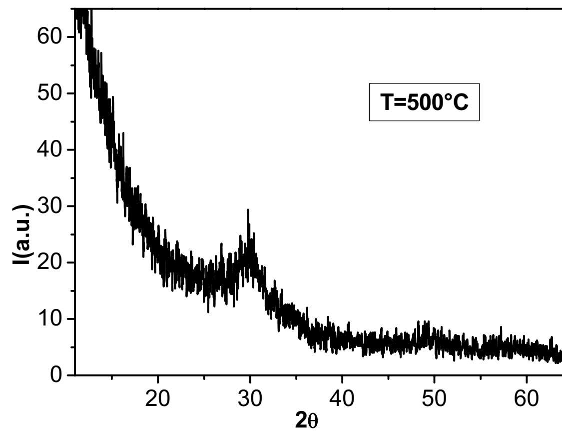

Fig.5.35. XRD patterns for PZT/Si samples annealed at 500°C.

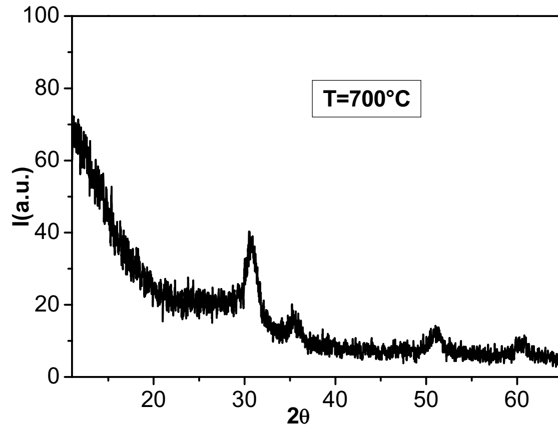

Fig.5.36. XRD patterns for PZT/Si samples annealed at 700°C.

The others peaks shown in Fig.5.36 fall at 30.62, 35.30, 51.04, 60.43°, which correspond to the (222), (400), (440), (622) planes of the pyrochlore cubic phase, respectively.

The size of the crystalline phases has been obtained by using the Debye-Scherer formula (5.4.6) and the results are summarized in Table I:

$$D = \frac{0.9\lambda}{\Delta(2\theta)\cos(\theta_0)} \qquad (5.4.6)$$

Table I. Sizes of the crystalline domains of PZT/Si wafer substrates obtained by using the Debye-Scherrer formula

T(°C)	W (deg)	D (Å)
500	6.6	12
700	1.7	57

As it can be seen, in Table I, the size of the crystal domains increases as well as the annealing temperature. Nevertheless, in the case of Si substrate, the domains for the highest annealing temperatures samples can still be considered nanocrystalline [7-9].

In fact, the lattice parameter of the unit-cell is 10.1 Å, slightly far from the value 10.40 Å found in literature [8], but it has been shown [9] that this value monotonically decreases from 10.40 to 10.16 Å when the deposition temperature increases from 560 to 700°C.

The results on silicon wafer substrate confirm that the PZT phase transition is strongly affected by the substrate.

5.1.6 Morphological evolutions

In Figure 5.37 the SEM images collected on the PZT/ITO samples annealed at 500°C and 700°C for 10 hours are shown. The highest annealing temperature induced evident structural modifications of the PZT layers which show that the almost complete nucleation of “rosetta” structure occurs; the “rosetta” structures grow in a radial shape and they cover the substrates by touching each other (see Figs. 5.37.c and 5.37.d).

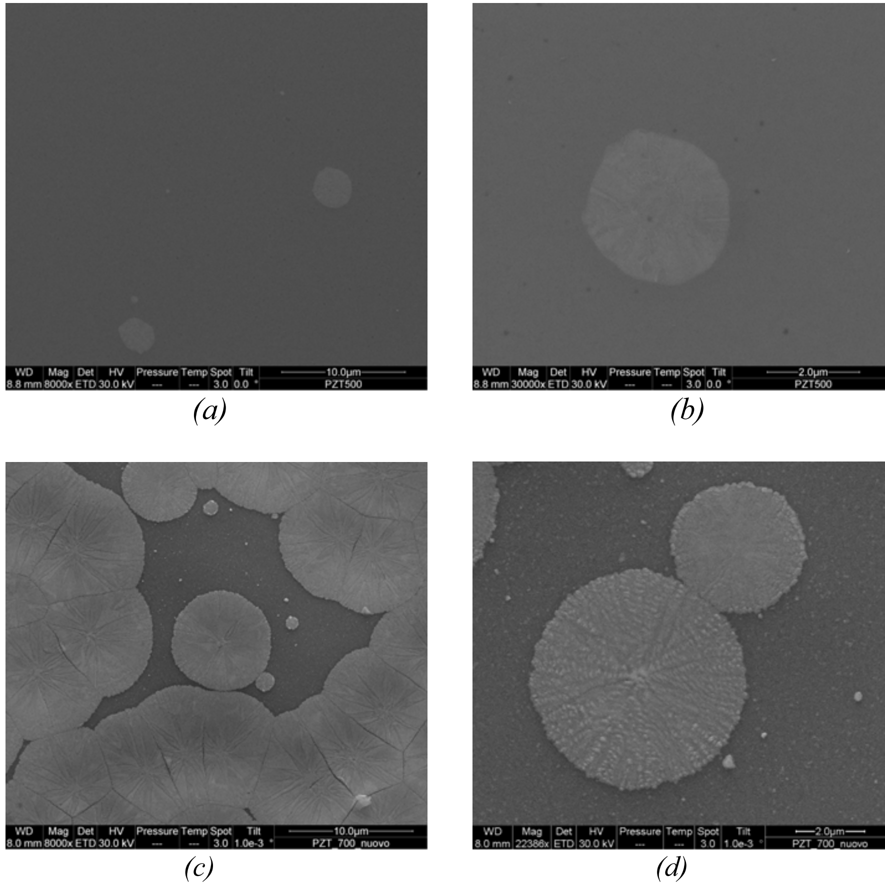

Fig.5.3.7. SEM images showing various steps of the in situ phase transition of a PZT film deposited on ITO substrate: step at 500°C (a), a particular of the same step (b), step at 700°C (c), and a particular of the same step (d).

The “rosetta” structures do not occur on the PZT deposited on silicon wafers annealed at 700°C. In fact, as it is shown, for comparison, in Figure 5.38, such samples show quite homogenous surfaces interrupted by some fractures; only the grey parts were seen for increased magnifications. The visible PZT fractures are due to thermal stress,

attributed to the different thermal strain coefficient between the PZT and silicon substrate. [5]

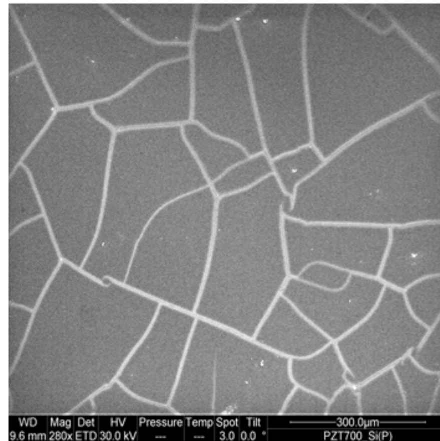

Fig.5.38 SEM image of PZT/Si surface

The absence of the nucleation centres, on the PZT/Si-wafer, demonstrates that the “rosette” structures are induced by the ITO/glass substrates. That is, the ITO substrates play a specific role in the perovskite phase formation, when the samples are annealed at temperature higher than phase transition temperature [5].

The surfaces topographies of the samples have been obtained by AFM investigations. The AFM image collected on the PZT/Si wafer annealed at 700°C, as above for the SEM images, results to be homogeneous flat surface and then not shown. On the contrary, the roughness of the glass/ITO/PZT sample annealed at 700°C is shown in Figure 5.39, where the nucleation centres of the rosette structures can be seen.

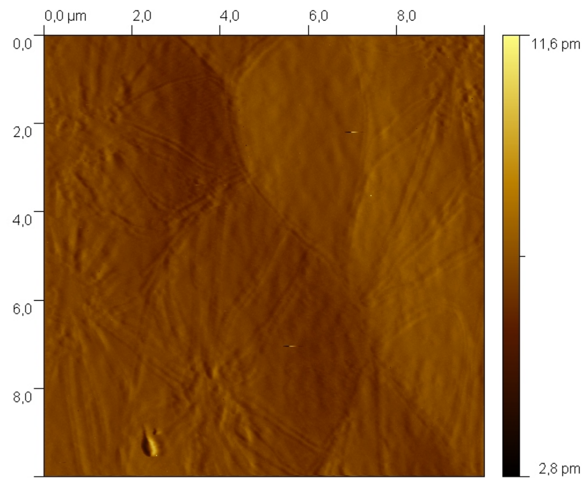

Fig.5.39. AFM image of PZT/ITO/glass surface.

This difference in the surface roughness is also due to the transition from amorphous PZT to crystalline perovskite phase, occurring at ITO defect sites when the samples are annealed at high temperatures.

5.1.7 Electrical response studies

Detailed mapping of the electric polarization have been obtained by Electric Force Microscopy (EFM). The EFM images collected on PZT\ITO\glass samples annealed at 600°C for 10h are shown in Figure 5.40, where it is possible to see the presence of black and white lines on the middle of the figures.[6]

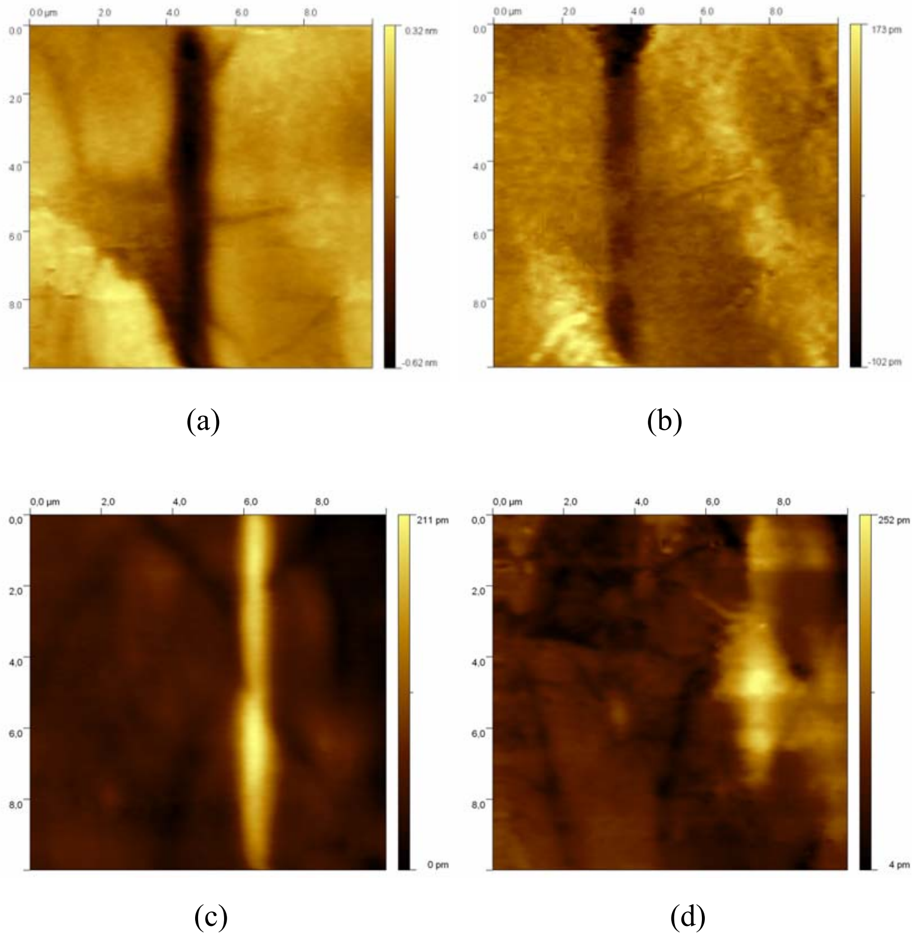

Fig.5.40. No Contact EFM image of the PZT sample annealed at 600°C for 10h, black line written with -10V (a), same line after 28h (b), white line written with +10V (c), same line after 50h (d)

Such black and white lines represent the electric polarizations on the surface induced by applying a dc voltage, -10V and +10V, respectively, between the tip and the ITO layer (writing process) [6]. The polarization induced by negative voltage (black line) becomes less detectable after 28 hours, as it can be seen by comparison of Fig. 5.40a (EFM images collected just after the writing process) and Fig.5.40b (images collected after 28 hours). On the contrary, the positively induced

polarization (white line) is still detectable for times longer than 50 hours, as it results from the comparison of Fig. 5.40c (just after writing) and Fig. 540d (50 hours later). Such findings indicate an asymmetric behaviour of the electric polarization persistence on the surface.

Different findings were obtained by performing the same EFM investigation on the samples annealed at temperatures lower than 600°C, always for 10 hours. The EFM images of the sample annealed at 400°C are shown in Fig. 5.41, to be compared with those of Fig.5.40.

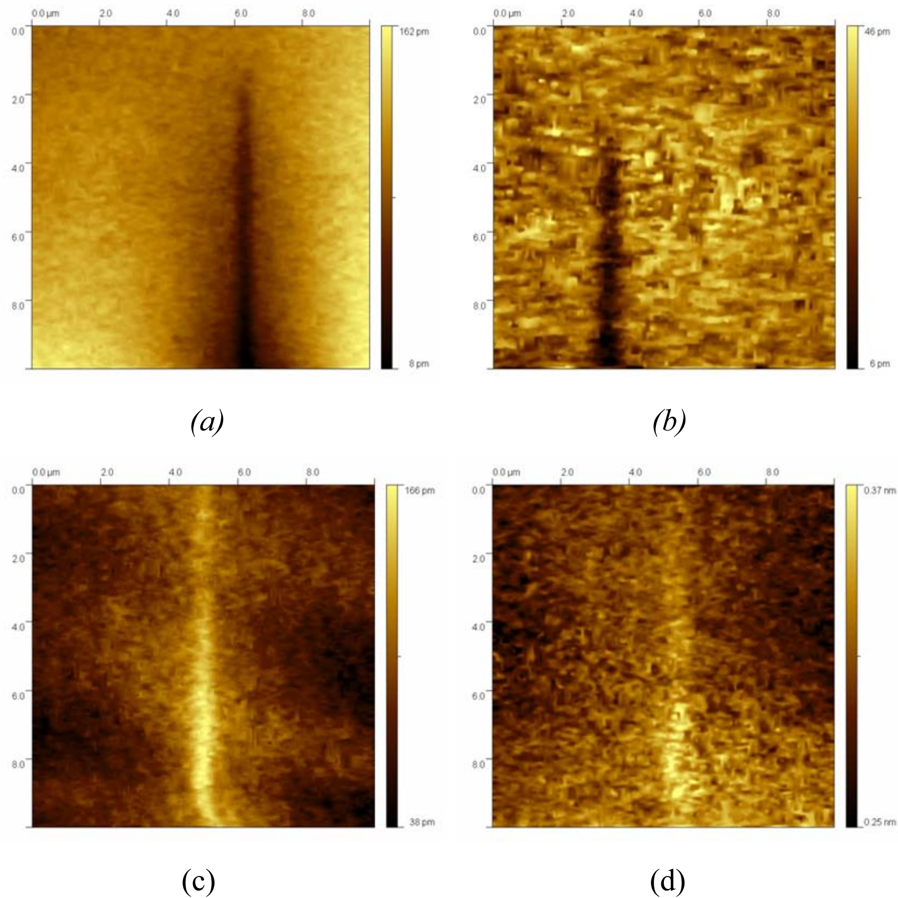

(a) *(b)*

(c) (d)

Fig.5.41. No Contact EFM image of the PZT sample annealed at 400°C for 10h, black line written with -10V (a), same line after 28h (b), white line written with +10V (c),same line after 5h (d)

It can be seen that, whereas the negative induced polarization (black line) still remains detectable for 28 hours (Fig. 5.41b), the positive induced polarization (white line) disappears after only about 5 hours (Fig. 5.41d).

The corresponding EFM images collected straight after the writing processes are reported in Fig. 5.41 (a and c), to show all the evolution. For these samples the phase transition is not complete, as previously shown also by the XRD (Figs.5.33 and 5.34) and SEM (Fig.5.37a) characterization.

The effect of the annealing times on the polarization behaviours of these PZT layers has been also investigated. In fact, it has been seen elsewhere [6] that the same samples subjected to identical annealing temperatures but only for 1 hour (against the 10 hours), show a different behaviour. For the samples annealed for an hour, the negative induced polarizations (black lines) remains longer than the positive induced polarization (white lines) independently from the annealing temperatures and anyway lower than those seen above (5 hours). Such behaviour can be ascribed to the kinetic of the phase transition. In fact, if the permanence of the positive induced polarization (white line) is due to the increased presence of the PZT in perovskite phase, then the 1 hour thermal treatments do not allow the whole layer to make the phase transition, independently of the annealing temperature. In this way, it can be explained why the positive induced polarization never prevails for the samples subjected to 1h treatments. However, the reduced durations of the induced polarization on the samples annealed for 1 hour, with respect to those annealed for 10 hours, might be due to the lower number of crystalline domains responsible of the polarization effect.

The possibility to overwrite by using opposite voltages is shown in Fig.5.42, on a sample annealed at 600°C for 10 hours. The 4x4 μm^2 white square area was obtained by using a positive voltage (+10V), while the 2x2 μm^2 dark square area was obtained by using a negative voltage (-10V) inside the white region. In Fig.5.6.4 are shown the images collected just after the writing processes (a) and after two hours (b).

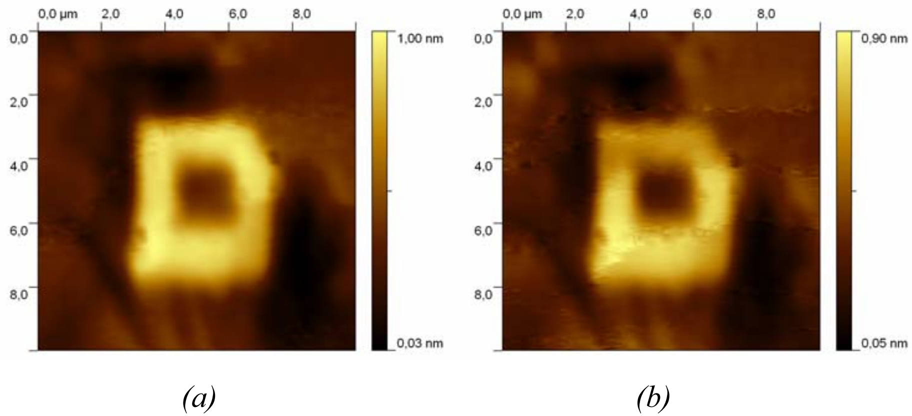

(a) *(b)*

Fig 5.42 White square 4x4μm² area (positive induced polarization) and black square 2x2μm² area (negative induced polarization) on PZT/ITO/glass at 600°C for 10h: (a) Straight after the writing process and (b) 2h later

The permanency of the two polarization states after two hours, with a good spatial resolution, confirms the stability of both states of the ferroelectric film.

5.1.8 Conclusion

The use of different experimental techniques as XRD, SEM, AFM and EFM allowed us to obtain important information about the structure and the electric characterization of PZT thin films deposited on different substrate. The EFM technique was used to investigate the ferroelectric properties of the PZT layers and the effect of the induced polarization was monitored as a function of the time.

XRD technique reveals the presence of a nanocrystalline pyrochlore phase in the PZT/Si samples, while the ferroelectric perovskite phase grows only in the PZT/ITO/glass samples, showing a complete crystallization for increasing temperature and annealing time.

The morphology of both PZT phases was revealed by the SEM analysis: the presence of dendritic "rosetta" structures was observed only when the PZT is deposited on ITO substrate, while, on silicon substrate, a flat PZT layer, constituted by undistinguished nanocrystals, shows fractures due to thermal stress, attributed to the different thermal strain coefficient between PZT and Silicon wafer.

Moreover, by the EFM images collected on glass-ITO-PZT samples, it has been possible to distinguish, at least qualitatively, two different behaviours of the induced polarizations, depending on annealing temperature, lower or higher than 600°C. In the samples annealed below 600°C, the electric polarization lines written by negative voltage (in our convention, black line), are more persistent than the white ones, written with positive voltage. Above 600°C the stability properties of such polarizations are inverted.

A detailed explanation of such behaviour is difficult to elaborate, but a tentative hypothesis can be proposed, associating the different persistence of the induced electric polarizations to the different amount of spontaneous polarization of the ferroelectric phase, as it has been shown

elsewhere. It could be influenced by some “local” electric field generated by the particular spontaneous charge distribution at the PZT-ITO interface, which depends, in turn, by the phenomena of ion migration occurring under high temperature annealing. It is reasonable that for higher temperature and longer annealing times the electric response is mainly due to the polarization of the ferroelectric phase, almost completely grown after such treatments, while in the other case (lower annealing temperature or shorter times) the direct effect of surface charge distribution could be taken into account.

Other possible interpretation associates the asymmetric behaviours shown above to the presence of oxygen vacancies. In fact, such oxygen vacancies behave differently depending on the PZT composition, i.e., they migrate toward the PZT/air interface for low ratio Zr/ (Zr+Ti) (<0.25) or towards the ITO/PZT interface for high ratio Zr/ (Zr+Ti) (>0.25). Such positive charge displacements give rise to internal fields that could be responsible for the favourite orientations of the ferroelectric dipoles.

Measurements of macroscopic hysteresis of the sample annealed at 800°C show also an asymmetric behaviour respect the two polarizations. In particular, you may notice a voltage shift (imprint) towards the negative part probably due to a preference of polarization-induced on the negative voltage. This behaviour is also confirmed by microscopic NCEFM measures. In all probability the imprint phenomenon is due to an asymmetry in the distribution of trapped charges, such as electrons and oxygen vacation [11-18]

In the topographic images obtained with both the AFM and SEM, we see clearly that with increasing annealing temperature the surface structure changes (Figure 5.20 and 5.22) revealing the presence of "white" particles and rosette (cluster) of irregular shape and size ranging from few microns to a few nanometers, due probably to the nucleation of

ferroelectric domains. The SEM microanalysis, performed on these areas, shows the presence of PZT. Even in areas between adjacent "rosette", as shown in Figure 5.26 it is evident the presence of PZT, excluding the possibility that the fractures between the rosettes are the result of thermal stress. All this suggests that of the range of temperature from 500°C to 800°C the samples have undergone a phase transition from an amorphous structure to an ordered structure, indicative of crystallization.

These same results are confirmed by some work existing in literature on substrates of silicon-platinum and iridium oxide IrO_2 [10].
More detailed studies on the influence of conductive substrate (ITO), the concentration ratio of zirconium-titanium and of the thickness of the determining the direction of polarization, will be further developed.

To conclude the excellent control of the experimental set up and the characteristics of ferroelectric materials examined provided nanoscale “egocentric typographic freedom "as you can see from the figure below.

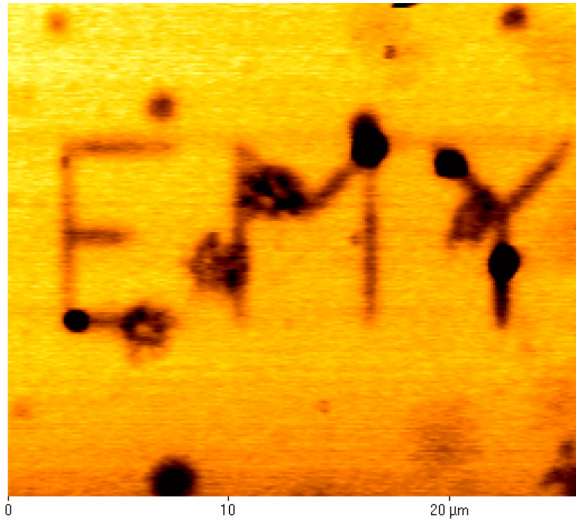

The results obtained on samples of PZT deposited on ITO are encouraging because in agreement with others experimental works extensively documented in the literature. Further quantitative studies related to ferroelectric and piezoelectric properties in the immediate future, will allow more control on the potential of these materials in various fields of application.

References

[1] C.T. Lin, B.W. Scanlan, J.D. McNeill, J.S. Webb, Li Li, R.A. Lipeles, P.M. Adams and M.S. Leung,

[2] S. S. Dana, K. F. Etzold and S. Clabes, "Crystallization of sol-gel derived lead zirconate titanate thin films", Journal of Applied Physics 69, 4398 (1991).

[3] Science and technology of Electroceramic Thin films (NATO/ARW Series E), edited by O. Auciello and R. Waser (Kluver, Deventer, 1994), Vol. 284.

[4] D. Damianovic, "Ferroelectric, dielectric and piezoelectric properties of ferroelectric thin films and ceramics," thesis, Swiss Federal Institute of technology-EPFL, Lausanne, Switzerland (1998).

[5] S. Marino, M. Castriota, G. Strangi, E. Cazzanelli and N. Scaramuzza, Journal of Applied Physics 102, 013112 (2007).

[6] E. Bruno, M. P. De Santo, M. Castriota, S. Marino, G. Strangi, E. Cazzanelli and N. Scaramuzza, Journal of Applied Physic*s* 103, 1 (2008).

[7] Harold P. Klug, Leroy E. Alexander "X Ray diffraction procedure*s"* John Wiley & sons, inc. 1970.

[8] G. Barucca , A. De Benedittis , A. Di Cristoforo , G. Majni , P. Mengucci, F. Leccabue and B. E. Watts, "Crystallization of perovskite PZT films on MgO substrates", Thin Solid Films 319, 207 (1998).

[9] L'H. Famedi, M. Guilloux-Viry, A. Perrin, Z. Z. Li and H. Raffy, "Support-Promoted stabilization of the metastable PZT Pyrochlore phase by Epitaxial thin film growth" Journal of Solid State Chemistry 158, 40 (2001).

[10] D. Van Genechten, G. Vanhoyland, J D.Haen. J Johnson, D J Wouters, M. K. Van Bael, H. Van den Rul, J Mullens, L. C. Van Pouche: Thin Solid Film 476 104-111 (2004)

[11] S. W. Jiang, O. Y. Zhang, W. Huang. B. Jiang: Applied Surface Science. (2006).

[12] A. Gruverman, O. Auciello, H. Tokumoto: Appl. Phys. Lett., 69 3191 (1996).

[13] Jian Shen et al. Appl. Surf. Science (2006).

[14] Y. J. Oh, J. H. Lee, W. Jo: Ultramicroscopy (2005).

[15] B. Watts et al. Electroceram, 11-139 (2003).

[16] B. Watts et al. Eur. Ceram. Soc.25-2495 (2005).

[17] A Wu, et al. Nanotechnology 16 2587-2595 (2005).

[18] Tien-I Chang et al. Iournal of Alloys and Compounds 414, 224-229 (2006).

Chapter 6

Direct Measurement of Surface-Induced Orientational Order Parameter Profile above the Nematic-Isotropic Phase Transition Temperature

6.1.1 Introduction

The spatial and temperature dependence of the surface-induced orientational order parameter $S(z_0\ t)$; was determined in the isotropic phase. An optical fiber was immersed in a thin liquid crystal layer and the retardation was measured as a function of the fiber's height above the surface, from which the model-independent $S(z_0\ t)$; was deduced with resolution $\lesssim$ 2nm. It was found that :

(i) $S(z=0) \leq 0.12$ close to the nematic transition temperature,

(ii) the susceptibility is mean-field-like,

(iii) $S(z,T)$; deviates significantly from exponential spatial decay. The results are discussed in terms of a nonlocal potential.

6.1.2 Results and discussion

Surface-induced orientational order at the nematic-isotropic (NI) phase transition has received extensive scrutiny [1–22]. Above the bulk first order NI temperature T_{NI}, an appropriately prepared surface induces orientational order in the otherwise isotropic phase, with the order decreasing into the bulk. The behaviour of the scalar orientational order parameter $S(z) = (3\backslash 2 \cos^2\theta - 1\backslash 2)$, where θ is the angle from the nematic director $\hat{n}$) depends on the interaction energy between the liquid crystal

(LC) and the alignment layer(s), the physical properties and thickness of the LC layer, and the temperature T. It generally is assumed that the surface potential is localized to the interface at z = 0 [3,5,10,11], with the uniaxial order parameter at the interface S_0 [≡(S=0)] determined by the form of the potential [3,5,9,11]. If the surface-induced order is not sufficiently large, only partial wetting by the nematic phase occurs.

On the other hand, if the interaction between the LC and the surface is strong, S(z) integrated through the cell thickness diverges logarithmically on approaching T_{NI} [1–3,12]; this corresponds to complete wetting by the nematic phase. Moreover, ‘‘capillary condensation’’ a transition to the nematic phase in a localized boundary layer has been predicted [4,11] and observed experimentally [13,17–19]. Sheng also predicted [5] a ‘‘pre-wetting transition’’ in which there is a discontinuous jump of S_0 at a temperature T>TNI, which also has been observed experimentally [22].

To date quantitative determinations of the order parameter profile S(z) versus temperature have used probes with visible light wavelength resolution—this is much larger than the length scale of the surface layer and so required specific models in conjunction with the macroscopic data in order to extract S(z) [1,2].

Other techniques that measure local quantities, such as evanescent wave and second harmonic generation experiments [6–9], also require specific models to extract S(z).

Recently, however, we have shown that the light intensity emerging from a tapered optical fiber immersed in a LC film and passing through an analyzer is well approximated by the total optical retardation α from the fiber aperture through the birefringent medium to the surface [23,24]. This allows us to obtain orientation order information in three dimensions out to z~500 nm above the interface, with lateral resolution

~125 nm and vertical resolution ~2nm. Here we apply this technique to surface-induced nematic order, whereby we measure α between the fiber aperture and the substrate as a function of the aperture's height h above the substrate and temperature T>TNI.

This allows us to extract the model-independent profile S(z) vs T close to the substrate. In particular, we find that $S_0 \lesssim 0{:}12$ and that S_0^{-1} vs T is mean-field-like, scaling approximately as $T - T^*$, where T^* is the supercooling limit of the isotropic phase, indicating the absence of capillary condensation in our system for the temperatures studied. Moreover, we found that dα/dh varies slowly with h out to h ≈ 10 nm, substantially different from the quasi exponential decay expected for weak surface-induced order in the absence of capillary condensation [3,5].

A glass substrate was spin coated with the polyamic acid RN-1175 (Nissan Chemical Industries, Ltd.), prebaked according to manufacturer's specifications at 100 °C for 3 min, then fully baked at 230°C for 60 min to achieve imidization. To establish the azimuthal orientation of the planar alignment, the polyimide-coated slide was rubbed with a rubbing strength $n_f = 1.5 \times 10^6\ cm^{-1}$ using a cotton cloth and rubbing machine [25].

Atomic force microscope measurements of the resulting surface revealed a short wavelength roughness with characteristic length scale ~30–40 nm and rms amplitude A_r ~ 1:5nm, as well as longer wavelength (L ~ 1 μm) grooves with a rms amplitude Ag < 1nm due to the rubbing cloth's crenellations [26]. The slide then was coated with a thin film (a few μm) of the LC pentylcyanobiphenyl (''5CB'', Merck) and placed into a Veeco Aurora near-field scanning optical microscope. (See Fig. 1 in Ref. [24]). The approximately conical-shaped fiber (cone angle 10°) was illuminated by circularly polarized light (extinction ratio ~1.2:1) at wave-length λ= 532 nm that first passed through a light chopper. The light emerged from the fiber's flat aperture (aperture width ~65 nm; total

diameter d_f < 200 nm, including Al cladding), which was immersed into a thin layer (a few μm) of LC.

The approximately circularly polarized transmitted light passed through the LC, the alignment layer, the glass slide, an analyzer rotated by 45°C with respect to the rubbing direction, and was collected by a photomultiplier tube. The photomultiplier tube output was input to a lock-in amplifier referenced to the light chopper; a 10 s time constant filter was used to average out the noise. The entire assembly was housed in a box, with a string of resistors placed along the box's inner walls and connected to a temperature controller; good thermal stability (<10mK) and homogeneity ($\nabla T < 5 mKcm^{-1}$) were maintained.

The sample was stabilized ~1.8 °C above T_{NI} and the fiber was lowered to make contact with the substrate, corresponding to $z = 0$. In light of the long time constant filter, the intensity was recorded after a delay of approximately 50 s. The fiber then was elevated a few nanometers, the signal was allowed to stabilize for another 50 s, and the intensity was again recorded.

This procedure was repeated about 20 times in order to construct an intensity I vs height h profile at this temperature. The temperature then was reduced by a few tens of millikelvins and, after allowing 2 h for the temperature to stabilize, the measurement procedure was repeated to obtain I vs h at this temperature. Data were collected at multiple temperatures down to T_{NI} + 50 mK, where T_{NI} was found to drift by <10 mK over the duration of the entire experiment. Figure 1(a) shows I vs h for all temperatures relative to T_{NI}, where the position of each baseline varied from run to run. It is apparent that I varies linearly with h out to ~10 nm, beyond which dI/dh decreases until I becomes constant for h $\gtrsim$ 30 nm.

To relate (I, T) to a physical quantity, we note that at fixed T, I is approximately $\propto$ α, although the proportionality constant C(T) was found empirically to depend on T due to the thermal characteristics including those due to ∇T of the fiber. To obtain C(T), we placed a top slide treated for homeotropic alignment on the sample, using a spacer of nominal thickness 10 μm. The now enclosed cell was then placed into a temperature controller and Pockels cell-based birefringence apparatus [27]. The beam from a He-Ne laser at wavelength λ_0 = 633 nm was focused to a spot of ~100 μm at the sample, and the total retardation α_{tot} (T) through the cell was measured versus T.

Because α_{tot} (T)=C(T)ΔI(T), where ΔI(T) is the intensity difference between the baseline (at h=0) and saturation intensities, C(T) was extracted and the intensity data in Fig. 6.1(a) were converted to retardation α vs h at each temperature [Fig. 6.1(b)] for wavelength λ_0.

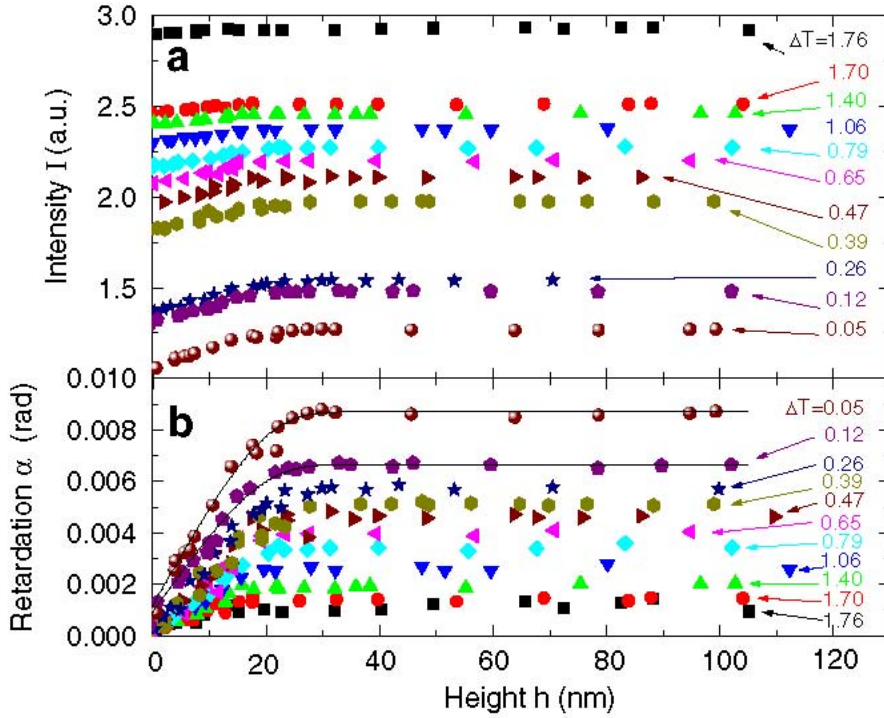

FIG. 6.1 (colour online). (a) Intensity versus aperture's height h above substrate at temperatures ΔT ($T - T_{NI}$). The different baselines for each ΔT are due to slow drifts compared to the data acquisition time and to a systematic variation of the baseline with temperature due to the thermal characteristics of the fiber. (b) Retardation α versus height h extracted from intensity data in (a) and normalized to the total retardation α_{tot} (T) through entire cell. Each set of data was regularized (see text), and two examples are shown by the solid lines.

Let us now turn to the meaning of α vs h.

We note that $\alpha(h) = \int_0^h k_0 \Delta n(z)\, dz$ where

$k_0 = \frac{2\pi}{\lambda_0}$ and $\Delta n(z)$ is the LC birefringence at λ_0= 633 nm at height z.

Because Δn =DS for small S, where the proportionality constant D = 0.28 for 5CB [28,29],

$$\alpha(h) = k_0 D \int_0^h S(z)dz .$$

That $\alpha \propto$ h for h $\lesssim$ 10 nm suggests one of two scenarios: Either (i) S(z) varies weakly over this range or (ii) S(z) varies significantly with position h of the fiber aperture but its integral always happens to be proportional to h over this range.

We discount mechanism (ii) because it would require the coincidence of far too many conditions, such as anchoring potentials at the substrate and fiber having the correct forms. Thus we believe that S(z) decays slowly near the substrate (over a length$\gg$ Ar), which will be discussed in more detail below.

Hence $$S_0 = \left(\frac{d\alpha}{dh}\right)_{h=0} / k_0 D .$$

In order to differentiate numerically the data in Fig. 1(b) and avoid the noise associated with numerical differentiation, we fitted a piecewise smooth Bezier curve of third degree to five representative data points, matching the values and derivatives for each section. Typical examples are shown by the solid curves in Fig. 1(b). S(z,T) then was obtained from the derivative of the Bezier curve; results are shown in Fig. 6.2. From Fig. 6.2 we extract S_0 and plot S_0^{-1} vs T in Fig. 6.2, inset. There are three important features.

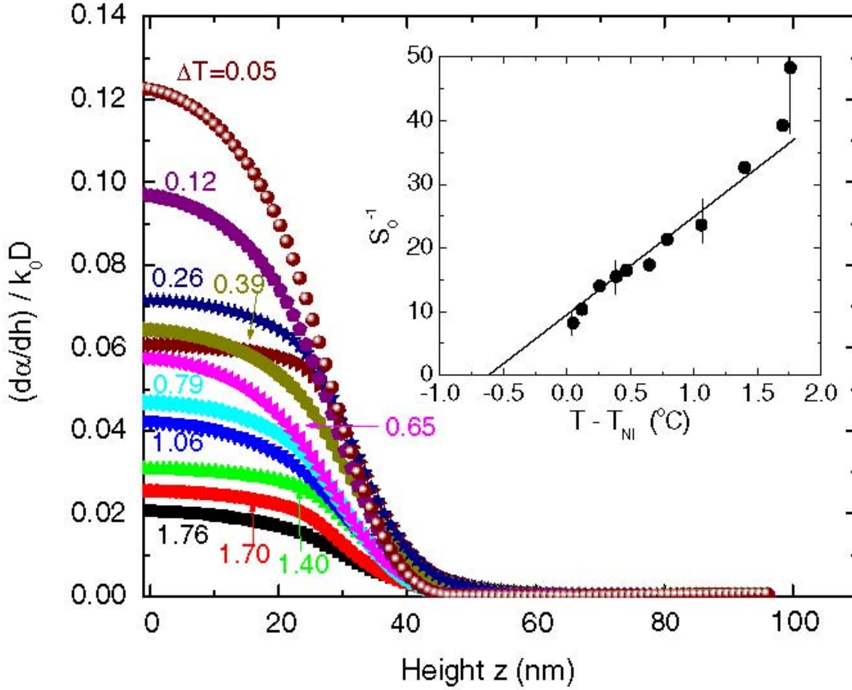

FIG 6.2 (colour online). The quantity (dα=dh)/k₀D (which is ≈S) versus height h. Inset: S_0^{-1} vs T - T_{NI}.

First, S_0 is relatively small for all T, having a maximum value of S_0 ≈ 0.12 at T - T_{NI} = 0.05°C. These are much smaller than values predicted [4,5] and measured experimentally [13,17] when capillary condensation occurs. The data also indicate that no pre wetting transition [5] was observed, at least for T>T_{NI} + 0.05 °C.

Second, the behaviour of S_0^{-1} vs T in Fig. 2, inset, is reminiscent of the mean- field behaviour for the orientational susceptibility in the isotropic phase, associated with a susceptibility exponent γ = 1 and a value to T_{NI} -T^* ~ 1 °C. The observed downward deviation of S_0^{-1} close to

T_{NI} also is commonly observed [30] in bulk measurements, although in our case this may be due to experimental scatter.

In contrast, Sheng's model [5] for capillary condensation for walls spaced <5nm apart predicts a highly nonlinear variation of S_0^{-1} with temperature and $T_{NI} - T^* > 4$ °C, which is contrary to our results.

Third, dα/dh ~ 0 for h> 30 nm, indicating that S ~ 0 beyond this range. This length scale differs sharply from that of capillary condensation, where $S \neq 0$ is observed experimentally for substrates separated by hundreds of nanometers [13]. Overall, our results suggest that there are no observable confinement effects because of the weak LC order at the rubbed polyimide and because the interaction potential between fiber and LC is very small. This negligible interaction with the fiber's surface is consistent with previous work over a wide range of length scales by our group and others [23,24,31].

Nevertheless, even in the absence of any preferred surface alignment or ordering, there exists a torque like natural boundary condition $dS/dz\big|_{z=h}$ at the fiber. On applying Sheng's model [5] to calculate S(z, T) when $S_0 \lesssim 0.12$ with this boundary condition, we obtain profiles for S(,T), we equate this with $(d\alpha/dh)_{h=z} / k_0D$, that differ by less than 10% from profiles in the absence of a fiber, i.e., with $dS/dz\big|_{z\to\infty}$. Thus taking account of all of our observations, a posteriori we can treat $(d\alpha/dh)_{h=z} / k_0D$ as approximately S(z), facilitating its measurement without requiring a specific model.

Beyond the surface, perhaps our most important observation is that S(z) falls off slowly over several nanometers before decaying more rapidly. This behaviour is not consistent with the exponential decay [characterized by a nematic correlation length ξ(T) that is expected when S_0 is small [3,5]; a possible mechanism for the decay profile will be

discussed below. Nevertheless, the increase in the aperture height h_s with decreasing T at which α seems to saturate [Fig. 6.1(b)] presumably is due to an increase of ξ(T) on approaching the transition. To make this more apparent, Fig. 6.3 shows the quantity α/S_0 at three representative temperatures. As expected, the initial slopes are the same, but at higher temperatures α/S_0 ''saturates'' at a height h_s lower than it does at temperatures closer to T_{NI}.

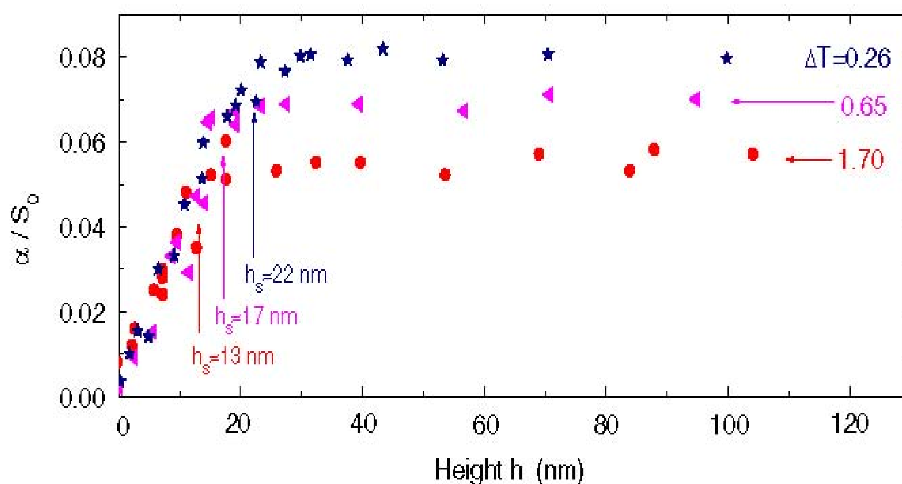

FIG.6. 3 (colour online). The quantity α/S_0 versus height at three representative temperatures. Vertical arrows show the height h_s (± 3nm) at which α saturates.

The initial slow spatial decay of S(z) raises questions about the physics near the interface. Hsiung et al. assumed an exponential form for S(z) to analyze their evanescent wave ellipsometry data, obtaining an excellent fit and information about ξ vs T [7]. In their case this form likely was justified, as their homeotropic alignment was controlled by silane molecules at the surface that provided a well localized potential. In our

experiment, however, we obtain planar alignment by mechanically rubbing a polyimide. The rubbing process has two effects: It creates long wavelength grooves [26] and it realigns the polymer backbone, which can extend to some depth into the polyimide layer. Because $L \gg d_f$ and Ag is small, the grooves have little influence on S_0, except in the region $z \lesssim$ Ag.

On the other hand, the realignment of the backbone can extend many nanometers into the polymer film [8,32,33]. Given this situation, Barbero and Evangelista showed [34] how quadrupole-quadrupole interactions can act over a range of several nanometers; an inhomogeneous spatial distribution of adsorbed charges at the interface [35] also would give rise to nonlocal forces. Nonlocal interactions have been shown to affect physical quantities such as surface viscosity [36] and elasticity in freestanding smectic-C films [37], where the length scale of the interactions extends $\xi \sim 5$–10 nm and results in a reduced elastic constant for films thinner than ξ [37]. The data near $z = 0$ in Fig. 6.2 clearly show deviations over these length scales from Landau– de Gennes behavior with a highly localized potential. We therefore speculate that the nonlocality of the ''surface'' potential may be playing the central role. To be sure, such a scenario does not necessarily apply to all interfaces; as noted above, orientation from a surface agent (e.g., silane) is likely to be highly localized. Nevertheless, for planar alignment that relies on anisotropic attractive interactions, especially those in which the anisotropy extends some distance beneath the surface and into the ''bulk'' polymer alignment film, the extended range of interactions may result in an $S(z)$ profile within several nanometers of the interface that is very different from exponential decay. To summarize, we have demonstrated that a variation on optical nanotomography [23,24] facilitates a model-free approximate determination of the surface-induced orientational profile. Moreover, the behaviour of S vs z is very different from that expected from the oft

assumed Landau– de Gennes model with a localized surface potential, suggesting that a non-local potential and/or other mechanisms (e.g., short range molecular clustering [38,39]) are needed to describe this behaviour.

References

[1] K. Miyano, Phys. Rev. Lett. 43, 51 (1979); J. Chem. Phys. 71, 4108 (1979).

[2] J. C. Tarczon and K. Miyano, J. Chem. Phys. 73, 1994 (1980).

[3] D.W. Allender, G. L. Henderson, and D. L. Johnson, Phys. Rev. A 24, 1086 (1981).

[4] P. Sheng, Phys. Rev. Lett. 37, 1059 (1976).

[5] P. Sheng, Phys. Rev. A 26, 1610 (1982).

[6] W. Chen, L. J. Martinez-Miranda, H. Hsiung, and Y.R. Shen, Phys. Rev. Lett. 62, 1860 (1989).

[7] H. Hsiung, Th. Rasing, and Y. R. Shen, Phys. Rev. Lett. 57, 3065 (1986).

[8] M.B. Feller, W. Chen, and Y.R. Shen, Phys. Rev. A 43, 6778 (1991).

[9] T. Moses and Y. R. Shen, Phys. Rev. Lett. 67, 2033 (1991).

[10] T. J. Sluckin and A. Poniewierski, Fluid and Interfacial Phenomena, edited by C.A. Croxton (John Wiley & Sons, New York, 1986).

[11] T. J. Sluckin and A. Ponewierski, Liq. Cryst. 2, 281 (1987).

[12] B. Je ´ro ˆme, Rep. Prog. Phys. 54, 391 (1991).

[13] H. Yokoyama, S. Kobayashi, and H. Kamei, Mol. Cryst. Liq. Cryst. 99, 39 (1983); J. Appl. Phys. 61, 4501 (1987).

[14] G. Barbero and G. Durand, J. Phys. II (France) 1, 651 (1991).

[15] R. Barberi and G. Durand, Phys. Rev. A 41, 2207 (1990).

[16] S.-T. Wu and U. Efron, Appl. Phys. Lett. 48, 624 (1986).

[17] A. Borstnik Bracic, K. Kocevar, I. Musevic, and S. Zumer, Phys. Rev. E 68, 011708 (2003).

[18] K. Kocevar, A. Borstnik, I. Musevic, and S. Zumer, Phys. Rev. Lett. 86, 5914 (2001).

[19] K. Kocevar and I. Musevic, Phys. Rev. E 64, 051711 (2001).

[20] B. Wen, J.-H. Kim, H. Yokoyama, and C. Rosenblatt, Phys. Rev. E 66, 041502 (2002).
[21] J.-H. Kim and C. Rosenblatt, J. Appl. Phys. 84, 6027 (1998).
[22] X. Liu, D.W. Allender, and D. Finotello, Europhys. Lett. 59, 848 (2002).
[23] V. Barna, A. De Luca, and C. Rosenblatt, Nanotechnology 19, 325709 (2008).
[24] A. De Luca, V. Barna, T. Atherton, G. Carbone, M. Sousa, and C. Rosenblatt, Nature Phys. 4, 869 (2008).
[25] J.-H. Lee, T. J. Atherton, D. Kang, R.G. Petschek, and C. Rosenblatt, Phys. Rev. E 78, 021708 (2008).
[26] M. P. Mahajan and C. Rosenblatt, J. Appl. Phys. 83, 7649 (1998).
[27] C. Rosenblatt, F. F. Torres De Araujo, and R. B. Frenkel, Biophys. J. 40, 83 (1982).
[28] P. P. Karat and N.V. Madhusudana, Mol. Cryst. Liq. Cryst. 36, 51 (1976).
[29] N.V. Madhusudana and R. Pratibha, Mol. Cryst. Liq. Cryst. 89, 249 (1982).
[30] T.W. Stinson, J.D. Litster, and N.A. Clark, J. Phys. (Paris) 33, C1-69 (1972).
[31] T. Tadokoro, T. Saiki, and H. Toriumi, Jpn. J. Appl. Phys. 41, L152 (2002); Jpn. J. Appl. Phys. 42, L57 (2003).
[32] J.-H. Kim and C. Rosenblatt, J. Appl. Phys. 87, 155 (2000).
[33] S. Kuniyasu, H. Fukuro, S. Maeda, K. Nakaya, M. Nitta, N. Ozaki, and S. Kobyashi, Jpn. J. Appl. Phys. 27, 827 (1988).
[34] G. Barbero and L. R. Evangelista, Adsorption Phenomena and Anchoring Energy in Nematic Liquid Crystals (Wiley, New York, 2005).
[35] G. Barbero and G. Durand, J. Appl. Phys. 67, 2678 (1990).
[36] G. E. Durand and E.G. Virga, Phys. Rev. E 59, 4137 (1999).

[37] C. Rosenblatt, R. Pindak, N.A. Clark, and R. B. Meyer, Phys. Rev. Lett. 42, 1220 (1979).

[38] P. Sheng, J. Chem. Phys. 59, 1942 (1973).

[39] G. R. Luckhurst and C. Zannoni, Nature (London) 267, 412 (1977).

List of Publications

1. E. Bruno, M.P. De Santo, M. Castriota, G. Strangi, E. Cazzanelli and N. Scaramuzza, Journal of Applied Physics 103, 064103 (**2008**)

2. Ji-Hoom Lee, Timothy J. Atherton, V. Barna, A. De Luca, Emanuela Bruno, Rolfe G. Petschek, and Charles Rosenblatt, Physical Review Letters 102, 167801 (**2009**)

3. E. Bruno, F.Ciuchi, M. Castriota, S. Marino, G. Nicastro, E. Cazzanelli and N. Scaramuzza*",* submitted to Philosophical Magazine (2009)

Morphological and electrical investigations of lead zirconium titanate thin films obtained by sol-gel synthesis on indium tin oxide electrodes

E. Bruno, M. P. De Santo, M. Castriota, S. Marino, G. Strangi, E. Cazzanelli, and N. Scaramuzza[a]

INFM-LICRYL Laboratory—CEMIF.CAL, Department of Physics, University of Calabria, Via P. Bucci, Cubo 33B, 87036 Rende (CS), Italy

(Received 27 July 2007; accepted 10 November 2007; published online 17 March 2008)

In recent years, interest in $PbZr_{0.53}Ti_{0.47}O_3$ (PZT) films has been rapidly increasing due to their technological applications as ferroelectric materials. In the present work, PZT films are obtained by sol-gel synthesis and deposited by spin coating on a transparent conductor substrate, with a perspective application as rectifying layers in asymmetric nematic liquid crystal cells. An extensive investigation is carried out on the effects of different annealing temperatures, with regard to the film texture and to the electric polarization properties, by using low vacuum scanning electron microscopy, atomic force microscopy, and electrostatic force microscopy. It has been observed that PZT domains self-organize into flower-like dendritic structures with a "rosetta" shape at the early stage of crystallization, occurring for annealing temperatures higher than 600 °C; the dimensions of such structures increase versus the annealing temperature. The ferroelectric properties of the PZT films have been related to the observed domains. © *2008 American Institute of Physics*.
[DOI: 10.1063/1.2830987]

I. INTRODUCTION

Thin films of lead zirconium titanate (PZT) are attracting a growing interest because of their applications in nonvolatile memories and piezoelectric transducers.[1,2] The properties of such ferroelectric materials have been investigated in the past ten years, focusing on problems such as elastic and dielectric properties, polarization fatigue, aging, field, and frequency dependence of the piezoelectricity.[3,4]

A particularly interesting application is the use of such films as rectifying layers in asymmetric nematic liquid crystal cells (ANLCC). In such cells, the electro-optical response depends on the polarity of the external electric field, so that it is defined as "rectified electro-optical response," while in the usual cell it is polarity-independent. In fact, metal oxides with mixed ionic and electronic conduction properties have been tested in recent years as rectifying layers in ANLCC, and their rectifying effect has been explained by the formation of double charged layers at the interfaces.[5–9]

In contrast, polarity-dependent responses already observed in ANLCC with an inserted PZT layer have been ascribed to a different mechanism: the polar orientation of the ferroelectric film could generate a permanent internal field opposite (in polarity) to the applied external field.[10] To optimize this particular application of ferroelectric films, specific information must be gathered on the influence of the production methods, the role of the substrate, and the effect of the thermal treatments on the electric and morphological properties of such a layer.

Platinum is the most used substrate for ferroelectric devices because of its good resistance to oxidation. Conducting oxides such as RuO_2,[11] IrO_2,[12] or $SrRuO_3$ (Ref. 13) are also used as electrodes to compensate for the oxygen vacancies and to eliminate the polarization fatigue of ferroelectric capacitors.[14] In this case, to preserve the transparency required by the specific application, the evolution of the deposited PZT films has been investigated on indium-doped tin oxide (ITO) substrate. The final samples can be schematized as: glass/ITO/PZT, where the ITO layer is the electronic conductor.

The samples have been annealed at various temperatures, mainly with the aim to study the differences between the amorphous and the crystalline (perovskite) phases, but also to check differences in electric responses. In fact, previous measurements of displacement current versus the applied voltage reveal a strong asymmetry of the macroscopic polarization properties.[10]

Therefore, in the present work, new investigations are carried out to gain more detailed information on the structural and electric evolution of PZT films obtained by sol-gel synthesis and deposited on ITO-coated glasses. Atomic force microscopy (AFM), electrostatic force microscopy (EFM), and low vacuum scanning electron microscopy (SEM) have been used in order to study at the microscopic level the ferroelectric, piezoelectric, and morphologic properties of PZT films as a function of the different annealing treatments. The EFM technique allows us to simultaneously obtain morphological information with nanometric resolution and to investigate the electrical properties of the PZT layer applying a strongly localized electric field between the probe and the film. Preliminary information about the topographies of such films has been obtained by SEM investigations.

II. EXPERIMENTAL DETAILS

A. Sol-gel preparation

Lead zirconate titanate thin films, with stoichiometric ratios indicated in the formula $PbZr_{0.53}Ti_{0.47}O_3$, were obtained by a hybrid (carboxylate and alkoxides) sol-gel route

[a]Author to whom correspondence should be addressed. Tel.: (+39) 0984-496113; Fax: (+39) 0984-494401; scaramuzza@fis.unical.it.

 © 2008 American Institute of Physics

Downloaded 18 Mar 2008 to 160.97.1.254. Redistribution subject to AIP license or copyright; see http://jap.aip.org/jap/copyright.jsp

and spin-coating deposition of the obtained mother solution on ITO (indium tin oxide) -glass substrate (sheet resistivity $\rho_s = 20\ \Omega/\Box$, Unaxis GmbH) as detailed in a previous paper.[10]

The reagents (all supplied by Sigma-Aldrich) used are lead(II) acetate trihydrate $[Pb(CH_3COO)_2 \cdot 3H_2O$, 99.999%], zirconium(IV) propoxide solution $[Zr(C_3H_7O)_4$, 70 wt. % in 1-propanol], titanium(IV) isopropoxide $(Ti[(CH3)_2CHO]_4$, 99.999%), acetic acid glacial (CH_3COOH, 99.99+%), *n*-propanol anhydrous ($CH_3CH_2CH_2OH$, 99.7%), and ethylene glycol anhydrous ($HOCH_2CH_2OH$, 99.8%).

Briefly, the synthesis of the stock solution was performed in a "humidity-free" glove box in argon atmosphere (percentage of humidity and of molecular oxygen lower than 0.1 ppm). In order to obtain a stable mother solution, the right amount of $Pb(CH_3COO)_2 \cdot 3H_2O$ was dissolved in CH_3COOH by stirring and heating the solution up to 80 °C for 15 min (10.43 g considering the 10% excess in mole of lead, which compensates for the lead loss, as PbO, which occurs during the process). After 2 min at 80 °C the heater was set at 70 °C, and when the solution was cooled down to the latter temperature, the stoichiometric amount of $Zr(C_3H_7O)_4$ solution was added. Later on, $Ti[(CH3)_2CHO]_4$, in its stoichiometric ratio, was added. When the solution was cooled down to room temperature, acetic acid was added and the solution was left to stir for 15 min. At this point, 23.10 g of *n*-propanol and 1.16 g of ethylene glycol were added and again stirred, and after 15 min the solution was sealed and left to stir for one night.

Finally, the solution was removed from the glove box and 9 ml of bidistilled water was added before the spin-coating deposition.

The ITO-coated glasses used as substrates were previously ultrasonically cleaned[6] and a SC10 (CaLCTec s.r.l.) spin coater was used for the deposition of the mother solution. PZT thin films were obtained at 1200 rpm for 25 s. Such samples (glass/ITO/PZT) were placed on a hot plate for 5 min at 300 °C.

Later on, several films were subjected, for an hour, to single thermal treatments in an oven, under room atmosphere, at different temperature values, starting from 100 °C up to 800 °C, each one separated by 100 °C steps.

B. Scanning electron microscopy

Morphologies were obtained using a Quanta FEG 400 (Fei, The Netherlands) scanning electron microscope. This apparatus can work in both environmental conditions as well as in high and low vacuum. It enables investigating samples in a variety of environments manipulating temperature, pressure, and humidity. In particular, this microscope is equipped with a software-controlled heating stage, which can be used for heating the sample up to 1000 °C.

C. Atomic and electrostatic force microscopy

Electrostatic force microscopy (EFM) allows us to obtain information on the surface electrical properties of materials by measuring electric forces between the tip probe and the surface. In this EFM experiment, an electric field is induced inside the PZT thin layer by applying a voltage between a conductive AFM tip (in close proximity to the surface) and the electronic conductor layer (ITO). In the case of thin ferroelectric samples, such an electric field turns out to be very strong, localized, and able to produce domains of electric polarization on a submicrometric scale inside the film. In addition, the evolution of such domains can be studied by EFM investigations.

By applying a dc voltage between the tip and the ITO layer, it becomes possible to orient domains inside the ferroelectric material.[15] In this work, such operation will be indicated as a "writing" process. No contact EFM (NC EFM) mode will be used to probe the surface potential. We will refer to this operation as a "reading" process. To read out the surface potential, an electric voltage, between 0.5 and $1.5V_{rms}$ at a frequency $f=2$ kHz, has been applied between the tip and the ITO layer; such frequency is much lower than the cantilever resonance frequency ($f'=100$ kHz). At the same time, *X*-*Y* scans of the corresponding area using the noncontact regime of AFM have been done.

A laser beam reflected from the cantilever is detected by a photodiode. The lower-frequency signals of the cantilever oscillation, selected by a lock-in amplifier, are used to create the surface potential images, while those at higher frequency are used, simultaneously, to obtain the topographical images. In addition, another mode that can be used for studying piezoelectric materials is direct contact EFM (DC EFM). The reading operation, in DC EFM, is performed in contact mode where the external ac voltage induces the piezoelectric vibration of the PZT layer, and the collected image is representative of the piezoelectric response of the ferroelectric layer against the charge distribution obtained by EFM investigations. AFM (Autoprobe CP, Veeco Instruments, CA) has been modified slightly to work as an EFM, equipped with silicon tips covered with a layer of $PtIr_5$ (Nanosensors, Germany). An external dc power supply (E3630A, Agilent) and a lock-in amplifier (EG&G Instrument, model 7260) have been used for "writing" and "reading" operations, respectively.

III. RESULTS AND DISCUSSION

A. SEM characterization

First of all, SEM has been used to measure the thickness of the PZT films. In Fig. 1, a section of the sample annealed at 100 °C is shown and the three layers glass/ITO/PZT can be clearly observed. The thickness of the PZT layer is about 290 nm, while the ITO thickness is 100 nm, in agreement with the nominal value declared by the manifacturer. Similar estimations have been obtained also for the other samples.

Very interesting results on morphological evolutions and phase-transformation kinetics of the PZT layers are provided by *in situ* investigations. In fact, the experimental procedure of the annealing processes, reproduced inside the SEM instrument, indicates that after annealing at 600 °C, the PZT layer shows on the surface the presence of different flower-shaped dendritic structures, called "rosetta," as shown in Fig. 2. The sizes of such structures range from hundreds to thou-

Downloaded 18 Mar 2008 to 160.97.1.254. Redistribution subject to AIP license or copyright; see http://jap.aip.org/jap/copyright.jsp

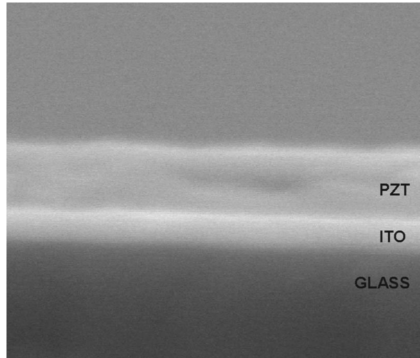

FIG. 1. Transversal section view of the thin PZT film deposited on ITO/glass.

sands of nanometers, increasing for higher-temperature treatments.

Calorimetric measurements performed on such samples have shown an exothermic peak at temperatures slightly higher than 600 °C,[10] which has been assigned to the phase transition from amorphous to crystalline phases.[10,16]

B. EFM characterization

In Fig. 3 (on the left) is shown the topography, given by AFM, of a region where a line was "written" by a constant voltage, for a sample annealed at 100 °C for 1 h. In the middle is shown the corresponding EFM image, related to a line previously "written" applying 10 V. Finally, on the right, the EFM image is shown of the line previously "written" applying −10 V.

FIG. 2. SEM images showing various steps of the *in situ* phase transition of a PZT film.

Downloaded 18 Mar 2008 to 160.97.1.254. Redistribution subject to AIP license or copyright; see http://jap.aip.org/jap/copyright.jsp

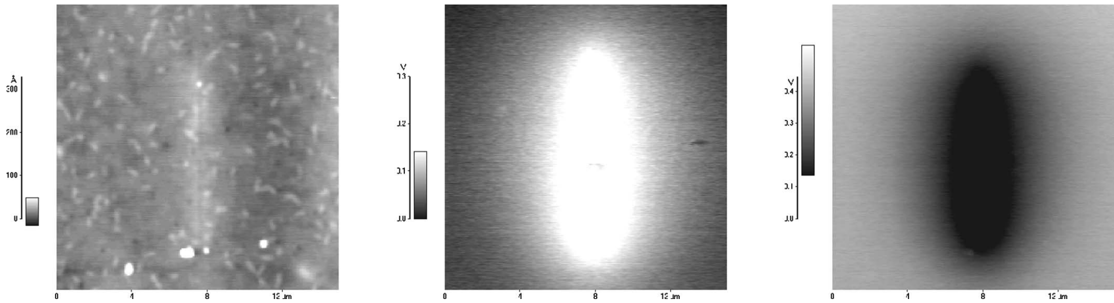

FIG. 3. Sample annealed at 100 °C, topography (left), line written applying 10 V (middle) and line written applying −10 V (right).

During the application of the voltage in contact mode, an additional pressure, due to the electrostatic forces between the tip and the sample's surface, is applied on the sample. It can induce a small amount of damage on the surface, as is evident from the topographical images of Fig. 3.

Black and white spots on the electric maps are related to the charge distributions on the surface, due to the applied dc voltage, in a corona-like discharge effect. Following the time evolution of the electrical traces, it can be observed that the spot dimensions of accumulated charges decrease in time, due to the ohmic diffusion of charges on the surface. After 15 min, the white spot vanishes completely while the black one is still detectable, revealing an asymmetrical behavior of the electric charge persistence on the surface, while no relevant changes are observed on the topography.

Results quite similar to those of the 100 °C annealed samples have been obtained for samples treated at 200, 300, 400, and 500 °C. A different behavior has been observed, on the contrary, for the samples annealed at 600, 700, and 800 °C, which underwent the phase transition to a crystalline structure, as stated above.

In Fig. 4 images are shown related to the AFM topographies of samples annealed at 600 °C (on the left), 700 °C (in the middle), and 800 °C (on the right). As previously shown by SEM characterizations, an abrupt change of topography occurs when the samples are heated above 600 °C, changing from a granular structure to the nucleation of the "rosetta" structures, with higher dimensions for higher annealing temperatures. These structures can be reasonably related to well-crystallized domains, whose expansion is favored by the high temperatures.

In Fig. 5 EFM images are shown related to the electric traces collected on samples annealed at 600 °C (on the top) and 700 °C (on the bottom). For each annealing temperature, the left images show lines "written" by a positive voltage (10 V), while on the right are shown the electrical traces "written" by the opposite voltage (−10 V). The black spots of the samples annealed at 600 °C are better defined than those observed on the samples annealed at lower temperatures. Moreover, they are still detectable after 2 h. This could be related to the alignment of the dipoles inside the PZT layer that traps the charges deposited on the surface by the corona effect. On the other hand, the lifetime of the white line is still shorter than that of the black one and disappears after 30 min.

On the sample annealed at 700 °C, a rearrangement of the granular structure in clusters of micrometric size can be observed (see Fig. 5, bottom). The EFM image (bottom right) shows as the definition of the electric trace "written" applying −10 V is still improved and much more intense. It has been supposed that in these samples, the transition from the paraelectric to the ferroelectric phases occurred. Such evolution is even more evident in the EFM image related to the samples annealed at 800 °C, as shown in Fig. 6.

From the topographical images shown in Fig. 4, an increase in the size of the clusters can be seen for the samples annealed at 800 °C. In the EFM images (Fig. 6), two very thin lines are visible, "written" by the two opposite voltages. This increased sharpness could be explained taking into account a stronger dipole reorientation inside the ferroelectric layer. Such lines are still detectable after more than 5 h.

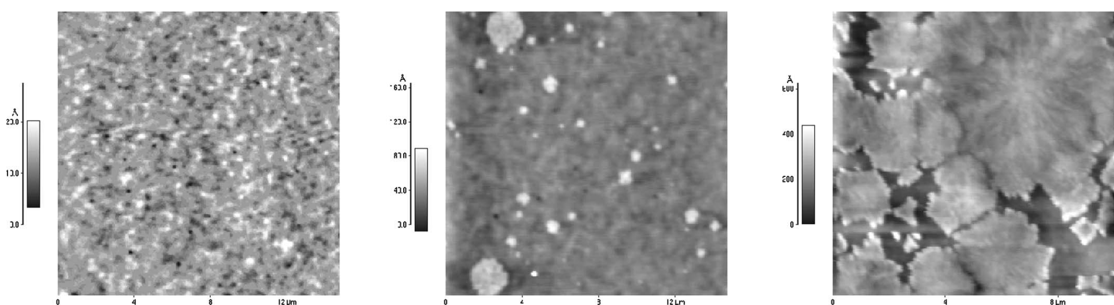

FIG. 4. Topography of samples annealed at 600 °C (left), 700 °C (middle), and 800 °C (right)

Downloaded 18 Mar 2008 to 160.97.1.254. Redistribution subject to AIP license or copyright; see http://jap.aip.org/jap/copyright.jsp

FIG. 5. EFM images: sample annealed at 600 °C (top), line written applying 10 V (top, left) and line written applying −10 V (top, right); sample annealed at 700 °C (bottom), line written applying 10 V (bottom, left) and line written applying −10 V (bottom, right).

On the samples annealed at the highest temperature, contact EFM has been performed to check the piezoelectric response of the PZT layer. When using contact mode, the "writing" operation requires higher dc voltages: in order to obtain detectable lines, ±20 V were applied. The EFM images show high intensities (Fig. 7) and they have been related to the piezoelectric effect of the PZT layer. Even in contact mode, the higher intensity of the electric signal is confirmed related to the black line with respect to that of the white line, as can be seen in Fig. 7.

IV. CONCLUSIONS

The use of different experimental techniques allowed us to obtain important information about the structure and the electric characterization of PZT thin films deposited on ITO substrates. The EFM technique was used to investigate the

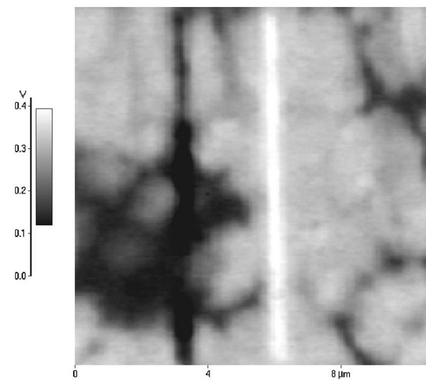

FIG. 6. No contact EFM image of the PZT sample annealed at 800 °C, lines written at ±10 V (white: +10 V, black: −10 V).

Downloaded 18 Mar 2008 to 160.97.1.254. Redistribution subject to AIP license or copyright; see http://jap.aip.org/jap/copyright.jsp

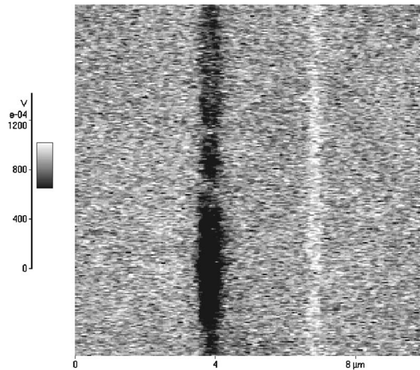

FIG. 7. Direct contact EFM image of the PZT sample annealed at 800 °C, lines written at ±20 V (white: +20 V, black: −20 V).

ferroelectric properties of the PZT layers, and the effect of the induced polarization was monitored as a function of the time.

Moreover, from the EFM images it was possible to distinguish, at least qualitatively, two different behaviors of the charge distributions, depending on annealing temperatures, lower or higher than 600 °C. In the samples annealed below 600 °C, the charge distribution appears quite diffuse and tends to disappear in less than 1 h. On the contrary, for the samples annealed above 600 °C, the charge deposited during the "writing" operations appears quite confined and remains for a time longer than 2 h. This evidence can be reasonably explained as a simple charge deposition on a dielectric surface in the first cases (lower the 600 °C), and assigned to the ferroelectric behavior of the PZT layers in the other case. However, a more precise modelization of these phenomena requires collecting more data to better quantify the time evolution of the electric response after writing processes.

Taking into account the presently available data, several hypotheses can be considered to explain the asymmetric behavior of the permanency times of the charge distributions.

A possible interpretation associates the asymmetric behaviors shown above to the presence of oxygen vacancies. In fact, such oxygen vacancies behave differently depending on the PZT composition, i.e., they migrate toward the PZT/air interface for low ratio Zr/(Zr+Ti) (<0.25) or toward the ITO/PZT interface for high ratio Zr/(Zr+Ti) (>0.25). Such positive charge displacements give rise to internal fields that could be responsible for the favorite orientations of the ferroelectric dipoles.[17,18]

Other hypotheses point to the effects related to the ITO/PZT interface. The same asymmetric switching has been reported by Gruverman *et al.*[19] They attributed it to the presence of an internal built-in electric field at the interface and to the mechanical stress exerted by the AFM tip. Asymmetric switching was also observed on ferroelectric polymeric thin films of PVDF-TrFE.[20] In this case, it was attributed to a partial poling in the film induced by the substrate.

Further studies about the influence of the conductive substrate, the zirconium titanium ratio, and the annealing treatments on the ferroelectric properties of PZT thin layers are currently in progress, as well as precise structural characterization of the various phases by XRD analysis.

ACKNOWLEDGMENTS

The authors wish to thank Dr. Giuseppe De Santo and Dr. Tiziana Barone for their essential contribution during the PZT thin layers preparation, Dr. Giovanni Desiderio for the SEM imaging, and Dr. Alfredo Pane for technical support.

[1]C. T. Lin, B. W. Scanlan, J. D. Mcneill, J. S. Webb, and L. Li, J. Mater. Res. **7**, 2546 (1992).
[2]S. S. Dana, K. F. Etzold, and S. Clabes, J. Appl. Phys. **69**, 4398 (1991).
[3]*Science and Technology of Electroceramic Thin Films (NATO/ARW Series E)*, edited by O. Auciello and R. Waser (Kluwer, Deventer, 1994), Vol. 284.
[4]D. Damjanovic, "Ferroelectric, dielectric and piezoelectric properties of ferroelectric thin films and ceramics," Ph.D. thesis, Swiss Federal Institute of Technology-EPFL, Lausanne, Switzerland (1998).
[5]S. Marino, M. Castriota, V. Bruno, E. Cazzanelli, G. Strangi, C. Versace, and N. Scaramuzza, J. Appl. Phys. **97**, 013523 (2005).
[6]M. Castriota, S. Marino, C. Versace, G. Strangi, N. Scaramuzza, and E. Cazzanelli, Mol. Cryst. Liq. Cryst. **429**, 237 (2005).
[7]G. Strangi, E. Cazzanelli, N. Scaramuzza, C. Versace, and R. Bartolino, Phys. Rev. E **62**, 2263 (2000).
[8]E. Cazzanelli, S. Marino, V. Bruno, M. Castriota, N. Scaramuzza, G. Strangi, C. Versace, R. Ceccato, and G. Carturan, Solid State Ionics **165**, 201 (2003).
[9]V. Bruno, M. Castriota, S. Marino, C. Versace, G. Strangi, E. Cazzanelli, and N. Scaramuzza, Mol. Cryst. Liq. Cryst. **441**, 27 (2005).
[10]S. Marino, M. Castriota, G. Strangi, E. Cazzanelli, and N. Scaramuzza, J. Appl. Phys. **102**, 013112 (2007).
[11]G. Asano, H. Morioka, and H. Funakubo, Appl. Phys. Lett. **83**, 5506 (2003).
[12]B. S. Kang, D. S. Kim, J. Y. Jo, T. W. Noh, J. G. Yoon, T. K. Song, Y. K. Lee, J. K. Lee, S. Shin, and Y. S. Park, Appl. Phys. Lett. **84**, 3127 (2004).
[13]S. Aggarwal, I. G. Jenkins, B. Nagarag, C. J. Kerr, C. Canedy, R. Ramesh, G. Velasquez, L. Boyer, and J. T. Evans, Jr., Appl. Phys. Lett. **75**, 1787 (1999).
[14]Z. Jia, T. L. Ren, T. Z. Liu, H. Hu, Z. G. Zhang, D. Xie, and L. T. Liu, Chin. Phys. Lett. **23**, 1042 (2006).
[15]L. M. Blinov, R. Barberi, S. P. Palto, M. P. De Santo, and S. G. Yudin, J. Appl. Phys. **89**, 3960 (2001).
[16]S. Dunn and R. W. Whatmore, J. Eur. Ceram. Soc. **22**, 825 (2002).
[17]A. Wu, P. M. Vilarinho, V. V. Shvartsman, G. Suchaneck, and A. L. Kholkin, Nanotechnology **16**, 2587 (2005).
[18]T. I. Chang, J. L. Huang, H. P. Lin, S. C. Wang, H. H. Lu, L. Wu, and J. F. Lin, J. Alloys Compd. **414**, 224 (2006).
[19]A. Gruverman, A. Kholkin, A. Kingon, and H. Tokumoto, Appl. Phys. Lett. **78**, 2751 (2001).
[20]X. Q. Chen, H. Yamada, Y. Terai, T. Horiuchi, K. Matsushige, and P. S. Weiss, Thin Solid Films **353**, 259 (1999).

Downloaded 18 Mar 2008 to 160.97.1.254. Redistribution subject to AIP license or copyright; see http://jap.aip.org/jap/copyright.jsp

Direct Measurement of Surface-Induced Orientational Order Parameter Profile above the Nematic-Isotropic Phase Transition Temperature

Ji-Hoon Lee,[1] Timothy J. Atherton,[1] Valentin Barna,[2] Antonio De Luca,[3] Emanuela Bruno,[3] Rolfe G. Petschek,[1] and Charles Rosenblatt[1]

[1]*Department of Physics, Case Western Reserve University, Cleveland, Ohio, 44106-7079, USA*
[2]*Faculty of Physics, University of Bucharest, P.O. Box Mg-11, 077125, Bucharest, Magurele, Romania*
[3]*CNR-INFM LiCryL, Centro di Eccellenza dell'Universita della Calabria, c/o Physics Department, University of Calabria, 87036 Rende (CS), Italy*

(Received 14 November 2008; published 24 April 2009)

The spatial and temperature dependence of the surface-induced orientational order parameter $S(z, T)$ was determined in the isotropic phase. An optical fiber was immersed in a thin liquid crystal layer and the retardation was measured as a function of the fiber's height above the surface, from which the model-independent $S(z, T)$ was deduced with resolution $\lesssim 2$ nm. It was found that (i) $S(z = 0) \lesssim 0.12$ close to the nematic transition temperature, (ii) the susceptibility is mean-field-like, and (iii) $S(z, T)$ deviates significantly from exponential spatial decay. The results are discussed in terms of a nonlocal potential.

DOI: 10.1103/PhysRevLett.102.167801 PACS numbers: 61.30.Hn

Surface-induced orientational order at the nematic-isotropic (NI) phase transition has received extensive scrutiny [1–22]. Above the bulk first order NI temperature T_{NI}, an appropriately prepared surface induces orientational order in the otherwise isotropic phase, with the order decreasing into the bulk. The behavior of the scalar orientational order parameter $S(z)$ ($\equiv \langle \frac{3}{2}\cos^2\theta - \frac{1}{2}\rangle$, where θ is the angle from the nematic director $\hat{n}$) depends on the interaction energy between the liquid crystal (LC) and the alignment layer(s), the physical properties and thickness of the LC layer, and the temperature T. It generally is assumed that the surface potential is localized to the interface at $z = 0$ [3,5,10,11], with the uniaxial order parameter at the interface S_0 [$\equiv S(z = 0)$] determined by the form of the potential [3,5,9,11]. If the surface-induced order is not sufficiently large, only partial wetting by the nematic phase occurs. On the other hand, if the interaction between the LC and the surface is strong, $S(z)$ integrated through the cell thickness diverges logarithmically on approaching T_{NI} [1–3,12]; this corresponds to complete wetting by the nematic phase. Moreover, "capillary condensation"—a transition to the nematic phase in a localized boundary layer—has been predicted [4,11] and observed experimentally [13,17–19]. Sheng also predicted [5] a "prewetting transition" in which there is a discontinuous jump of S_0 at a temperature $T > T_{NI}$, which also has been observed experimentally [22].

To date quantitative determinations of the order parameter profile $S(z)$ versus temperature have used probes with visible light wavelength resolution—this is much larger than the length scale of the surface layer—and so required specific models in conjunction with the macroscopic data in order to extract $S(z)$ [1,2]. Other techniques that measure local quantities, such as evanescent wave and second harmonic generation experiments [6–9], also require specific models to extract $S(z)$. Recently, however, we have shown that the light intensity emerging from a tapered optical fiber immersed in a LC film and passing through an analyzer is well approximated by the total optical retardation α from the fiber aperture through the birefringent medium to the surface [23,24]. This allows us to obtain orientational order information in three dimensions out to $z \sim 500$ nm above the interface, with lateral resolution $\sim$125 nm and vertical resolution $\sim$2 nm. Here we apply this technique to surface-induced nematic order, whereby we measure α between the fiber aperture and the substrate as a function of the aperture's height h above the substrate and temperature $T > T_{NI}$. This allows us to extract the model-independent profile $S(z)$ vs T close to the substrate. In particular, we find that $S_0 \lesssim 0.12$ and that S_0^{-1} vs T is mean-field-like, scaling approximately as $T - T^*$, where T^* is the supercooling limit of the isotropic phase, indicating the absence of capillary condensation in our system for the temperatures studied. Moreover, we found that $d\alpha/dh$ varies slowly with h out to $h \approx 10$ nm, substantially different from the quasiexponential decay expected for weak surface-induced order in the absence of capillary condensation [3,5].

A glass substrate was spin coated with the polyamic acid RN-1175 (Nissan Chemical Industries, Ltd.), prebaked according to manufacturer's specifications at 100 °C for 3 min, then fully baked at 230 °C for 60 min to achieve imidization. To establish the azimuthal orientation of the planar alignment, the polyimide-coated slide was rubbed with a rubbing strength $n_f = 1.5 \times 10^6$ cm^{-1} using a cotton cloth and rubbing machine [25]. Atomic force microscope measurements of the resulting surface revealed a short wavelength roughness with characteristic length scale $\sim$30–40 nm and rms amplitude $A_r \sim 1.5$ nm, as well as longer wavelength ($L \sim 1$ μm) grooves with a rms ampli-

 © 2009 The American Physical Society

tude $A_g < 1$ nm due to the rubbing cloth's crenellations [26]. The slide then was coated with a thin film (a few μm) of the LC pentylcyanobiphenyl ("5CB", Merck) and placed into a Veeco Aurora near-field scanning optical microscope. (See Fig. 1 in Ref. [24]). The approximately conical-shaped fiber (cone angle 10°) was illuminated by circularly polarized light (extinction ratio ~1.2:1) at wavelength $\lambda = 532$ nm that first passed through a light chopper. The light emerged from the fiber's flat aperture (aperture width ~65 nm; total diameter $d_f < 200$ nm, including Al cladding), which was immersed into a thin layer (a few μm) of LC. The approximately circularly polarized transmitted light passed through the LC, the alignment layer, the glass slide, an analyzer rotated by 45° with respect to the rubbing direction, and was collected by a photomultiplier tube. The photomultiplier tube output was input to a lock-in amplifier referenced to the light chopper; a 10 s time constant filter was used to average out the noise. The entire assembly was housed in a box, with a string of resistors placed along the box's inner walls and connected to a temperature controller; good thermal stability (<10 mK) and homogeneity ($\nabla T < 5$ mK cm^{-1}) were maintained.

The sample was stabilized ~1.8 °C above $T_{\rm NI}$ and the fiber was lowered to make contact with the substrate, corresponding to $z = 0$. In light of the long time constant filter, the intensity was recorded after a delay of approximately 50 s. The fiber then was elevated a few nanometers, the signal was allowed to stabilize for another 50 s, and the intensity was again recorded. This procedure was repeated about 20 times in order to construct an intensity I vs height h profile at this temperature. The temperature then was reduced by a few tens of millikelvins and, after allowing 2 h for the temperature to stabilize, the measurement procedure was repeated to obtain I vs h at this temperature. Data were collected at multiple temperatures down to $T_{\rm NI} + 50$ mK, where $T_{\rm NI}$ was found to drift by <10 mK over the duration of the entire experiment. Figure 1(a) shows I vs h for all temperatures relative to $T_{\rm NI}$, where the position of each baseline varied from run to run. It is apparent that I varies linearly with h out to ~10 nm, beyond which dI/dh decreases until I becomes constant for $h \gtrsim 30$ nm.

To relate $I(h, T)$ to a physical quantity, we note that at fixed T, I is approximately $\propto \alpha$, although the proportionality constant $C(T)$ was found empirically to depend on T due to the thermal characteristics—including those due to ∇T—of the fiber. To obtain $C(T)$, we placed a top slide treated for homeotropic alignment on the sample, using a spacer of nominal thickness 10 μm. The now enclosed cell was then placed into a temperature controller and Pockels cell-based birefringence apparatus [27]. The beam from a He-Ne laser at wavelength $\lambda_0 = 633$ nm was focused to a spot of ~100 μm at the sample, and the total retardation $\alpha_{\rm tot}(T)$ through the cell was measured versus T. Because

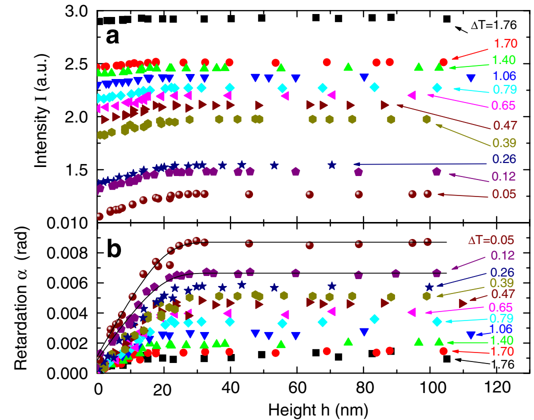

FIG. 1 (color online). (a) Intensity versus aperture's height h above substrate at temperatures $\Delta T = (T - T_{\rm NI})$. The different baselines for each ΔT are due to slow drifts compared to the data acquisition time and to a systematic variation of the baseline with temperature due to the thermal characteristics of the fiber. (b) Retardation α versus height h extracted from intensity data in (a) and normalized to the total retardation $\alpha_{\rm tot}(T)$ through entire cell. Each set of data was regularized (see text), and two examples are shown by the solid lines.

$\alpha_{\rm tot}(T) = C(T)\Delta I(T)$, where $\Delta I(T)$ is the intensity difference between the baseline (at $h = 0$) and saturation intensities, $C(T)$ was extracted and the intensity data in Fig. 1(a) were converted to retardation α vs h at each temperature [Fig. 1(b)] for wavelength λ_0.

Let us now turn to the meaning of α vs h. We note that $\alpha(h) = \int_0^h k_0 \Delta n(z) dz$, where $k_0 = 2\pi/\lambda_0$ and $\Delta n(z)$ is the LC birefringence at $\lambda_0 = 633$ nm at height z. Because $\Delta n = DS$ for small S, where the proportionality constant $D = 0.28$ for 5CB [28,29], $\alpha(h) = k_0 D \int_0^h S(z) dz$. That $\alpha \propto h$ for $h \lesssim 10$ nm suggests one of two scenarios: Either (i) $S(z)$ varies weakly over this range or (ii) $S(z)$ varies significantly with position h of the fiber aperture but its integral always happens to be proportional to h over this range. We discount mechanism (ii) because it would require the coincidence of far too many conditions, such as anchoring potentials at the substrate and fiber having the correct forms. Thus we believe that $S(z)$ decays slowly near the substrate (over a length $\gg A_r$), which will be discussed in more detail below. Hence $S_0 = (d\alpha/dh)_{h=0}/k_0 D$. In order to differentiate numerically the data in Fig. 1(b) and avoid the noise associated with numerical differentiation, we fitted a piecewise smooth Bezier curve of third degree to five representative data points, matching the values and derivatives for each section. Typical examples are shown by the solid curves in Fig. 1(b). $S(z, T)$ then was obtained from the derivative of the Bezier curve; results are shown in Fig. 2. From Fig. 2 we extract S_0 and plot S_0^{-1} vs T in Fig. 2, inset. There are three important features. First,

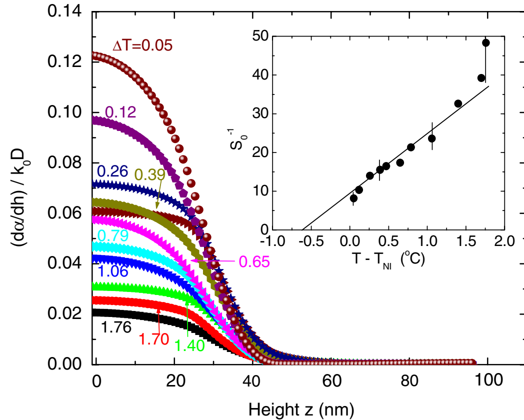

FIG. 2 (color online). The quantity $(d\alpha/dh)/k_0D$ (which is $\approx S$) versus height h. Inset: S_0^{-1} vs $T - T_{NI}$.

S_0 is relatively small for all T, having a maximum value of $S_0 \approx 0.12$ at $T - T_{NI} = 0.05\,°\mathrm{C}$. These are much smaller than values predicted [4,5] and measured experimentally [13,17] when capillary condensation occurs. The data also indicate that no prewetting transition [5] was observed, at least for $T > T_{NI} + 0.05\,°\mathrm{C}$. Second, the behavior of S_0^{-1} vs T in Fig. 2, inset, is reminiscent of the mean-field behavior for the orientational susceptibility in the isotropic phase, associated with a susceptibility exponent $\gamma = 1$ and a value to $T_{NI} - T^* \sim 1\,°\mathrm{C}$. The observed downward deviation of S_0^{-1} close to T_{NI} also is commonly observed [30] in bulk measurements, although in our case this may be due to experimental scatter. In contrast, Sheng's model [5] for capillary condensation for walls spaced <5 nm apart predicts a highly nonlinear variation of S_0^{-1} with temperature and $T_{NI} - T^* > 4\,°\mathrm{C}$, which is contrary to our results. Third, $d\alpha/dh \sim 0$ for $h > 30$ nm, indicating that $S \sim 0$ beyond this range. This length scale differs sharply from that of capillary condensation, where $S \neq 0$ is observed experimentally for substrates separated by hundreds of nanometers [13]. Overall, our results suggest that there are no observable confinement effects because of the weak LC order at the rubbed polyimide and because the interaction potential between fiber and LC is very small. This negligible interaction with the fiber's surface is consistent with previous work over a wide range of length scales by our group and others [23,24,31]. Nevertheless, even in the absence of any preferred surface alignment or ordering, there exists a torquelike natural boundary condition $dS/dz|_{z=h} = 0$ at the fiber. On applying Sheng's model [5] to calculate $S(z, T)$ when $S_0 \lesssim 0.12$ with this boundary condition, we obtain profiles for $S(z, T)$—we equate this with $(d\alpha/dh)_{h=z}/k_0D$—that differ by less than 10% from profiles in the absence of a fiber, i.e., with $dS/dz|_{z\to\infty} = 0$. Thus taking account of all of our observations, *a posteriori* we can treat $(d\alpha/dh)_{h=z}/k_0D$ as approximately $S(z)$, facilitating its measurement without requiring a specific model.

Beyond the surface, perhaps our most important observation is that $S(z)$ falls off slowly over several nanometers before decaying more rapidly. This behavior is *not* consistent with the exponential decay [characterized by a nematic correlation length $\xi(T)$] that is expected when S_0 is small [3,5]; a possible mechanism for the decay profile will be discussed below. Nevertheless, the increase in the aperture height h_s with decreasing T at which α seems to saturate [Fig. 1(b)] presumably is due to an increase of $\xi(T)$ on approaching the transition. To make this more apparent, Fig. 3 shows the quantity α/S_0 at three representative temperatures. As expected, the initial slopes are the same, but at higher temperatures α/S_0 "saturates" at a height h_s lower than it does at temperatures closer to T_{NI}.

The initial slow spatial decay of $S(z)$ raises questions about the physics near the interface. Hsiung *et al.* assumed an exponential form for $S(z)$ to analyze their evanescent wave ellipsometry data, obtaining an excellent fit and information about ξ vs T [7]. In their case this form likely was justified, as their *homeotropic* alignment was controlled by silane molecules at the surface that provided a well localized potential. In our experiment, however, we obtain *planar* alignment by mechanically rubbing a polyimide. The rubbing process has two effects: It creates long wavelength grooves [26] and it realigns the polymer backbone, which can extend to some depth into the polyimide layer. Because $L \gg d_f$ and A_g is small, the grooves have little influence on S_0, except in the region $z \lesssim A_g$. On the other hand, the realignment of the backbone can extend many nanometers into the polymer film [8,32,33]. Given this situation, Barbero and Evangelista showed [34] how quadrupole-quadrupole interactions can act over a range of several nanometers; an inhomogeneous spatial distribution of adsorbed charges at the interface [35] also would give rise to nonlocal forces. Nonlocal interactions have been shown to affect physical quantities such as surface viscosity [36] and elasticity in freestanding smectic-C films [37], where the length scale of the interactions extends $\xi \sim$ 5–10 nm and results in a reduced elastic constant for films

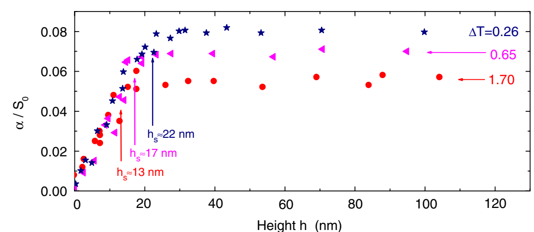

FIG. 3 (color online). The quantity α/S_0 versus height at three representative temperatures. Vertical arrows show the height h_s (±3 nm) at which α saturates.

thinner than ξ [37]. The data near $z = 0$ in Fig. 2 clearly show deviations over these length scales from Landau–de Gennes behavior with a highly localized potential. We therefore speculate that the nonlocality of the "surface" potential may be playing the central role. To be sure, such a scenario does not necessarily apply to all interfaces; as noted above, orientation from a surface agent (e.g., silane) is likely to be highly localized. Nevertheless, for planar alignment that relies on anisotropic attractive interactions, especially those in which the anisotropy extends some distance beneath the surface and into the "bulk" polymer alignment film, the extended range of interactions may result in an $S(z)$ profile within several nanometers of the interface that is very different from exponential decay.

To summarize, we have demonstrated that a variation on optical nanotomography [23,24] facilitates a model-free approximate determination of the surface-induced orientational profile. Moreover, the behavior of S vs z is very different from that expected from the oft assumed Landau–de Gennes model with a localized surface potential, suggesting that a nonlocal potential and/or other mechanisms (e.g., short range molecular clustering [38,39]) are needed to describe this behavior.

The authors are grateful to T. J. Sluckin, G. Carbone, P. Sheng, and C. Zannoni for useful discussions, and we thank Nissan Chemical Industries, Ltd. for providing the RN-1175. J-H. L. was supported by the Korean Research Foundation under Grant No. KRF-2007-357-C00034; C. R., A. D. L., and T. A. by U.S. DOE Office of Basic Energy Science under Grant No. DE-FG02-01ER45934; R. G. P. by the Office of Naval Research under Grant No. N00014-05-0404; and C. R. and V. B. by the National Science Foundation under Grant No. DMR-0804111.

[1] K. Miyano, Phys. Rev. Lett. **43**, 51 (1979); J. Chem. Phys. **71**, 4108 (1979).
[2] J. C. Tarczon and K. Miyano, J. Chem. Phys. **73**, 1994 (1980).
[3] D. W. Allender, G. L. Henderson, and D. L. Johnson, Phys. Rev. A **24**, 1086 (1981).
[4] P. Sheng, Phys. Rev. Lett. **37**, 1059 (1976).
[5] P. Sheng, Phys. Rev. A **26**, 1610 (1982).
[6] W. Chen, L. J. Martinez-Miranda, H. Hsiung, and Y. R. Shen, Phys. Rev. Lett. **62**, 1860 (1989).
[7] H. Hsiung, Th. Rasing, and Y. R. Shen, Phys. Rev. Lett. **57**, 3065 (1986).
[8] M. B. Feller, W. Chen, and Y. R. Shen, Phys. Rev. A **43**, 6778 (1991).
[9] T. Moses and Y. R. Shen, Phys. Rev. Lett. **67**, 2033 (1991).
[10] T. J. Sluckin and A. Poniewierski, *Fluid and Interfacial Phenomena*, edited by C. A. Croxton (John Wiley & Sons, New York, 1986).
[11] T. J. Sluckin and A. Ponewierski, Liq. Cryst. **2**, 281 (1987).
[12] B. Jérôme, Rep. Prog. Phys. **54**, 391 (1991).
[13] H. Yokoyama, S. Kobayashi, and H. Kamei, Mol. Cryst. Liq. Cryst. **99**, 39 (1983); J. Appl. Phys. **61**, 4501 (1987).
[14] G. Barbero and G. Durand, J. Phys. II (France) **1**, 651 (1991).
[15] R. Barberi and G. Durand, Phys. Rev. A **41**, 2207 (1990).
[16] S.-T. Wu and U. Efron, Appl. Phys. Lett. **48**, 624 (1986).
[17] A. Borstnik Bracic, K. Kocevar, I. Musevic, and S. Zumer, Phys. Rev. E **68**, 011708 (2003).
[18] K. Kocevar, A. Borstnik, I. Musevic, and S. Zumer, Phys. Rev. Lett. **86**, 5914 (2001).
[19] K. Kocevar and I. Musevic, Phys. Rev. E **64**, 051711 (2001).
[20] B. Wen, J.-H. Kim, H. Yokoyama, and C. Rosenblatt, Phys. Rev. E **66**, 041502 (2002).
[21] J.-H. Kim and C. Rosenblatt, J. Appl. Phys. **84**, 6027 (1998).
[22] X. Liu, D. W. Allender, and D. Finotello, Europhys. Lett. **59**, 848 (2002).
[23] V. Barna, A. De Luca, and C. Rosenblatt, Nanotechnology **19**, 325709 (2008).
[24] A. De Luca, V. Barna, T. Atherton, G. Carbone, M. Sousa, and C. Rosenblatt, Nature Phys. **4**, 869 (2008).
[25] J.-H. Lee, T. J. Atherton, D. Kang, R. G. Petschek, and C. Rosenblatt, Phys. Rev. E **78**, 021708 (2008).
[26] M. P. Mahajan and C. Rosenblatt, J. Appl. Phys. **83**, 7649 (1998).
[27] C. Rosenblatt, F. F. Torres De Araujo, and R. B. Frenkel, Biophys. J. **40**, 83 (1982).
[28] P. P. Karat and N. V. Madhusudana, Mol. Cryst. Liq. Cryst. **36**, 51 (1976).
[29] N. V. Madhusudana and R. Pratibha, Mol. Cryst. Liq. Cryst. **89**, 249 (1982).
[30] T. W. Stinson, J. D. Litster, and N. A. Clark, J. Phys. (Paris) **33**, C1-69 (1972).
[31] T. Tadokoro, T. Saiki, and H. Toriumi, Jpn. J. Appl. Phys. **41**, L152 (2002); Jpn. J. Appl. Phys. **42**, L57 (2003).
[32] J.-H. Kim and C. Rosenblatt, J. Appl. Phys. **87**, 155 (2000).
[33] S. Kuniyasu, H. Fukuro, S. Maeda, K. Nakaya, M. Nitta, N. Ozaki, and S. Kobyashi, Jpn. J. Appl. Phys. **27**, 827 (1988).
[34] G. Barbero and L. R. Evangelista, *Adsorption Phenomena and Anchoring Energy in Nematic Liquid Crystals* (Wiley, New York, 2005).
[35] G. Barbero and G. Durand, J. Appl. Phys. **67**, 2678 (1990).
[36] G. E. Durand and E. G. Virga, Phys. Rev. E **59**, 4137 (1999).
[37] C. Rosenblatt, R. Pindak, N. A. Clark, and R. B. Meyer, Phys. Rev. Lett. **42**, 1220 (1979).
[38] P. Sheng, J. Chem. Phys. **59**, 1942 (1973).
[39] G. R. Luckhurst and C. Zannoni, Nature (London) **267**, 412 (1977).